Boundary Conditions in Laboratory and Field Compaction

Elisa Martinez Avilés

A Thesis

in

The Department

of

Building, Civil and Environmental Engineering

Presented in Partial Fulfillment of the Requirements

for the Degree of Master Applied Science (Civil Engineering) at

Concordia University

Montreal, Quebec, Canada

August 2008

Your file Votre référence
ISBN: 978-0-494-45340-7
Our file Notre référence
ISBN: 978-0-494-45340-7

ABSTRACT

Boundary Conditions in Laboratory and Field Compaction

Elisa Martinez Avilés

Dynamic compaction of soils is an efficient and cost effective ground improvement technique, allowing for the use of sites previously considered unsuitable for construction. The technique consists of densifying loose granular materials by applying high energy impacts to a soil's surface by dropping a heavy weight carried by a crane at a given height.

Field compaction predictions based upon laboratory Proctor test results generally result in great discrepancies with the obtained field results. A Proctor test sample is restrained both laterally and at its bottom, whereas a field sample is free to move in three dimensions. Therefore, the boundary conditions of the Proctor test are incompatible with those of field compaction.

This thesis presents a numerical model capable of examining both the field and laboratory boundary conditions of a soil sample undergoing dynamic compaction. It was found that the boundary conditions of the Proctor test are incompatible with those of dynamic field compaction and that the stiffness of the underlying layer plays a role in determining the level of compaction experienced by the overlying layer. This relationship was further explored by accounting for varying thicknesses of the upper layer with a range of stiffness values for the underlying layer. A trend of decreasing compaction with increasing upper layer thickness was observed when the underlying layer's modulus of elasticity exceeded that of the upper layer. Also, compaction of the upper layer increased

as the elasticity modulus of the lower layer increased for upper layer thicknesses of 1 and 2 m.

ACKNOWLEDGEMENTS

I would like to express my sincere gratitude to my supervisor, Dr. Adel Hanna, for being my mentor over the past few years. His encouragement and support have been invaluable to me throughout the course of both my undergraduate and graduate studies. On this occasion I would also like to thank the staff of the BCEE department who have helped me along the way over the past few years.

Finally, I wish to thank my friends and family, near or far, for all their unwavering moral support, as I am well aware that I would not be here without them.

Elisa Martinez Avilés

LIST OF FIGURES

LIST OF TABLES

LIST OF SYMBOLS

Symbols

dmax	=	Depth of improvement
n	=	Empirical coefficient for energy per drop
W	=	Weight of tamper
H	=	Drop height
fn	=	Natural frequency of a system
T	=	Period of vibration
K	=	Vertical stiffness of the system
G	=	Shear modulus
ro	=	Radius of the mass or tamper
υ	=	Poisson's ratio
m	=	Mass of the weight or tamper
g	=	Gravitational constant
ω1	=	Amplitude of vibration at distance r1 from the source
ω2	=	Amplitude of vibration at distance r2 from the source
n	=	Attenuation due to radiation damping
a	=	Attenuation coefficient due to material damping
VR	=	Propagation velocity of R-waves
D	=	Geomaterial damping ratio
F	=	Frequency of vibration

VSO	=	Shear wave velocity of soil
γ	=	Cyclic shear amplitude
$\overline{\sigma_0}$	=	Mean effective confining pressure
Gmax	=	Maximum dynamic shear modulus
[C]	=	Rayleigh damping matrix of the system
[M]	=	Mass matrix of the system
[K]	=	Stiffness matrix of the system
α	=	Rayleigh damping parameter for mass
β	=	Rayleigh damping parameter for stiffness
I	=	Applied energy intensity
n	=	Total number of blows
S	=	Print spacing
$\Delta\varphi/\Delta\varphi b$	=	Friction angle ratio
$\Delta\varphi b$	=	Increase in angle beneath the pounder
DSM	=	Dynamic settlement modulus
D	=	Tamper diameter
pt	=	Impact stress
dt	=	Tamper displacement
ηb	=	Area-normalized depth of improvement
z	=	Depth
z1.2	=	Depth of improvement for a tamper radius of 1.2 m
Ie	=	Normalized improvement factor
Δe	=	Change in void ratio

e0	=	Initial void ratio
H	=	Layer thickness
OWC	=	Optimum water content
$\lambda_{d_{max}}$	=	Maximum dry density
W	=	Water content

TABLE OF CONTENTS

CHAPTER 1

INTRODUCTION

1.1 GENERAL

Sites which were previously considered unsuitable for urban development, due their inadequate bearing capacities, are now being used thanks to ground improvement techniques. One such technique, which is both efficient and cost effective, is dynamic compaction.

Compaction allows for the improvement of a soil's bearing capacity by increasing its unit weight. This is achieved by applying mechanical energy to the soil at its surface which in turn reduces its void ratio, therefore making compaction an essential component of foundation construction. Some of the deterioration exhibited by road infrastructures and building structures can be directly attributed to poor compaction, such as foundation cracks in building structures due to weak soil bearing capacity or poor compaction of bearing strata.

There is currently no theory allowing one to estimate how much of the applied compaction effort is actually transmitted to the subgrade layer in the field by using preliminary laboratory data obtained via Proctor tests.

1.2 PROBLEM STATEMENT

This thesis aims at comparing the differences between the boundaries of a Proctor test for soil compaction with those of dynamic field compaction in order to determine whether or not the Proctor test can be used to predict field compaction and at examining

the role played by the underlying layer with respect to the compaction of the targeted upper layer. Thus, this thesis presents experimental data for various Proctor tests and a numerical model which simulates the Proctor test. The experimental data will be used to validate the developed numerical model. The numerical model is subsequently modified to first remove the Proctor mold's base (laterally confined model), replacing it with a deep deposit and then to remove all Proctor mold conditions in order to simulate the field case of a thin subgrade layer overlying a deep deposit undergoing dynamic compaction.

1.2.1 BOUNDARY CONDITIONS

The modified Proctor test allows for the compaction of a soil sample in one-dimension (see fig. 1a), whereas dynamic compaction performed in the field is a three dimensional process (see fig 1b). That is, the Proctor test imposes boundary conditions on the tested soil sample which are not representative of the field boundary conditions. The Proctor test mold surrounds the soil sample, thereby imposing a radial constraint, and its base confines the sample at its lower limit. A soil element undergoing compaction in the field would experience different boundary conditions; the surrounding soil allows for three dimensional deformations to take place, all depending on the surrounding soil's properties.

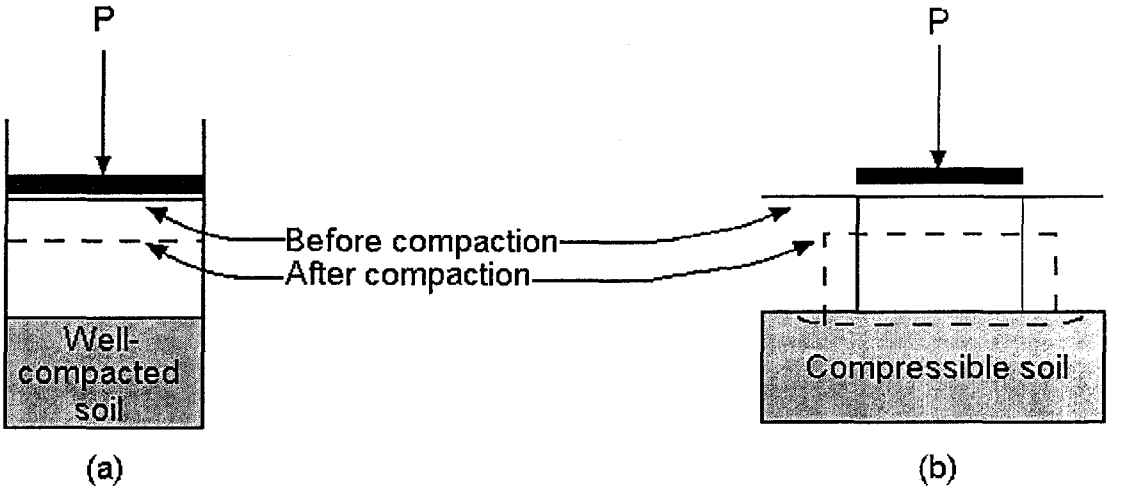

Figure 1.1: Boundary conditions of a soil element subjected to compaction:

(a) Proctor test laboratory conditions; (b) field boundary conditions (Hanna, 2003)

1.3 DYNAMIC COMPACTION

Dynamic compaction is a highly efficient ground improvement technique that densifies loose granular materials (Nashed et al, 2006). High energy impacts are repeatedly applied to a soil's surface by dropping heavy weights, of 4 to 40 tons, carried by cranes from heights ranging from 5 to 40 m in a grid pattern (Nashed et al, 2006, Rollins et al, 1998 and Lee and Gu, 2004). This in turn causes the compaction of the underlying ground; the repeated impact of the dropped weight causes high intergranular stresses and ground vibration, which results in grain skeleton deformation, intergrain slippage, particle rearrangement, reduction of the void ratio, and an increase in the soil's relative density (Nashed et al, 2006).

This technique is very effective in densifying loose granular deposits, such as sandy materials and granular fills, as materials composed of cohesive materials are not suitable

due to their low permeability and long drainage paths for excess pore water pressure dissipation (Chow et al, 1990).

Dynamic compaction is still rather empirical in its use; the selection for tamper weight, drop height, impact grid spacing and the required number of passes for a given site are mainly based on previous experience or field test programs (Nashed et al, 2006). The maximum depth of improvement that can be achieved via dynamic compaction is calculated from the following:

$$d_{max} = n\sqrt{WH} \quad \text{.....(1.1)}$$

where W is tamper weight in tonnes, H is the tamper drop height in m and n is an empirical coefficient whose value ranges between 0.3 to 0.8, which accounts for soil type, dropping mechanism and groundwater level (Nashed et al, 2006 and Chow et al, 1990). However, as noted by Lee and Gu, 2004, there is no clear means of determining n, nor is it certain that a single coefficient accounts for the effects of the many factors which may affect the dynamic compaction process (Lee and Gu, 2004). Although the value of n has been correlated to soil permeability, the effects of other factors, such as tamper area and soil compressibility, are still largely unknown (Lee and Gu, 2004).

Dynamic compaction has been successfully used to densify a wide range of soils to depths exceeding 10 m (Lukas, 1986 in Rollins et al, 1998). This technique is also being used to reduce the risk presented by collapsible soils, but this treatment requires the use of significantly higher energy application levels in comparison to those applied to non-collapsible soils (Rollins et al., 1998).

1.3.1 SEISMIC WAVES IN DYNAMIC COMPACTION

There are two main groups of seismic waves which can travel through a soil medium; (1) body waves and (2) surface waves (Athanasopoulos et al, 2000). Body waves travel within the interior or along the ground's surface and are composed of compressional and distortional waves, also respectively known as P-waves and S-waves (Athanasopoulos et al, 2000). Surface waves are composed of L-waves, which are out-of-plane Love waves, and R-waves, or in-plane Rayleigh waves. Dynamic compaction is chiefly concerned with three types seismic waves; P-waves, S-waves and R-waves (see figure 1-2), as these are the waves that are propagated through the surrounding soil upon the impact of the falling weight (Nashed et al, 2006).

R-waves are the dominant type with increasing distance from the vibration source, as they have a lower attenuation rate and a high vibration energy percentage (Athanasopoulos et al, 2000). It was found that the velocity of Rayleigh waves in layered soils is frequency dependent, making the R-waves dispersive in this case (Athanasopoulos et al, 2000).

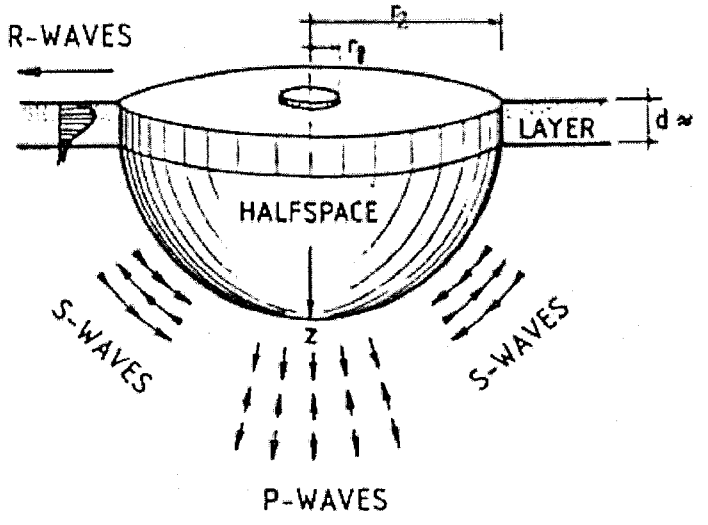

Figure 1.2: Seismic waves in dynamic compaction (Nashed et al, 2006).

Seismic waves are attenuated via geometric and material damping, where geometric damping is due to the loss of amplitude of waves due to their spreading out and material damping is caused by absorption into the soil (Das, 1993). It should also be noted that when a wave encounters a boundary between two soil layers, the wave will be reflected and/or absorbed, all depending on the applied energy level, the depth to the boundary and the mechanical properties of the soil composing each of the layers.

When seismic waves travel from a weak soil layer to a strong soil layer, that is from a layer of low impedance to one of high impedance, the waves are reflected back into the weak soil layer, thereby causing its densification (Hanna, 2003). However, if the underlying layer has lower impedance than the overlying layer, the layer interface between the two becomes energy-transparent (Hanna, 2003). This in turn has for effect that the overlying layer will only be partially compressed, as the amount of compression achieved depends on the respective impedances of the layers (Hanna, 2003).

There is also some limited data available which suggests that vibrations experienced during dynamic compaction may be reduced by increasing the natural moisture content of the soil (Rollins et al., 1998).

1.4 PROCTOR TEST

The Proctor test is a standardized procedure which allows for the determination of the optimum moisture content for compaction of a given soil. The present thesis deals with the modified Proctor test, which uses a soil sample, placed in a steel mold, compacted in 5 layers. The compaction performed during this test is one dimensional (confined compression) (Hanna 2003 and ASTM D1557-00). The importance of the

results provided by this type of compaction test lies in the fact that the compaction water content strongly influences the final soil properties (Walsh et al, 1997).

1.5 RELATING PROCTOR TEST RESULTS TO DYNAMIC COMPACTION

Dynamic compaction is typically performed at a soil's natural moisture content (Rollins et al., 1998). It has been demonstrated that the efficiency of dynamic compaction is related to the soil's moisture content (Liasu and Varskin, 1989; Rollins and Rogers, 1991 in Rollins et al, 1998). This further indicates that an optimum moisture content exists for soils treated by dynamic compaction (Rollins et al., 1998). Care must be taken in the selection of the moisture content, as too high a level will result in the generation of large pore water pressures upon impact and low densification (Rollins and Rogers, 1994 in Rollins et al, 1998). There is currently little literature available on the optimum moisture content for dynamic compaction of non-collapsible soils.

1.6 OBJECTIVE OF THE THESIS

This thesis will first present a review of the literature available with respect to the problem statement. Using the results obtained via modified Proctor tests and a numerical model for a subgrade layer overlying a deep deposit it will be demonstrated that the boundaries of the Proctor test and of dynamic field compaction are incompatible. The impact of the underlying layer upon the field compaction of the overlying layer will also be examined in terms of the deep deposit's modulus of elasticity and the thickness of the subgrade layer. A discussion of the experimental set-up and procedure used will also be presented.

CHAPTER 2

LITERATURE REVIEW

2.1 GENERAL

The available literature dealing with dynamic compaction is generally limited to discussions of equipment-dependent factors, such as tamper diameter and area, rather than site-dependent factors, such as the underlying soil properties. There are currently few reports dealing with optimum moisture or the strength of the underlying layer within dynamic compaction.

2.2 VIBRATION WAVES IN DYNAMIC COMPACTION

Lukas (1980) noted that although a large amount of energy is transmitted to the ground directly below the tamper in dynamic compaction, there is still some energy which is transmitted through the ground to off site locations. He proposes a method whereby measurements are taken on site using a portable seismograph at varying distances from the point of impact and then plotted on a chart as scaled energy versus particle velocity for a particular site. The obtained data can then be extrapolated in order to determine the distances that the tamper points should applied at with respect to existing structures.

It is important to determine how much and how far the applied compactive energy acts in order to minimize potential damage to existing structures. However, the method

proposed by Lukas requires that measurements be taken on site while the work is ongoing.

Peak particle velocities (PPV) are used to evaluate damage to structures by measurements obtained using a velocity recorder seismograph (Mayne et al., 1984). Mayne et al. (1984) compiled available PPV data from various dynamic compaction projects and developed the following relationship for a conservative upper limit for preliminary ground vibration levels:

$$PPV \leq 7\left(\frac{\sqrt{WH}}{d}\right)^{1.4} \quad \text{..... (2.1)}$$

where PPV is in cm/sec, d and H are in meters and W is in tonnes.

Mayne (1985) studied ground vibrations during dynamic compaction. He found that dynamic compaction is characterized by low-frequency waves which are potentially more damaging than high frequency waves and that are below the frequency range of many commercially available vibration monitor seismographs.

Mayne noted that an approximate analysis of ground vibrations, such as harmonic motion which is generally assumed for simplicity to represent the magnitude of ground vibrations, is usually sufficient even though real motions are more complex than sinusoidal waveforms.

The frequency range for dynamic compaction is given as being between 2 to 20 Hz. A first order estimation for the vibration frequency f_n obtained via dynamic compaction is given:

$$f_n = \frac{1}{T} = \frac{1}{2\pi}\sqrt{\frac{k}{m}} \quad \text{..... (2.2)}$$

where

T= period of vibration

$k = \frac{4Gr_0}{1-\nu}$ = vertical stiffness of the system

G= shear modulus

r_o=radius of the mass

υ=Poisson's ratio

m= mass of weight= W/g

g= gravitational constant = 9.8 m/sec^2

This equation indicates that low frequency vibrations are associated with loose soils (with low shear moduli) and for larger weights

Therefore, the maximum dynamic stress at the point of impact is given by the following:

$$\sigma_{max} = \sqrt{\frac{32WHGr_o}{\pi^2(1-\nu)}} \cdot \frac{1}{A_p} \qquad \text{..... (2.3)}$$

where A_p is the area of the pounder.

It has been observed that vibration levels increase as the treated area becomes densified. Generally a maximum level of particle velocity is achieved after one or two passes of heavy tamping of about 150 tm/m^2.

Slocombe (1993) notes that a frequency ranges of 5-15 Hz is potentially damaging to structures and services. This range falls within that of dynamic compaction. The author gives the following guide values for resultant PPV at the foundation level for buildings:

- 40 mm/s for structural damage
- 10 mm/s for minor architectural damage
- 2.5 mm/s for annoyance to occupants

Slocombe (1993) further states that it is difficult to predict the level of vibration transmission as it depends on the properties of the soils present at a particular site. Also, one should be cautious when treating soil that is directly underlain by relatively dense sand, gravel or rock, as these types of soils tend to transmit vibrations further in terms of distance with little attenuation.

Slocombe presents three main methods to reduce the effect of vibrations:

1. Reducing the drop height and compensating for this by increasing the number of drops per imprint.
2. Reducing the weight.
3. Excavating a cut off trench

The first method effectively reduces the impact energy and penetration of the vibrations, whereas the third method requires that the trench be dug to the necessary depth which will intercept the surface wave.

Athanasopoulos et al. (2000) studied the attenuation of seismic Rayleigh waves propagating in the ground surface. The size of the area affected by the waves depends on the attenuation rate of the geomaterial that the waves travel through. The Bornitz equation provides for both the effects of radiation and material damping and can be used when the amplitude of vibration is known at a small distance, r_1, from the source:

$$w_2 = w_1\left(\frac{r_1}{r_2}\right)^n e^{-a(r_1-r_2)} \quad \text{.....(2.4)}$$

where

w_1 is the amplitude of vibration at distance r_1 from the source

w_2 is the amplitude of vibration at distance r_2 from the source

n is the attenuation due to radiation damping

and

a is the attenuation coefficient due to material damping (m^{-1}) which is defined as:

$$a = \frac{2\pi fD}{V_R} \quad \text{.....(2.5)}$$

where

V_R is the propagation velocity of R-waves;

D is the damping ratio of the geomaterial;

and f is the frequency of vibration.

The results were produced by generating artificial ground vibrations with known low-amplitude shear wave velocity of soil, V_{so}, versus depth profiles. The spectral analysis of surface waves (SASW) method, a non-destructive, non-intrusive field method that records the time histories of ground vibrations, was used in 17 sites. The waves were generated by dropping a weight of 5 kN on the surface using a backhoe from heights greater than 4 meters. Two (2) receivers monitored the vibrations at 2 radial distances.

From the obtained results, they estimated the values of the frequency independent attenuation coefficient, a_o, as a function of the V_{so} of the soil materials.

First, they estimated the Fourier Spectra of the two time histories recorder by each pair of receivers at distances $r_1=x$ and $r_2=x+s$. The coherence function of the two histories was estimated in order to determine the frequency range having the best quality. It was found that the 2 signals were highly correlated for a frequency range of 0 to 45 Hz, for which a spectral ratio curve was plotted. The curve was plotted in the form of a decay curve, w_2/w_1 versus frequency (fig. 2), and showed a general trend of frequency dependency; that is the value of w_2/w_1 increased with frequency. The experimental data was best fitted by a curve having equation:

$$\frac{w_2}{w_1} = \left(\frac{r_1}{r_2}\right)^n e^{-a_0 f (r_2 - r)_1} \quad \text{.....(2.6)}$$

Where

f = variable frequency of vibration

a_0 = attenuation coefficient due to material damping

n =attenuation coefficient due to radiation damping

n =0.5 for the case of surface waves generated by a point type source at the ground surface.

V_{S0} was used a as an index of ground stiffness. The predominant frequency of ground vibration was found to be of 15 Hz and it reflects the characteristics of the soil profile. From this value, the predominant wavelength was estimated to be of 9 m. It was found that the attenuation due to material damping decreases with increasing stiffness of soils. The equation for the best fit curve for the pairs of a_0-V_{SO1} values is:

$$a_0 = 3.17 \times 10^{-3} \times e^{\frac{-V_{SO1}}{500}} \quad \text{..... (2.7)}$$

which allows for an estimation of a_0 considered to be more reliable than those obtained via other techniques. The values obtained via this equation were compared to available data in literature and were found to be in agreement. This establishes a relationship between the attenuation rate due to material damping of the surface waves with respect to distance from the source and stiffness of the soil.

It should be noted that the frequency range for which the two time histories were highly correlated (0 to 45 Hz) includes that of dynamic compaction (2 to 20 Hz). It has yet to be seen how the proposed relationship specifically applies to material damping in dynamic compaction cases. It would also be interesting to investigate this relationship

with respect to applied energy in dynamic compaction that is the role of material damping with respect to applied compaction effort.

2.3 DAMPING IN DYNAMIC COMPACTION

Ishibashi and Zhang (1993) established unified formulas for dynamic shear moduli and damping ratios for a wide variety of soils. The equivalent shear modulus G is expressed as follows:

$$G = K(\gamma) f(e) \bar{\sigma}_0^{m(y)} \quad \text{.....(2.8)}$$

Where

$K(\gamma)$ is a decreasing function of the cyclic shear amplitude γ, and is unity for very small values of $\gamma(\leq 10^{-6})$;

f(e) is a function of the void ratio *e*;

$\bar{\sigma}_0$ is the mean effective confining pressure;

and power $m(\gamma)$ is an increasing function of γ.

The maximum dynamic shear modulus, G_{max}, is the maximum value of G and is generally obtained for values of $\gamma \leq 10^{-6}$:

$$G_{max} = K_0 f(e) \bar{\sigma}_0^{m_0} \quad \text{.....(2.9)}$$

Where

$K_0 = K(\gamma \leq 10^{-6}) = 1.0$

and $m_0 = m(\gamma \leq 10^{-6})$

From these two equations, the following is obtained:

$$\frac{G}{G_{max}} = K(\gamma)\bar{\sigma}_0^{m(\gamma)-m_0} \quad \text{..... (2.10)}$$

which can be rewritten as:

$$\log\frac{G}{G_{max}} = \log K(\gamma) + \{m(\gamma) - m_0\}\log\bar{\sigma}_0 \quad \text{..... (2.11)}$$

They found the damping ratio D to be a function of G/G_{max}:

$$D = f\left(\frac{G}{G_{max}}\right) = 0.333\left[0.586\left(\frac{G}{G_{max}}\right)^2 - 1.547\left(\frac{G}{G_{max}}\right) + 1\right] \quad \text{..... (2.12)}$$

It was further found that D = 0.333 is the maximum damping ratio for sands at very high shear strain levels $\left(\gamma \geq 10^{-2}\right)$, where G/G_{max} is close to zero.

2.4 MEASUREMENTS OF DYNAMIC COMPACTION

Chow et al. (1990) presented a method which estimates the degree and depth of improvement of loose granular soils having undergone dynamic compaction by matching the pounder's decelerations as computed by a numerical model to those actually measured in the field. The method uses a one-dimensional wave equation model where the soil beneath the pounder is modeled as a laterally confined elastic soil column of length that extends beyond the expected depth of improvement, whereas the confining soil is represented by a series of springs and dashpots. The springs and the dashpots respectively simulate dynamic soil stiffness and radiation damping. Both pounder and soil column are discretized into one-dimensional elements with an axial mode of deformation (Fig. 3). The presented model yielded results which were in agreement with laboratory and field data.

The one-dimensional wave equation model makes use of the damping matrix of the soil column under the form of Rayleigh damping:

$$[C] = \alpha[M] + \beta[K] \quad \text{..... (2.13)}$$

Where

[C] = viscous damping matrix

[M] = mass matrix

[K] = stiffness matrix

α = mass constant

β = stiffness constant

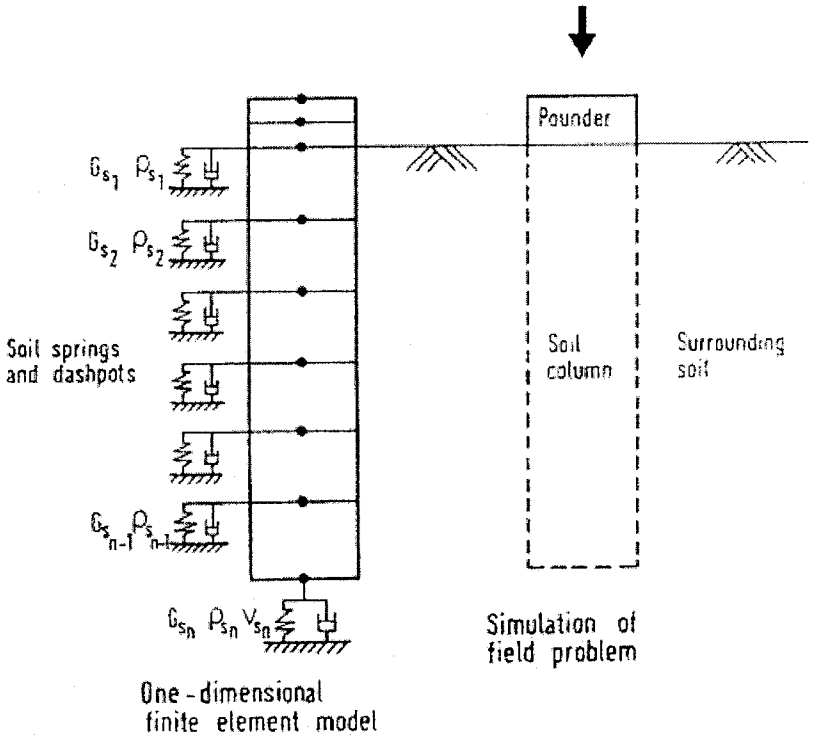

Figure 2.1: Wave equation model for dynamic compaction (Chow et al., 1990)

It should be noted that Chow et al.'s wave equation model is one dimensional and therefore does not account for the lateral spreading of shock-waves (true field conditions), although it is a fair representation of a large scale Proctor test.

2.5 DYNAMIC COMPACTION PARAMETERS

As previously discussed, there are various parameters which affect the effectiveness of dynamic compaction. The following section will present a review of the available literature with respect to these parameters and their use.

2.5.1 GRID AND PRINT SPACING

Mayne et al. (1984) noted the importance of applying compaction energy in the proper spatial and chronological order in order to achieve the desired compaction level. In the first stage of the work, impacts should be spaced at the distance dictated by the depth of the compressible layer, the ground water level and the grain size distribution. It is suggested that the initial grid spacing be at least equal to the thickness of the compressible layer and that up to 50 drops can be used at each impact point.

Chow et al. (1994) presented a method which enables one to predict the lateral extent of soil improvement around the pounder using print spacing. Currently, the improvement experienced by soil having undergone dynamic compaction is measured in terms of applied energy intensity I, which is the total applied compaction energy per unit print area;

$$I = \frac{nWH}{S^2} \qquad (2.14)$$

where

n = total number of blows

W = pounder weight

H =drop height

and S = print spacing, center to center

It should be noted that the impact of the pounder improves the soil properties directly beneath it and, to a lesser extent, that surrounding it, with an effect which reduces with distance from the point of impact or source (Chow et al, 1994). Also, too wide a spacing while maintaining the same applied energy intensity does not adequately compact the soil between impact points (Chow et al, 1994).

Chow et al. (1994) evaluated the increase in friction angles ($\Delta\phi$) of loose granular soils at various distances. As with the compaction of cohesionless soil beneath the tips of driven piles and caissons, the densification of soil via dynamic compaction decreases progressively with increasing distance from the center of the pounder to a lateral distance of about 3.5 times the diameter of the pounder, beyond which there is little densification (Chow et al, 1994). The friction-angle ratios $\Delta\phi/\Delta\phi_b$, where $\Delta\phi_b$ is the increase in friction angle beneath the pounder, obtained at the same lateral distance but at varying depths showed some differences which were not found to be significant. This in turn implies that the ratio of the increase in friction-angle ratios of loose granular soils at a given lateral *X/D* away from the impact center after dynamic compaction is independent of depth:

$$\frac{\phi}{\phi_b} = 1.0; \text{ for } \frac{X}{D} \leq 0.5$$

$$\frac{\phi}{\phi_b} = 0.642 - 1.180\log\left(\frac{X}{D}\right); \text{ for } 0.5 < \frac{X}{D} \leq 3.5 \quad \text{.....(2.15)}$$

$$\frac{\Delta\phi}{\Delta\phi_b} = 0; \text{ for } \frac{X}{D} > 3.5$$

Dynamic compaction is typically executed in a square grid pattern. Chow et al. (1994) found that the two most critical locations, in terms of achieving a uniform level of improvement, are the center of the grid and the middle of the side of the grid. Further, when the print spacing is close, the influence of impacts at neighbouring drop points is significant and should therefore be included in the analysis following the pounding sequence. They presented charts which may be used for the selection of print spacing in dynamic compaction projects in order to achieve a certain level of soil improvement (Chow et al, 1994).

2.5.2 DYNAMIC SETTLEMENT MODULUS

Poran et al. (1992) studied the response of dry sand to the impact of a rigid tamper using an experimental model consisting of a circular steel tamper which was repeatedly dropped on sand contained in a large tank. They developed the dynamic settlement modulus (DSM) which is defined as the slope of the tangent of the loading portion of the impact stress-strain curve:

$$DSM = \frac{\Delta p_t}{\Delta\left(\frac{d_t}{D}\right)} \quad \text{..... (2.16)}$$

where

D = tamper diameter

d_t = tamper displacement

p_t = impact stress

DSM values can be correlated to the density and global elastic moduli of the sand. Based on the DSM concept, they presented a new design method for dynamic compaction of sand which provides estimates of depth and width of the densified soil mass based on tamper weight and contact area, drop height and the number of drops.

2.5.3 IMPROVEMENT DEPTH

As previously noted, eq. 1.1 allows one to estimate the improvement depth that can achieved via dynamic compaction. Lukas (1980) compared the calculated depth of improvement with that measured with standard penetration tests (SPT) and pressuremeter tests. He found the value of n to be of 0.65 to 0.8 and that the improvement of soil properties was not uniform; improvement was greater at high levels and diminished with depth. He further found that depth of improvement did not increase with additional passes, therefore indicating that there is limited soil property improvement which can be achieved.

Mayne et al. (1984) noted that a maximum soil property improvement was achieved at a critical depth, d_c, which then diminishes with depth until d_{max} is reached, below which soil properties remain unchanged.

Although induced settlement is dependent on the total energy input and the way in which it is applied, Slocombe (1993) noted that Mayne et al's (1984) study did not account for the initial softness/density of the soils nor for the proportion of total energy applied by high velocity passes or the low velocity final passes.

Slocombe (1993) further emphasized the importance of the depth of stress impulse in planning treatment operations and transmission of vibrations, the kinetic energy at the point of impact as a major factor in depth of treatment, as increasing the

drop height will increase the drop velocity, and finally that the shape of improvement in the ground is similar to that of the Boussinesq distribution of stresses for a circular foundation.

2.5.4 PASSES AND NUMBER OF DROPS

Mayne et al. (1984) describe the methodology of dynamic compaction, where they define a pass as being the first phase of treatment designed to improve the deeper layers by applying wide spaced impacts. Initial passes or high energy phases are concentrated on points that are at least 3 meters apart and are followed at the end by a low energy pass called ironing, which densifies surficial layers in intervals of 0 to 1.5 meters. After each pass, the site is levelled by filling the craters with surface materials. They further suggested that up to 50 drops could be used per impact point. However, it should be noted that additional pounding will not improve the soil properties once dmax has been reached.

Slocombe (1993) describes an approach whereby the ground is considered to be in three layers. The first pass aims at treating the deepest layer by using a wide spaced grid combined with a suitable number of drops from full height crane capacity. The second pass treats the middle layer using a an intermediate grid, either the midpoint of the first pass or half the initial grid, with both reduced numbers of drops and reduced drop height. Finally, the surface layer is treated with continuous tamping with few drops from a low height. Often times, combinations of the above are used. One can therefore note that the number of passes is quite site specific as is the number of drops.

2.5.5 WEIGHT AND DROP HEIGHT

Mayne et al. (1984) stated that both circular and octagonal weight bases are best suited for primary phases of tamping, as energy is not wasted in forming the circular crater shape, whereas square weights are suitable for ironing phases. The weight and drop height are interdependent; that is the weight of the tamper will increase or decrease its drop height.

It should be noted that the DSM concept developed by Poran et al. (1992) is based on drop height, tamper weight, contact area and number of drops as presented earlier. Lee and Gu (2004) investigated the effect of the tamper base area by normalizing the depth of improvement to that of a corresponding case having the same energy and momentum but with a tamper radius of 1.2 m:

$$\eta_b = \frac{Z}{Z_{1.2}} \qquad \text{..... (2.17)}$$

Where

η_b = area-normalized depth of improvement

$Z_{1.2}$ = depth of improvement of corresponding case with tamper radius of 1.2 m

The authors found that there is an optimal tamper radius r_0 that maximizes the depth of improvement. They found that too small a tamper causes the lateral confinement of the soil directly beneath the tamper to be maintained for a short period, which in turn limits the depth where one-dimensional wave propagation takes place. Also, too large a tamper distributes the impact force over a larger area, effectively reducing impact stress and limiting depth of improvement. They further found that optimum tamper radius increases with momentum and energy blow since an increase in both these parameters causes an increase in the impact force, thereby allowing for a larger tamper base area to

be used before the impact stress falls below the effective level. Finally, the authors noted that zones of high relative density are highly influenced by tamper radius.

2.6 FINITE ELEMENT MODELING IN DYNAMIC COMPACTION

Poran and Rodriguez (1992) developed a numerical model for successive, large deformation impacts applied to the surface of a dry sand mass using a variety of dynamic finite element, finite deformation models in an axisymmetric domain. This model aimed at quantifying the impact induced deep densification and to study its relationship to impact parameters. They noted that there are two major components to modeling dynamic compaction:

1. Appropriately representing the physical mechanism by a mathematical model; and
2. Providing an accurate and computationally efficient solution of the resulting equations.

They used two Drucker-Prager type deviatoric plasticity models with tabulated volumetric plasticity to model soil behavior in an axisymmetric domain for a finite element analysis of the response of dry sand to repeated dynamic compaction impacts. These models were unable to represent the large deformation dynamic response of dense sand. The models were able to approximately represent the behavior of loose sand.

They concluded that the constitutive law of stress-strain relationships of the subject soil is the single most important aspect of their modeling. They further found that there are two viable options for the modeling of repeated impacts that result in large changes in soil density:

1. employing a comprehensive and complex model to represent soil behavior under a larger range of density conditions; and

2. employing a simpler elasto-plastic model together with automated or iterative procedures for mesh refinement and re-assignation of soil model properties.

Also, the authors noted that numerical modeling of dynamic compaction in dry sand is complicated by the fact that large deformations occur in the soil close to the contact area of the tamper.

Zerwer et al. (2002) developed a method that quantitatively evaluates mesh limitations and the damping effects of finite element models (FEM) simulating transient wave propagation, that is for Rayleigh waves in terms of mesh dimensions and attenuation parameters using the Newmark-β method. The effects of mesh filtering are reduced by calibrating the maximum mesh size to the wavelength of the wave having the slowest propagation rate. Propagation velocity decreases for smaller mesh sizes and it increases for smaller time increments.

Two types of attenuation exist in FEM: (1) numerical damping and (2) material damping. They are respectively caused by the integration of Newmark-β parameters and Rayleigh damping parameters. These two types of attenuation must carefully be balanced in order to create an accurate model.

Like Chow et al. (1990), this model uses the standard Rayleigh damping equation (eq. 2.14). The relationship between the damping ratio and Rayleigh damping is given as:

$$D = \frac{\alpha}{2\omega} + \frac{\beta\omega}{2} \qquad \text{..... (2.18)}$$

Pan and Selby (2002) numerically simulated the ground waves generated during dynamic compaction of loose soils using ABAQUS. The system was modeled in two different ways: (1) by applying a force-time curve derived from the product of drop mass

and deceleration time, based on the typical damped half-sine wave form and (2) by applying the impact of a rigid body to the soil surface.

The Mohr-Coulomb failure criterion was used for the axisymmetric soil model for elasto-plastic finite element analysis with a total stress approach (Pan and Selby, 2002). The impact loads were simulated by using first-order four–node elements, which have a lumped sum mass formulation able to model the effect of stress waves (Pan and Selby, 2002). A mesh with approximately 10 nodes per wavelength was used. Pore pressure is not accounted for as the impact duration is only of a few milliseconds (Pan and Selby, 2002).

It was found that the force-time load model provided an overestimate when compared with the empirical estimation of depth of effective treatment of $d = n\sqrt{WH}$, where n was taken to range between 0.5 to 1.0, whereas the rigid body model results agreed with the empirical estimates (Chow et al, 1994). The shape of the force-time plot was taken as being similar to a damped half-sine wave or a normal distribution curve (see Fig 2-2). This in turn has the implication that the simulation method has significant effects on the induced mass penetration or crater depth (Chow et al, 1994). It was further found that the rigid body model yielded superior results for several aspects. Also, the effect of multiple drops was considered by taking into account the first three drops, or blows. The maximum vertical acceleration of the first drop is considered to be much smaller than that of following drops, as the soil is much softer prior to dynamic compaction treatment, yielding a longer impact with a lower peak force (Chow et al, 1994). The peak accelerations for the second and third blows were found to be similar, and the effects of blows beyond that of the first three are limited in terms of

improvement, although it was noted that as blow number increases, the depth of effective improvement increases (Chow et al, 1994). It was further noted that the depth of improvement after the initial three blows was large, with $n = 2.0$ rather than the expected 0.5 to 1.0 range.

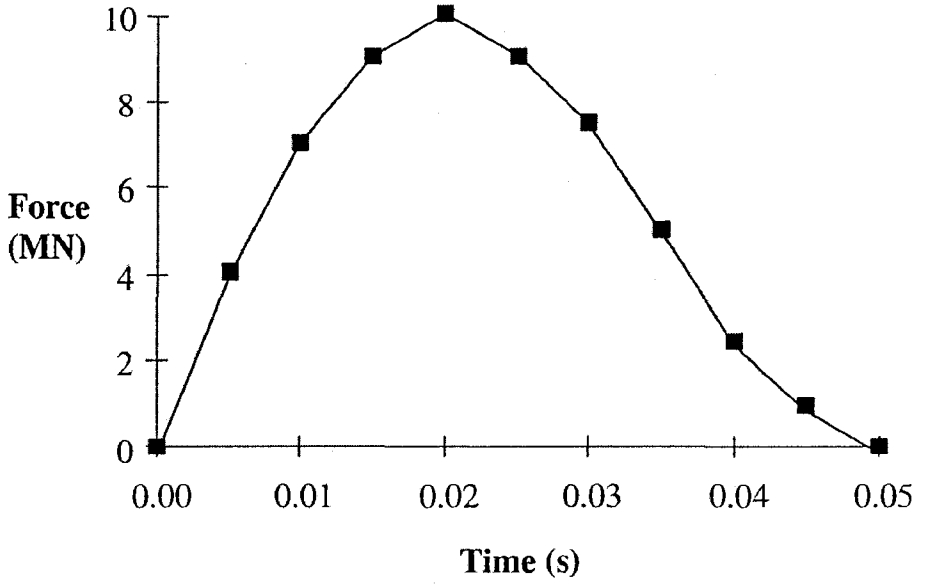

Figure 2.2: Force-time load plot (Pan and Selby, 2002)

It should be noted that Pan and Selby (2002) prefer the use of the Mohr Coulomb criterion rather than the Drucker-Page criterion selected by Poran and Rodriguez (1992). The Mohr Coulomb criterion in comparison to the Drucker Page one assumes that failure is independent of the value of the intermediate principal stress, which is considered to be suitable for most applications even though most geotechnical materials have some small degree of dependence on the intermediate principal stress.

Lee and Gu (2004) proposed a method for the estimation of the degree and depth of improvement resulting from dynamic compaction on sand based on the results from a number of finite element (FE) analyses, which were validated by using centrifuge model

data. The FE studies were conducted using the CRISDYN software. The investigated parameters were the influence of soil properties, initial state, energy per blow, momentum per blow and tamper radius on the depth and radius of improvement. The results of these studies are summarized in a set of curves of normalized depths of improvement, which allow for the prediction of final relative density D_r with depth for any selected tamper area, mass, and drop height.

The impact of the tamper was modeled by taking the tamper to be a stiff elastic block with an initial velocity calculated from the drop height, assuming free fall and using a two-dimensional axisymmetric FE mesh to model the tamper and the ground.

2.7 OPTIMUM MOISTURE CONTENT IN DYNAMIC COMPACTION

Rollins et al. (1998) investigated the effect of optimum moisture content for dynamic compaction of collapsible soils. They performed a series of full-scale dynamic compaction tests at six test cells each having different average moisture contents. The field test procedure was analogous to a large scale Proctor test. They concluded that the optimum moisture content appears to be valid for dynamic compaction of collapsible soils, as it was found that the optimum moisture content generally increased with depth, as compactive energy decreases with depth (Rollins et al., 1998). They further found that the field measured data for both dry unit weight and optimum moisture content was in good agreement with their corresponding lab results (Rollins et al., 1998). They also found that depth of improvement increased slightly and crater depth decreased with increasing moisture content, and they observed that vibrations decreased for compaction performed at higher moisture contents (Rollins et al., 1998).

Rollins et al. (1998) investigated the influence of collapsible soils' moisture on dynamic content by performing a series of full scale dynamic compaction tests at six test cells with different average moisture contents.

The soil tested was composed of sandy silts with thin layers of silty gravel (Rollins et al., 1998). The soil had not been saturated following deposition (Rollins et al., 1998). A 9 m thick layer of collapsible soil was present at the test site (Rollins et al., 1998). Six test cells similar in terms of soil composition were used in the field testing (Rollins et al., 1998).

Initial void ratios ranged between 0.9 to 1.1, whereas the natural moisture content varied between 6 % to 12 % (Rollins et al., 1998). The collapse strain was determined from ring sample obtained at the site and was found to range between 5% to 20% (Rollins et al., 1998).

Laboratory Proctor tests were performed on disturbed samples in order to estimate the optimum moisture content and the range of moisture contents that would be desirable to achieve for the field testing (Rollins et al., 1998).

Lukas (1986) noted that of the energy per volume applied in a standard Proctor test, only 40% to 60% is applied to a site via dynamic compaction. Rollins et al. (1998) expected the applied compaction energy of their study to fall close to the lower end of this range, for which the performed Proctor test results suggested that the optimum moisture content would lie between 16% to 18%.

Two test cells (nos. 1 and 2) having average moisture contents of 7% and 10% respectively were taken as dry samples. Test cells nos. 4 and 5 were moistened via surface pounding to reach 20% to 25% moisture content, which corresponds to 60% to

70% saturation. Test cell no. 3 was found to have an average moisture content of 15%, which is below the optimum moisture content determined via the Proctor tests. Finally, test cell no.6 had an average moisture content varying between 18% to 22%.

From these test cells, it was found that the moisture content varied with depth but it was still deemed adequate for a comparison of moisture content effects on compaction efficiency. CPT (?) testing was performed in the field.

In order to compare field compaction testing with laboratory Proctor tests, Rollins et al. (1998) divided the applied energy by the treated volume, that is they used $D_{max} = n\sqrt{WH} = 4.3m$, with $n = 0.4$ for collapsible soils. Therefore the energy per volume used in the field compaction testing is ≈ 30.2 t-m/m^3, which is $\approx 1/2$ energy per volume used in a standard Proctor test.

Deceleration measurements were taken for the first seven drops at test cells nos. 1, 2 and 4. The two drier cells, nos. 1 and 2, showed an increase in peak deceleration with increasing number of drops, which is contrast with test cell no. 4, where peak deceleration decreased with increasing number of drops. It therefore appears that soil becomes softer with an increase in water content.

The crater depth was measured following each drop and the data obtained indicates a direct relationship between crater depth and soil moisture content. The authors attribute the increase in crater depth with moisture content to the fact that shear strength and penetration resistance decrease as moisture content increases.

Vibration measurements demonstrated that at short distances from the drop point, the PPV generally decrease with an increase in average moisture content.

CPT tests were performed at the center of one drop point in each test cell. Significant improvement was noted for test cells having average moisture content between 15% and 18%. The drier and wettest sites showed less and no improvement respectively.

The measured depths of improvement were generally found to be 10% to 20% higher than predicted by D_{max}.

Undisturbed block samples were retrieved from each test cell in order to determine the level of improvement in terms of unit weight versus initial conditions. Ring samples were taken from the block samples for laboratory determination of void ratio and unit weight as a function of depth for each test cell.

Oedometer collapse tests revealed that reductions in collapse strain are greater when dynamic compaction is performed with water content above that in the dry natural state.

The computed values for Dmax and the applied energy per volume were found to be of 4.3 m and 50% of the Proctor value respectively. In contrast, the field data yielded a Dmax of 4.75 m and the deceleration measurements indicate that only 81% of the theoretical free-fall energy is actually delivered by the tamping weight.

Rollins et al. (1998) proposed that if one accounts for both these factors, the actual applied energy per volume of treated soil is of approximately 35% of the standard Proctor value. That is, the observed field moisture content is expected to best correlate with the laboratory produced moisture–unit curves developed for 1/3 of the standard Proctor energy.

Evaluations of optimum moisture content were performed based on void ratio, dry unit weight, collapse strain and CPT soundings.

The evaluation of improvement based on void ratio was performed by simply determining the area between the pre- and post-compaction void ratio versus depth curves. In order to normalize for initial void ratios variation, the area between the pre and post curves was divided by the void ratio of each layer. The normalized improvement factor (Ie) for each cell was calculated by the following equation:

$$I_e = \sum \left(\frac{\Delta e H}{e_0} \right) i \qquad \text{..... (2.19)}$$

where

Δe = change in void ratio caused by dynamic compaction

e_o = initial void ratio

H = layer thickness

The summation made is from the base of the crater to the depth of improvement Dmax. The calculated Ie value is an indicator of both the degree and depth of improvement. Plots of Ie for each cell versus the average moisture content demonstrated that as the moisture content increased, Ie increased to a peak value of 17%, after which it decreases. This in turn indicates that moisture content is a major factor in achieving a given degree of improvement.

The evaluations of optimum moisture content based on dry unit weights were achieved by computing them at each depth. This was done in order to provide a comparison between field and lab moisture unit weight curves. Plots of dry unit weight

versus moisture content following dynamic compaction also indicate that there is a relation between optimum moisture content and dynamic compaction.

A decrease in maximum dry unit weight and an increase in optimum moisture content with depth below ground surface resulting from the decrease of compaction energy with depth was observed. Similarly, laboratory Proctor testing indicates that optimum moisture content increases as compaction energy decreases. Both of these observations suggest that greater compaction efficiency would be achieved if the moisture content increases with depth, starting at the surface, being the driest point.

Similarly, the evaluations of moisture content based on reduction in collapse strain demonstrated that optimum improvement occurs at 17% and those based on CPT soundings indicate that at a moisture content level drier than the optimum, as this allows for greater improvement.

Lukas (1999) corroborated Rollins et al's findings that demonstrated that the optimum water content should be of 17% in order to achieve the greatest soil property improvement. The author uses data from two projects performed in Indiana.

The first of these sites required that the top 5 feet of a sand lean clay fill deposit be removed following heavy downpour and replaced with crushed stone. The removed soil initially had an average moisture content of 11.7% which increased significantly to values ranging 16% to 17%. The underlying soil, from 5 feet to 10 feet below grade, initially had an average natural moisture content of 13.9%, which decreased to 12.7% following dynamic compaction. This indicates that dynamic compaction dissipated sufficient pore water pressure in order to reduce the moisture content by 1%. This data

agrees with Rollins et al's finding that optimum moisture content increases with depth, as the applied energy decreases with depth.

The second project was one of dynamic compaction performed on a silty sandy clay deposit on another site in Indiana. The dynamic compaction work was done during a drier season, therefore no undercutting was necessary and the average moisture content was found to be of 14.4 %.

The two sets of data further corroborate Rollins et al's theory that dynamic compaction should be performed close to optimum in order to achieve maximum improvement. Lukas further underlines the importance of existing field conditions, particularly moisture content, upon the effectiveness of dynamic compaction; unexpected rainfall may dramatically alter existing field conditions above the desired optimum level.

2.8 DYNAMIC COMPACTION OF A THIN SUBGRADE LAYER OVERLYING WEAK DEPOSIT

Yulek (2006) presented an axisymmetric finite element model which simulates dynamic compaction of a thin subgrade layer overlying a deep deposit. This model, developed using the "PLAXIS" software, assumes that both deformation and stress state are identical in any radial direction.

The model was tested with various stiffness levels for the deep deposit. The compaction effort was represented via the application of impact energy on the ground surface to then be represented as a transient load in the form of a sine wave with a constant frequency and amplitude varying according to the applied energy level. The model was validated using tamper settlement data from the studies of Poran et al. (1992) and Poran and Rodriguez (1992).

Yulek concluded that the presence of a weak subgrade layer substantially affects its compaction, as the applied energy is not necessarily fully transmitted to the subgrade layer due to dissipation. The amount of energy dissipation experienced depends on the weak layer's thickness and stiffness, as well as on the amount of applied energy. The compaction of a subgrade layer was found to increase with increasing depth and energy. Furthermore, it was found that a combination of higher number of drops with a lower energy level allows for an increase in densification of the subgrade. The author provides design charts for practicing engineers to assist in the estimation of the field compaction level of a subgrade layer overlying a deep deposit. It should be noted that Yulek finds that the Proctor test is unsuitable for predicting field compaction, as he finds that there is a lack of compatibility between the boundary conditions of the Proctor test and those of dynamic compaction in the field.

2.9 DISCUSSION

Based on the literature review presented herein, it can be noted that there are limited studies available which deal with optimum moisture content or with the effect of the underlying layer within dynamic compaction.

The downside to the approach presented by Lukas (1980) is that as work is ongoing, there may be damage caused to the existing adjacent structures due to the pounding performed in order to obtain data. Furthermore, as this method requires that seismic wave measurements be taken concurrently with the pounding work, it fails to provide an estimate for the soil's initial conditions.

The wave equation model presented by Chow et al. (1990) is one dimensional and therefore does not account for the lateral spreading of shock-waves (true field conditions), although it is a fair representation of a large scale Proctor test.

Lee and Gu's model (2004) is an improvement over that presented by Chow et al. (1992), as it uses a two-dimensional dynamic finite element analyses rather than the one-dimensional wave model, therefore accounting for lateral spreading of shock waves.

Finally, it is important to recall at this point that the studies performed by Rollins et al. (1998) and Lukas (1999) both deal with the treatment of collapsible soils by dynamic compaction. Collapsible soils by their very nature undergo some level of compaction upon wetting, which is not accounted for in these studies, therefore making it unclear how these findings apply to the treatment of non-collapsible soils by dynamic compaction. Furthermore, although the authors provide an estimate for how much of the compactive effort is actually transmitted to the layer undergoing dynamic compaction, they do not discuss how the applied energy is dissipated. They further do not consider how the soil compacts outwardly (radially) but only in depth. Finally, it would have been interesting to see the effects of print spacing, if any, upon both these studies.

Although Yulek's (2006) study does consider the effects of an underlying deep deposit, he found that the boundary conditions of the Proctor test and those of his model, which simulates dynamic compaction in the field, are not compatible. The model was tested for various energy levels, but not that of the Proctor test. However, the findings of Rollins et al. (1998) and Lukas (1999) demonstrate that there is a correlation between optimum moisture content, as they found that for collapsible soils an optimum moisture content of 17% allowed for the achievement of the maximum depth due to dynamic

compaction. Therefore, using the applied energy of the modified Proctor test within numerical models, it is expected to demonstrate that the boundary conditions of the Proctor test and those of field compaction are not compatible for modified Proctor's energy.

The current study also aims at correlating how much of the applied compaction effort of dynamic compaction is actually transmitted to the subgrade layer in the field by using preliminary laboratory data obtained via Proctor tests. The following chapter will present the experimental procedure and data used towards this purpose.

CHAPTER 3

EXPERIMENTAL PROCEDURE AND RESULTS

3.1 GENERAL

Various soil samples were obtained from various work sites. The obtained samples were taken to a laboratory where they underwent sieve analysis, water content determination and Proctor testing under a controlled setting.

3.2 EXPERIMENTAL PROCEDURE

This section briefly outlines the procedures employed for the experimental portion of this research. The obtained results are presented in the following section of this chapter.

3.2.1 SOIL SAMPLES

The soil samples were obtained from 5 different construction sites in the Laval/ Milles Îles region, as summarized in Table 3-1. All collected samples were classified as being a Class A MG-112 material according to the MTQ's standards, that is a natural sand. The sand material was sampled both before and after compaction in the field by a vibratory roller, as it was generally being used as a foundation layer for various structures, such as highway road and a bridge.

Table 3.1: Sample provenance

Sample no.	Site	Origin	State of sample
1	A-50, Brownsburg-Chatham	Material in place	Post-compaction
2	A-50, Brownsburg-Chatham	Material in place	Post-compaction
3	A-25, Mascouche	Sand quarry	Pre-compaction
4	A-50, Brownsburg-Chatham	Sand quarry	Pre-compaction
5	Préfontaine-Prévost Bridge	Sand quarry	Pre-compaction
6	A-640, Terrebonne	Sand quarry	Post-compaction
7	A-50, Brownsburg-Chatham	Material in place	Pre-compaction
8	Rawdon	Sand quarry	Post-compaction

3.2.2 SIEVE ANALYSIS AND SOIL CLASSIFICATION

In order to classify the soil used according to particle size, sieve analyses were performed as per Transport Quebec's LC 21-040 standard. Sieves with metallic square meshes as per the ISO standard 3310-1 were used. For each sample, the sieves were superimposed in decreasing mesh order starting from the top and the sample was placed in the top sieve. The sifting was performed mechanically by a sieve shaker, which transmits both vertical and lateral movement to the sieves, for a time period not exceeding 10 minutes. The use of the mechanical shaker allows for particles to be bounced around and therefore to be in a different orientation upon meeting the sieve's

mesh, preventing particles from getting trapped in the wrong sieve due to their angularity or position upon encountering the mesh of a particular sieve.

3.2.3 PROCTOR TESTS

Modified proctor tests were performed in order to determine the relationship between water content and the volumetric mass of the soil samples upon compaction in a standard mold with a 4.54 kg hammer having a free-fall height of 457 mm. The optimum moisture content and the range of moisture contents desirable in the field were estimated by performing laboratory modified Proctor testing on disturbed soil samples. Each sample was compacted at constant energy levels with increasing moisture levels as per the procedures outlined in the Bureau de normalisation du Québec (BNQ) standard BNQ 2501-255/2005.

3.2.3.1 EXPERIMENTAL EQUIPMENT

The mold used within the scope of these experiments consisted of a rigid metal cylinder equipped with a detachable collar having a minimum height of 60 mm, which allows for the preparation of the compacted samples to the desired dimensions (Figure 3-1). Both the mold and the detachable collar can be firmly attached to a detachable base plate. The mold has a diameter of 101.6mm and a volume of 935.56 cm^3. Both the height and diameter of the mold are measured after every 1000 uses in order to assure conformity to the respective BNQ standard. A mechanical rammer was used in order to perform the compaction (Figure 3-2). The use of the mechanical rammer insures that a constant compaction force is applied to the sample. The hammer itself has a circular flat pounding surface of 50.8 mm. The mechanical rammer is activated by a device which evenly distributes the drops on the sample's surface. The mechanical rammer is

calibrated after the compaction of 1000 samples as per the ASTM standard ASTM D 2168. The Proctor mold is placed below the mechanical rammer on a rotating base, allowing for even distribution of blows to the sample.

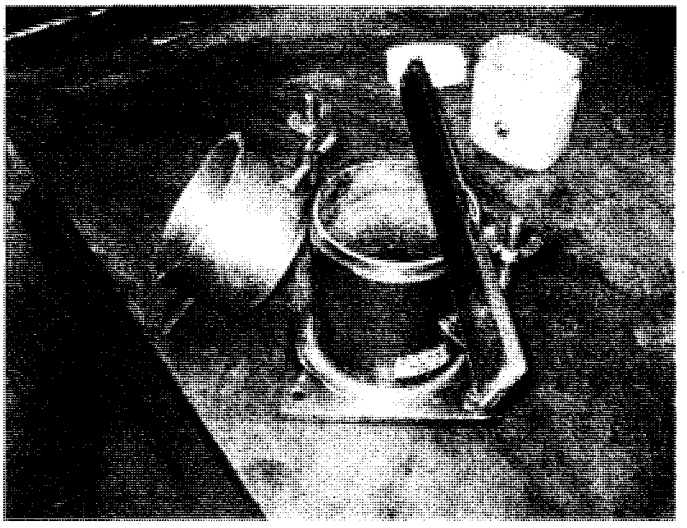

Figure 3.1: Proctor mold with detachable collar and base plate and steel straightedge

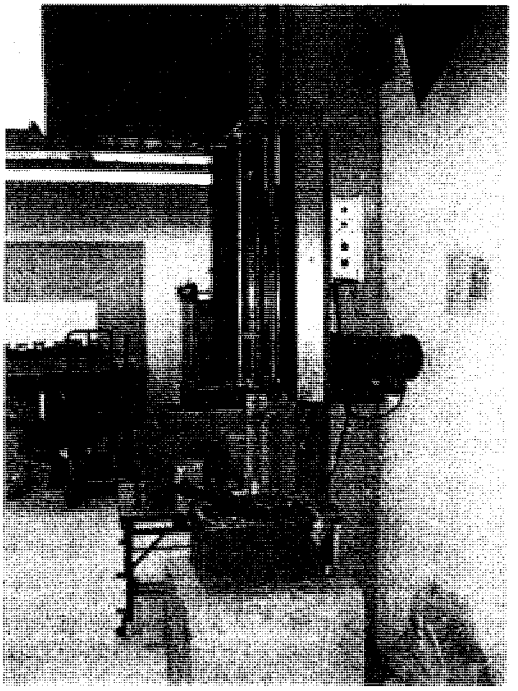

Figure 3.2: Mechanical rammer with internal mechanism displayed

3.2.3.2 SAMPLE PREPARATION

As method A of the BNQ standard was to be used for the Proctor tests, 11 kg of each soil sample were used in order to have a representative quantity of the sample. The samples were air dried prior to sieving and all agglomerations within the sample were broken down, all the while avoiding a reduction in the natural size of the particles.

The dry samples were then each sieved through the 5 mm sieve. From each sample, 4 smaller samples were prepared; initially 2 of these samples were prepared with a 2% difference in their moisture content, in order to determine the range within which to moisten the remaining two samples so as to successfully determine the optimum water content.

Upon the addition of the determined water content, each sample was carefully mixed in order to obtain a uniform moisture distribution. As the soil samples were all classified as being of SP type, there is no requirement to let the samples sit for a given period of time following their preparation. It was therefore possible to immediately proceed to the compaction portion of the experiment.

3.2.3.3 EXPERIMENTAL PROCEDURE

Method A of the BNQ standard was used, which states that all granular material retained on the 5 mm sieve is rejected and that no granulometric correction is required for the grain size distribution of the sample to be subjected to the Proctor test (BNQ, 2005). For each sample, the following outlined procedure was employed:

Vaseline was applied to the inside and outside of the mold at the level of the base plate in order to prevent water seepage during the compaction (Figure 3-3). The dimensions of the mold and the weight of the mold with the attached base plate were all recorded. Each soil sample was compacted in 5 layers by 25 blows of the mechanical rammer (Figures 3-4 to 3-6).

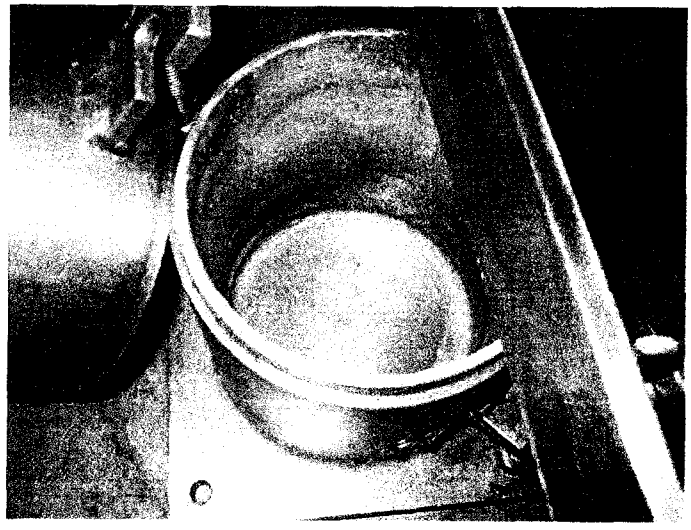

Figure 3.3: Mold with Vaseline at its base

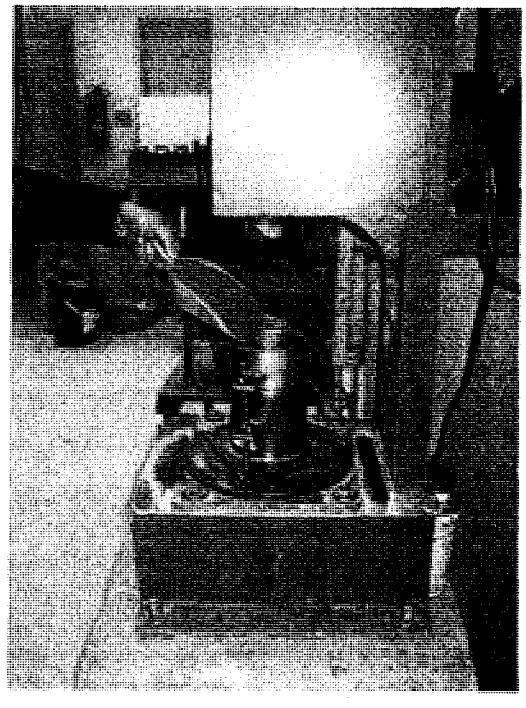

Figure 3.4: Addition of sample for one layer

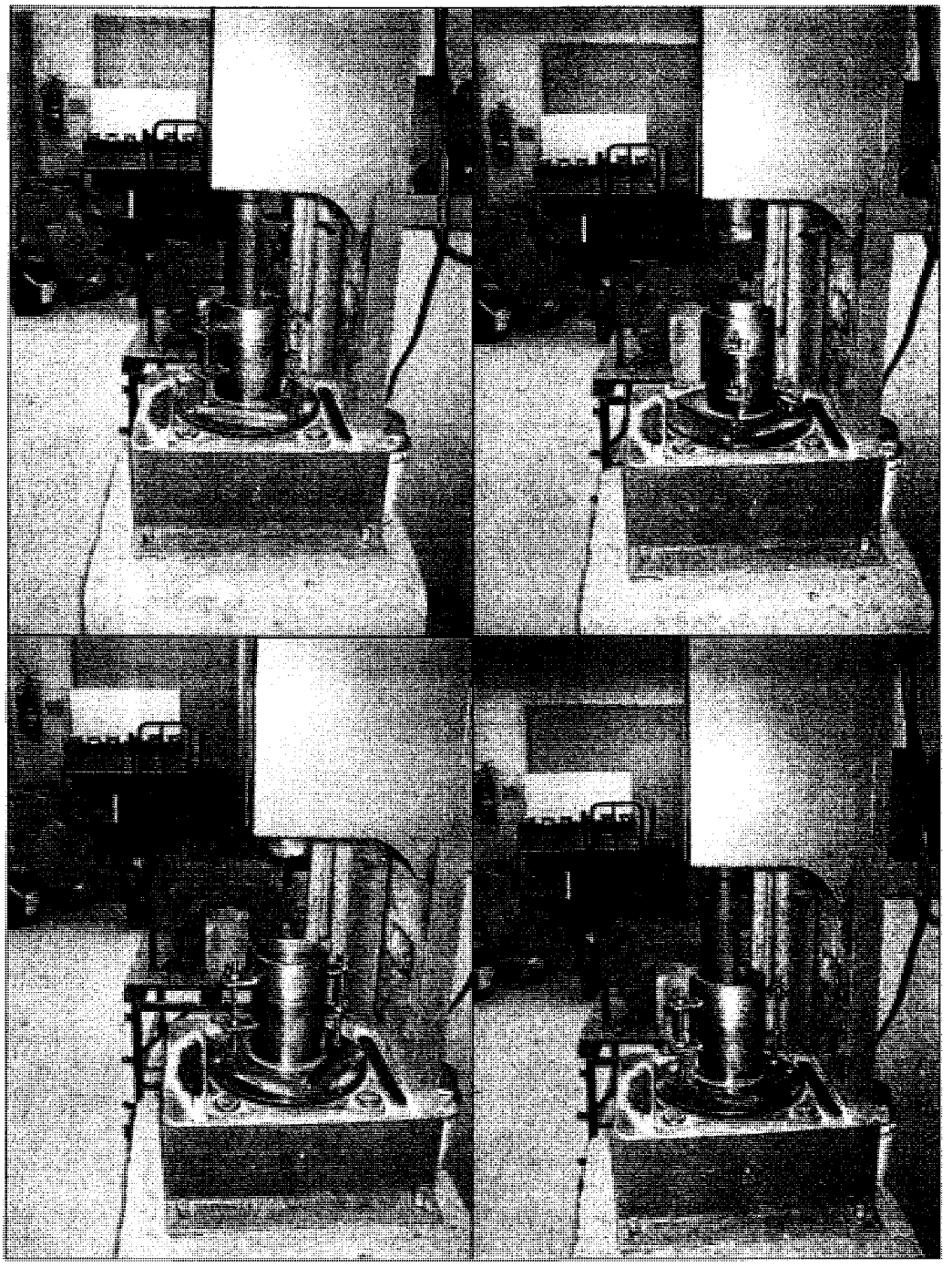

Figure 3.5: Rammer pounding sequence with rotating base

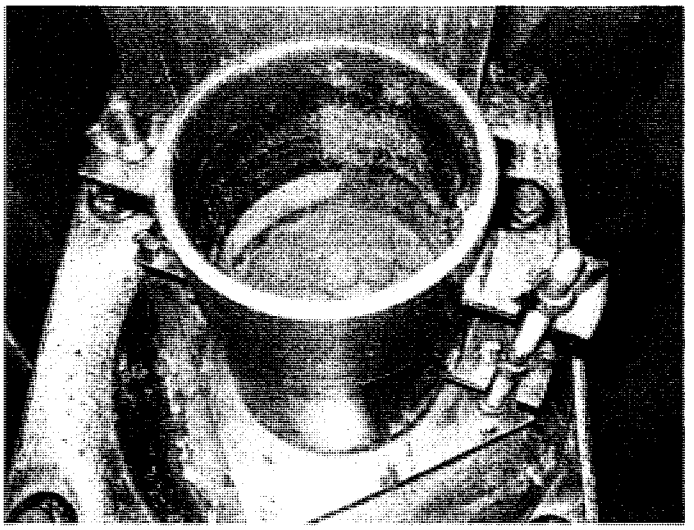

Figure 3.6: Mold with first compacted layer

After the compaction of all 5 layers, the compacted sample was removed from the mechanical rammer and the mold's detachable collar was removed (Figures 3-7 and 3-8). The excess material left over upon removal of the collar was shaved off using a steel shaving ruler. The mold was then cleaned to remove any of the shaved off excess material and/or material having spilt out of the mold onto the base plate during the pounding process (Figure 3-9). The mold and the compacted sample's weight was recorded.

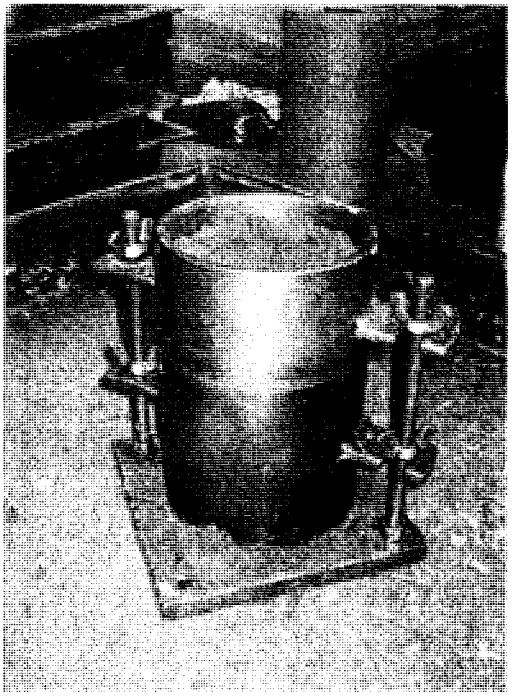

Figure 3.7: Mold with sample compacted in 5 layers

Figure 3.8: Mold after collar removal

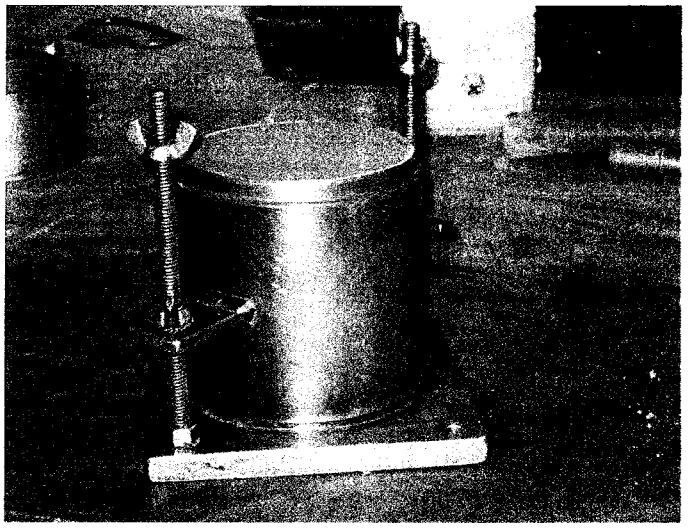

Figure 3.9: Clean mold with excess material removed

The mold was then detached from the base plate and placed inside a numbered pan in order to remove the sample from the mold (Figures 3-10 and 3-11). The pan's number was recorded. It should be noted that the pan's weight had previously been recorded. The weight of the sample and the pan was recorded. The pan containing the sample was then put in an oven at a temperature of 110°C in order to determine the sample's water content (Figure 3-12). Water content determination was performed in accordance to the Transport Quebec standard LC 21-201. The sample was removed after a 24-hour period and the weight of the pan and the now dry sample was recorded. This procedure was repeated for each of the 4 subsamples composing each sample. Finally, the dry unit weight of each sample was computed and then plotted against water content (see figures 3.15 and 3.16).

All results obtained for sieve analysis, water content and Proctor tests are presented in the next section.

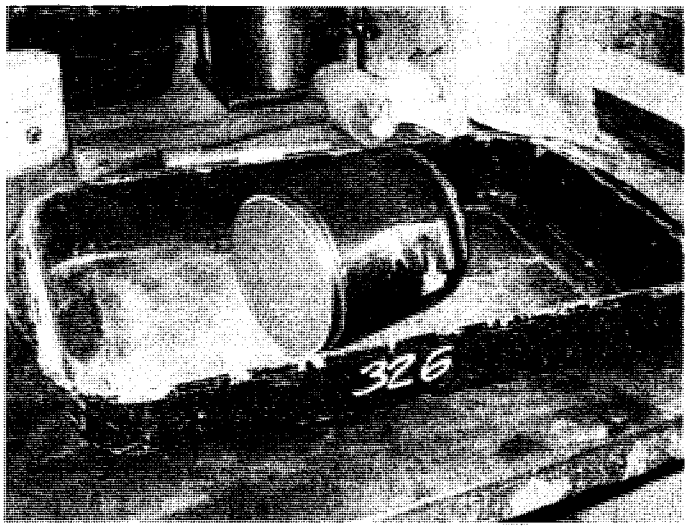

Figure 3.10: Mold with base plate detached

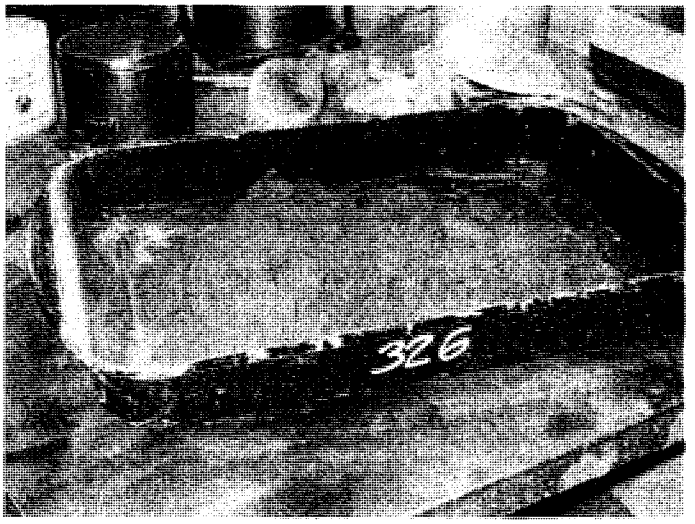

Figure 3.11: Sample extracted from mold

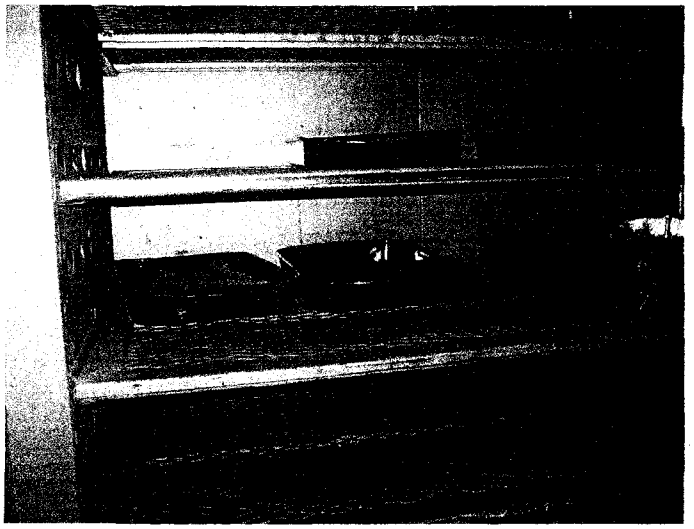

Figure 3.12: Sample placed in oven for water content determination

3.3 EXPERIMENTAL TEST RESULTS

The present section presents the experimental results obtained as well as a discussion of these results.

3.3.1 SOIL CLASSIFICATION

The results of each sieve analysis performed were calculated starting from the cumulative retained mass and/or the individual retained mass per sieve with respect to the dry sample mass. The results are expressed in percentage passing in relation to the total sample and are given with a 1 unit accuracy for sieves above 80 μm and to 0.1% accuracy for samples below 80 μm (Table 3-2). The results of these analyses are depicted in Figures 3-13 and 3-14. From the presented curves it can be seen that all samples exhibited fairly even grain-size distribution. The coefficients of uniformity and of concavity of each sample are summarized in table 3-3.

Table 3.2: Summary of Sieve Analysis Results

Sample No.	1	2	3	4	5	6	7	8
Diam. (mm)	% passing	% passing	% passing	% passing	% passing	% passing	% passing	% passing
112								
80								
56								
40								
31.5								
20								
14								
10								
5							99.7	100
2.5				99.9	99.9	99.9	99.4	99
1.25	100.0	100.0		99.9	99.6	99.2	96.4	98
0.63	99.9	99.9	99.9	99.7	98.1	94.6	80.4	94.0
0.315	98.4	99.3	97.3	97.7	85.2	69.2	31.6	82.0
0.16	32.9	46.0	48.9	73.9	22.6	15.3	6.1	42.0
0.08	0.5	2.3	2.8	1.2	0.5	0.4	0.3	9.5

Table 3.3: Sieve Analysis Properties

Sample No.	1	2	3	4	5	6	7	8
D10	0.10	0.09	0.09	0.09	0.13	0.15	0.19	0.08
D30	0.16	0.13	0.12	0.11	0.18	0.2	0.30	0.13
D60	0.22	0.19	0.19	0.14	0.24	0.28	0.47	0.22
Cu	2.2	2.1	2.2	1.6	1.8	1.9	2.5	2.8
Cc	1.2	1.0	0.9	1.0	1.0	1.0	1.0	1.0

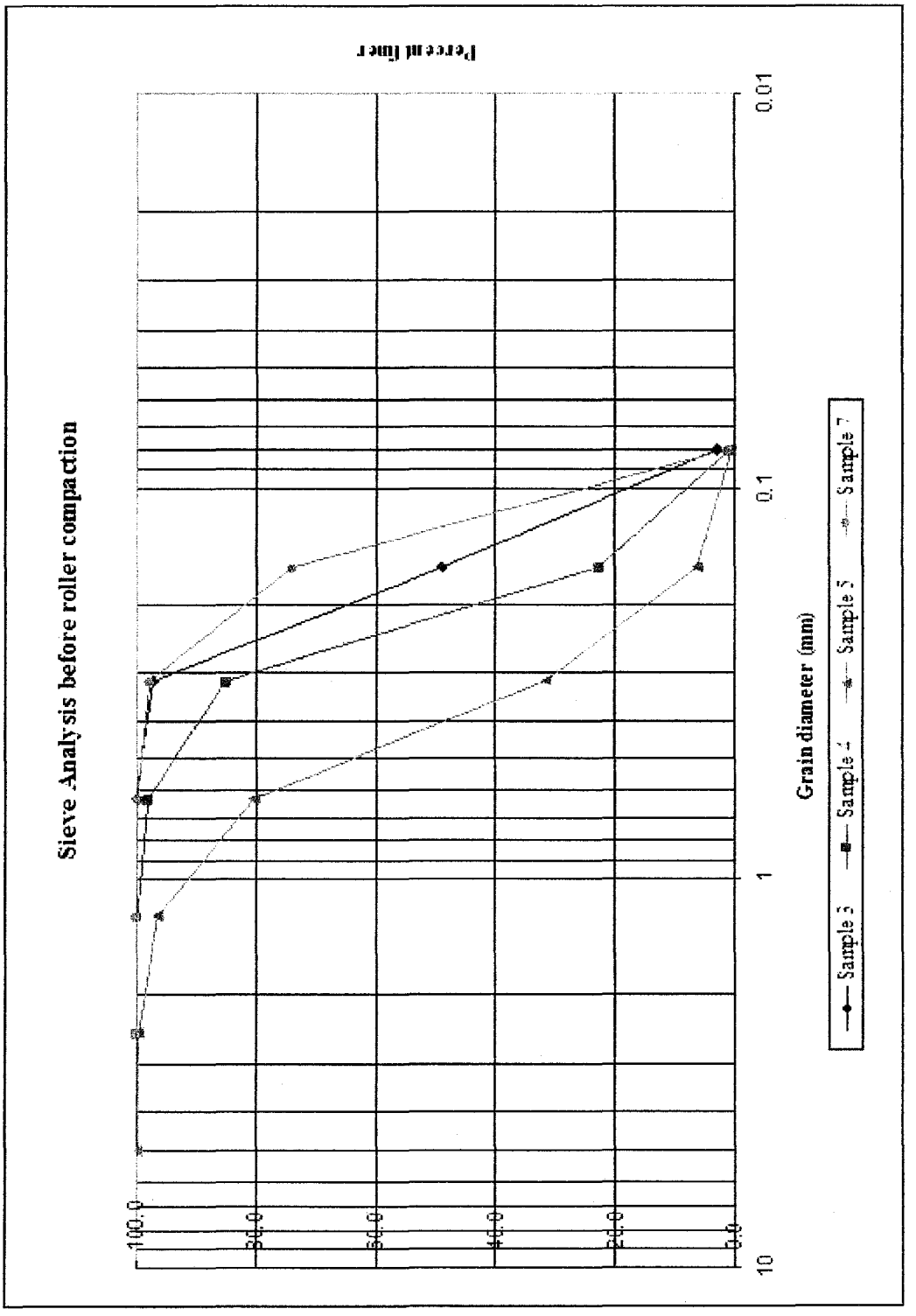

Figure 3.13: Sieve Analysis curves for uncompacted samples

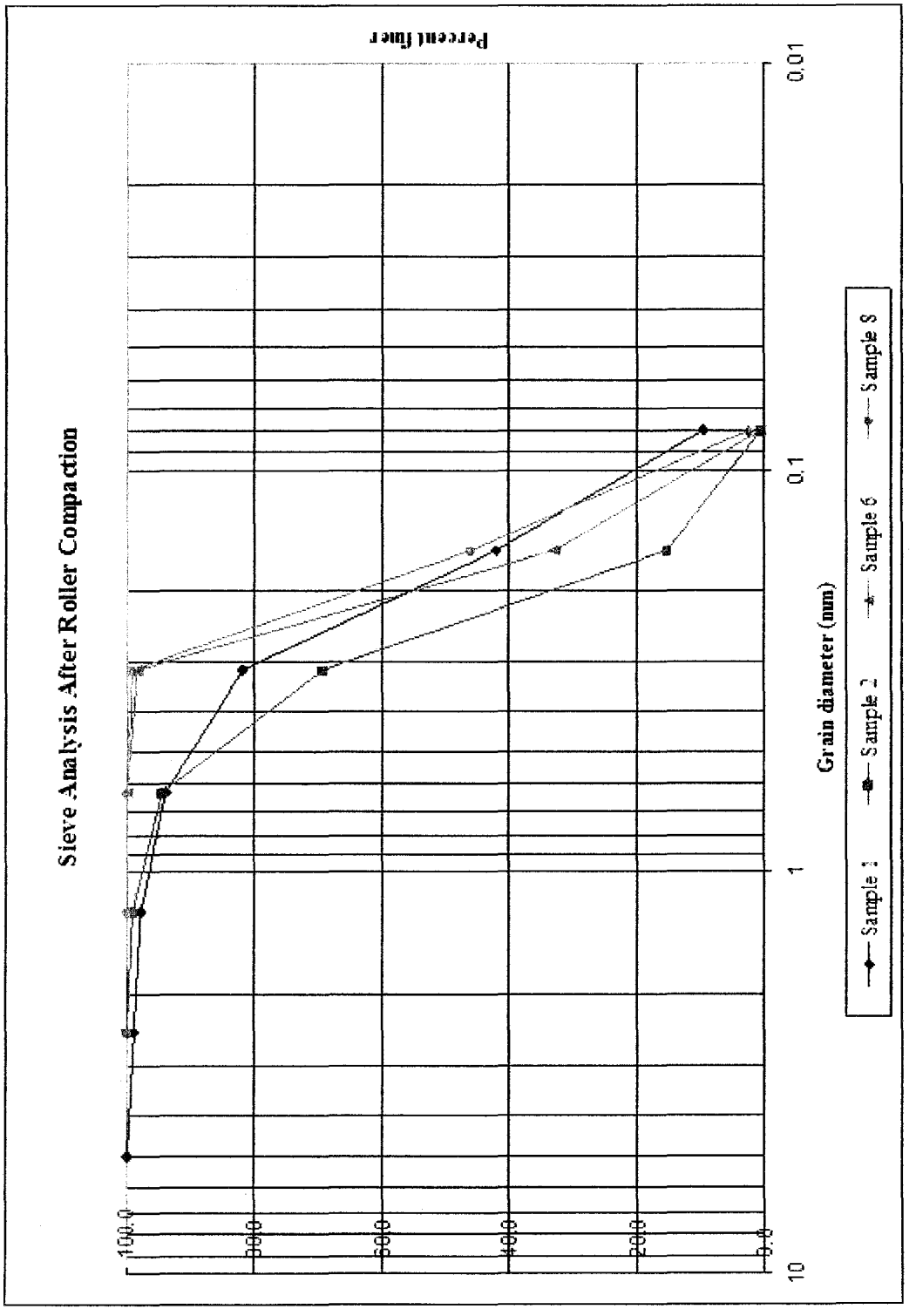

Figure 3.14: Sieve Analysis curves for field compacted samples

3.3.2 PROCTOR TEST RESULTS

Table 3-4 presents the optimum water content, maximum dry density and the average water content of all samples.

Table 3.2: Summary of Proctor tests and water content determination

Sample No.	Optimum water content (OWC)	Maximum dry density (λd max)	Water content (%)	
3	14.0%	16.4	13.8	Before roller compaction
4	15.5%	16.5	14.5	
5	13.3%	16.8	13.1	
7	13.5%	17.7	12.3	
1	13.0%	16.2	12.5	After roller compaction
2	15.3%	16.2	14.0	
6	12.8%	17.1	12.3	
8	12.5%	17.3	12.2	

It can be seen from the above table that the optimum water content values of the samples taken prior to roller compaction are higher (ranging from 13.3 to 15.5 %) than those of the samples taken after roller compaction (ranging from 12.5 to 15.3 %). This is to be expected, as roller compaction would decrease the amount of voids within a soil. However, the handling of the roller compacted samples diminished the compaction level experienced by the soil in the field, which would explain the similarity in the ranges of the optimum water content. The relationships obtained between dry unit weight and moisture content are shown in figures 3.15 to 3.16.

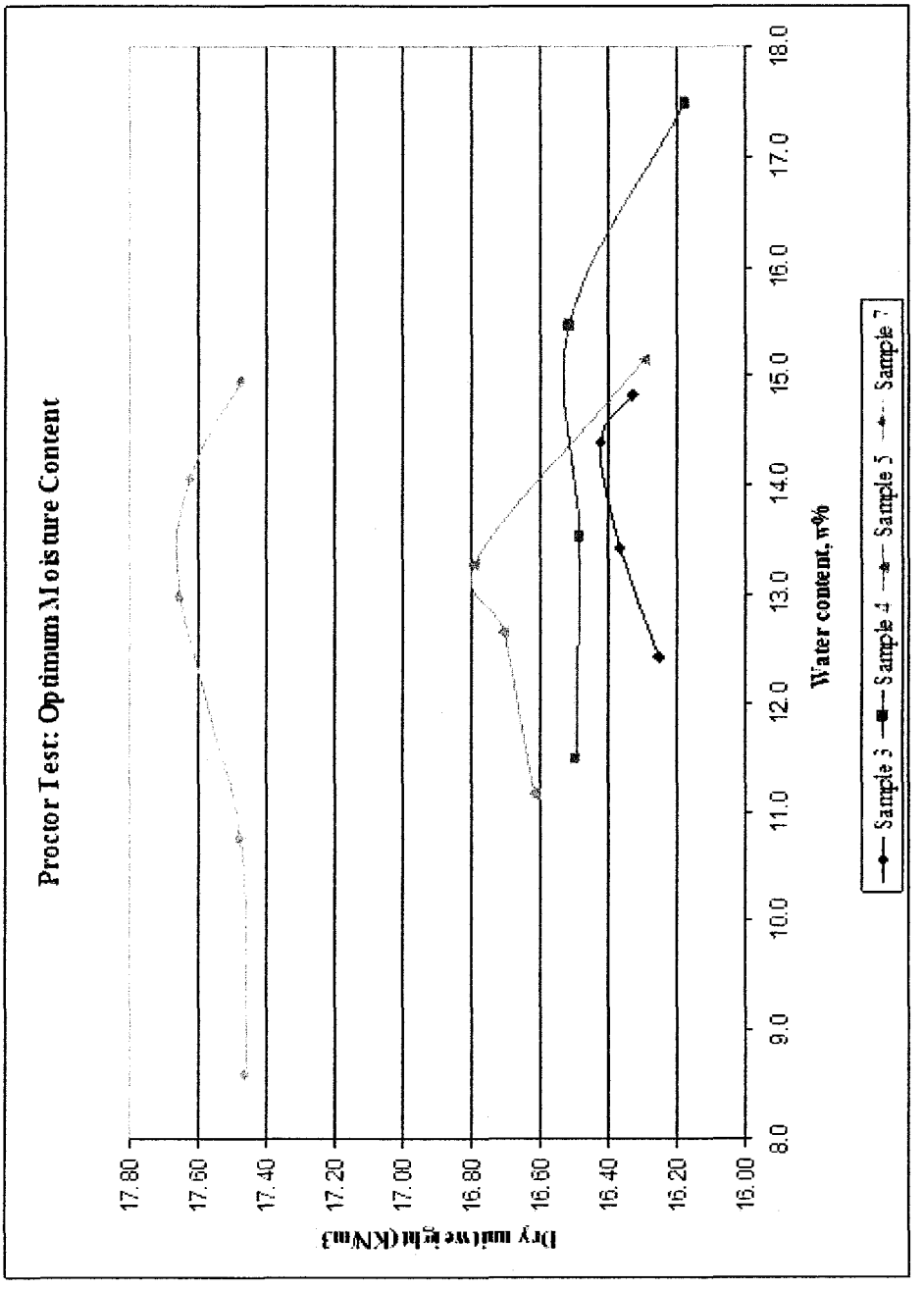

Figure 3.15: Optimum moisture content curves for samples taken before roller compaction

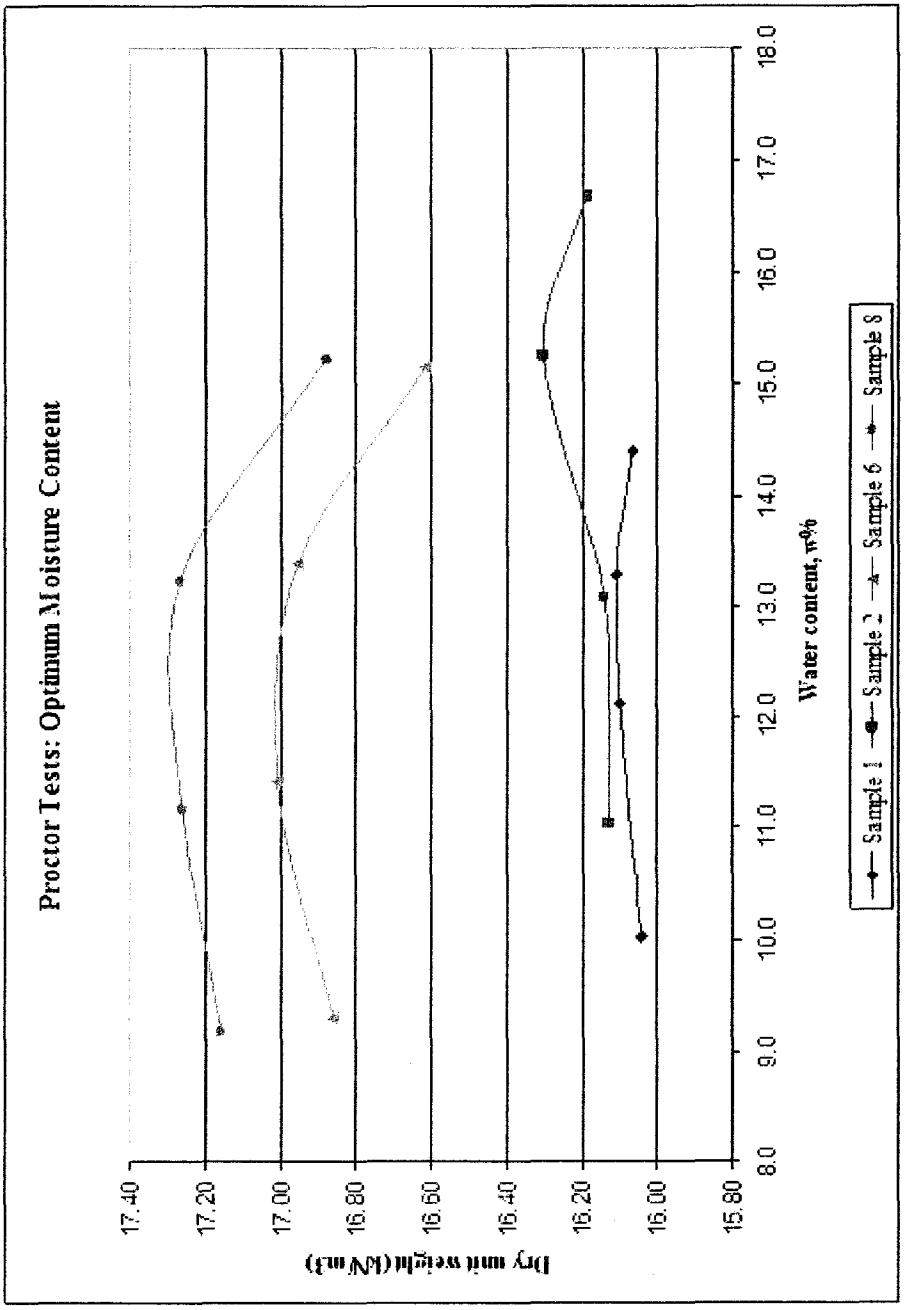

Figure 3.16: Optimum moisture content curves for samples taken after roller compaction

From these figures, it can be seen that the typical increase in dry unit weight up to an optimum moisture content followed by a decrease in dry unit weight was exhibited by the material tested. That is, the compaction energy decreases as the maximum dry unit weight decreases and the optimum moisture content increases.

The data obtained via these experiments will now be used to test the modified numerical model, as presented in the following chapter, in order to find a relationship between the Proctor test compaction level and that of dynamic compaction in the field.

CHAPTER 4

NUMERICAL MODELLING

4.1 GENERAL

In this study, a numerical model of dynamic compaction in a two-layered medium using the same energy as the modified Proctor was developed using the *"PLAXIS" v8.2* software.

4.2 NUMERICAL MODEL

The model consists of an axisymmetric model with 4^{th} order triangular elements of 15 nodes. An axisymmetric model was selected as it allows for both geometrical damping and a realistic representation of dynamic compaction using a circular tamper. It is assumed that deformations are identical in any radial direction (x-axis) at the same level along the axial line of symmetry (y-axis).

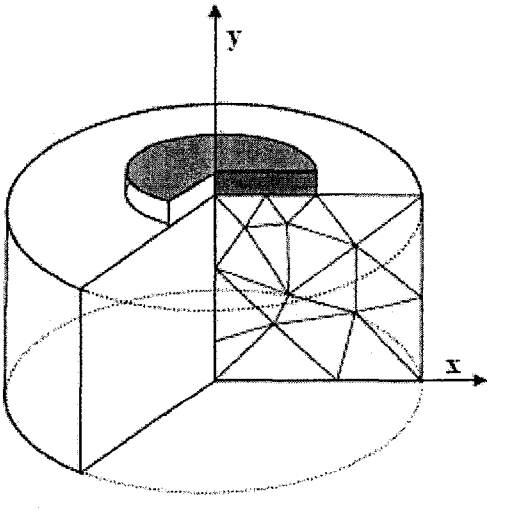

Figure 4.1: Axisymmetric problem (ref. "PLAXIS" v 8.2 Reference Manual)

4.3 MODEL GEOMETRY AND BOUNDARY CONDITIONS

As it is desired to compare the boundary conditions of a Proctor test with field boundary conditions, it was necessary to develop a model for which the boundary conditions were altered. Therefore a base model was created for which the boundary conditions were subsequently altered resulting in 3 types of boundary conditions:

- Proctor
- Laterally confined (underlying soil ranging from loose to very dense).
- Field case: no confinement (underlying soil ranging from loose to very dense).

4.3.1 PROCTOR MODEL

The base model which was developed is intended to replicate the Proctor test. Absorbent boundaries allow for the absorption of stress increments on the boundaries caused by dynamic loading that are otherwise reflected inside the soil body. Therefore, absorbent boundaries were not used for this model, as here it is desired that the seismic waves be reflected back, as is the case during a Proctor test. Also, only one type of soil was used for this portion of the numerical modeling. The soil in this model is in a single layer which is tampered 25 times as in the modified Proctor test. The soil type was modeled using the Soil Hardening Model which allows for changes in soil properties due to the dynamic nature of the problem, that is the stiffness matrix of the soil is updated after each calculation step.

In order to create this model, the dimensions of the modified Proctor mold and tamper were determined by making an equivalent model based on the tamper diameter; the numerical tamper has a diameter of 1 m. The following table shows the applicable Proctor test dimensions and the corresponding numerical model dimensions. It should be

noted that as the model is unisymmetric, some of the model's dimensions are actually half of those reported in the table, such as is the case for the diameter. The model was tested for a soil layer depth of 2.3 m.

Table 4.1: Dimensions

	Proctor Dimensions	Numerical model dimensions
Hammer weight (kg)	4.54	N/A
Drop height (m)	0.457	9.00
Energy (KN/m2)	2700	2700
Hammer diameter (m)	0.0508	1.000
Mold diameter (m)	0.1016	2.000
Number of drops	25	25
Number of layers	5	1
Volume (m3)	0.000944	7.20
Mold height (m)	0.12	2.3

4.3.2 LATERALLY CONFINED MODEL

The model was then modified to include 2 layers of soil which are laterally confined; the top layer uses the Soil Hardening Model, whereas the underlying layer uses the Mohr Coulomb Model, as a deeper layer exhibits less deformation and it has a fixed yield surface, that is the model is fully defined by the model parameters and is not affected by plastic straining. The top layer was taken as having a depth of 2.3 m; the equivalent modified Proctor mold height, whereas the bottom layer's depth was taken as

being infinite, or very deep. The bottom layer was tested for 3 conditions: loose, medium and dense. This allows us to see the extremities of the stiffness range. An absorbent boundary was placed at the base of this model. It is expected that the weak soil will absorb much of the applied energy, therefore not allowing for the top layer to be compacted properly, whereas the very dense layer allows for a better compaction of the top layer by reflecting a portion of the applied energy back.

4.3.3 FIELD MODEL

Finally, the model was modified yet again to simulate dynamic compaction in the field. The model itself was made larger in order to account for geometric damping. This in turn implies that the boundary conditions had to be modified to include absorbent boundaries. It is expected that this model should demonstrate a lower level of compaction, as geometric damping is now allowed to occur, meaning that waves are not reflected back and the soil is not as compacted.

The basic geometry of the model is that of a thin subgrade layer overlying a deep deposit. Both layers are assumed to be sand for a range of stiffness values. The deep deposit has dimensions of 25 m in depth and width and a 2.3 m thick subgrade layer.

4.3.4 DISCUSSION OF BOUNDARY CONDITIONS AND MODEL GEOMETRY

The outer boundaries of the soil media are supported by horizontal fixities at the vertical geometry lines and full fixities at the base horizontal geometry line, as shown in figure 4.2.

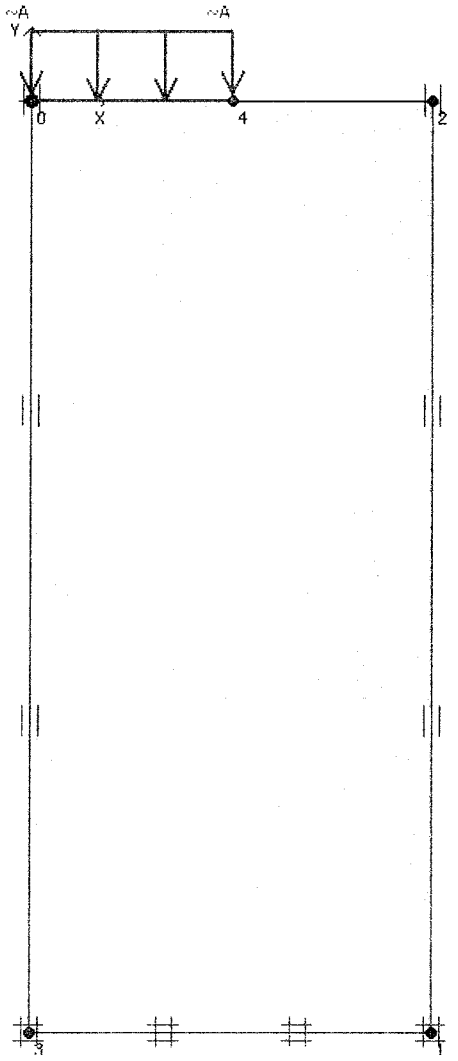

Figure 4.2: Proctor model geometry and boundary conditions

As the applied impact energy and its associated deformations within the soil are concentrated at the point of impact and in its vicinity, mesh refinements were made in this area. The final selected mesh is presented in figure 4.3.

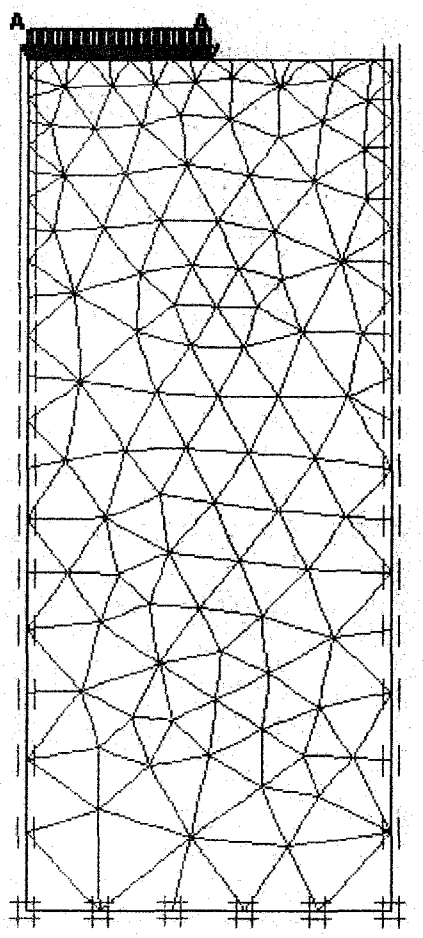

Figure 4.3: Generated mesh with refinements about point of impact

The basic boundary conditions taken were those that replicate the conditions of a Proctor test. Therefore, the base model has horizontal fixities present at the vertical geometry lines and full fixities are employed on the bottom and right fixities.

Considering the dynamic nature of the model at hand, the mechanical properties of the soil and the deformation characteristics are continuously changing during testing. It is for this reason that the Hardening Soil model was selected for the subgrade layer as it allows for the stiffness matrix of the soil to be updated following the completion of each step of the model.

The same model was not used for the underlying layer, as it is a deep deposit and should not exhibit the same level of deformation. Therefore, the deep deposit was created using the Mohr-Coulomb model, which has a fixed yield surface. That is, its yield surface is fully defined by the model parameters and is not affected by plastic straining.

4.3.5 DYNAMIC LOADING

The dynamic load is applied via the base of a 1 m in diameter tamper as a transient load, which is in the shape of a half-sine curve (Pan and Selby,2002) (see figure 4.4). The modified Proctor energy level of 2700 KN/m^{2}was applied as the peak dynamic stress.

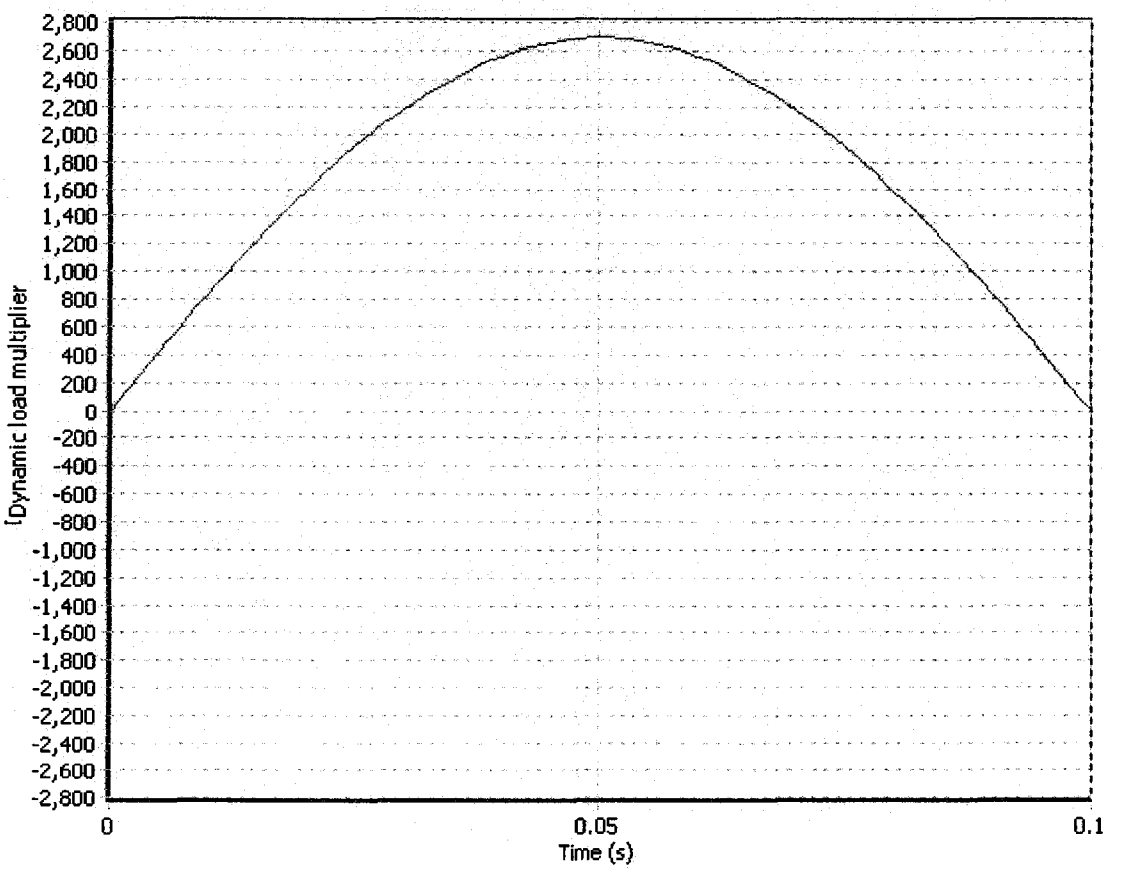

Figure 4.4: Transient load due to impact

The duration of contact for each impulse loading was taken as being of 0.1 second, which corresponds to a transient harmonic load of frequency of 5 Hz and falls well within the typical Dynamic Compaction range of 2 to 10 Hz, and the amplitude is equal to the peak dynamic stress formed upon impact. The unloading time was taken as being twice the loading time, 0.2 second, which allows for the dynamic stress distribution throughout the soil and for all rebound effects at both the point of impact and the interface to take place.

Although the impact duration changes as soil properties are improved, there is no rational means to include this in the model. Peak dynamic stress also changes due to an increase in soil stiffness, but similarly there is no means to quantify this and therefore the change in peak dynamic force is also neglected in the model.

4.4 SOIL TYPES

The top layer was taken as being composed of loose sand using the soil hardening model in "PLAXIS"; this in turn requires the entry of the Oedometer Modulus. This value was obtained using the relation between the modulus of elasticity and that of the oedometer modulus, which is as follows ("PLAXIS" reference manual):

$$M = \frac{E(1-\nu)}{(1-2\nu)(1+\nu)} \quad \text{(4.1)}$$

where E and υ are the modulus of elasticity and Poisson's ratio respectively.

In order to account for the damping ratio of sands, both α and β were used throughout the analysis by approximating the value of G/G_{max}. Since soils exhibit low frequency vibrations and higher deformation and strain while undergoing dynamic

compaction, the dynamic shear modulus is taken as being one tenth of its initial value. Therefore, the value of G/G_{max} for the lower layer will range between 0.1 to 1, which corresponds to a loose to dense soil, where a value of 1 is used for the case of the stiffest soil, where no deformation is expected.

The values of the shear moduli used as well as other parameters used are presented in Table 4.2. It should be noted that these parameters represent 7 different subgrade layers of varying stiffness, and unit weight, corresponding to the experimental values obtained, and 3 other types of underlying layers which ranges from very loose sand to very dense sand. The values were taken to correspond to the average values for loose, normal and dense sands as given by Das (2005).

Table 4.2: Soil parameters used within the numerical model

Soil type	γunsat	γsat	kx=ky	E	M	C	φ	υ	G/Gmax	α	β
Upper layer 1	16.2	17.2	0.00005	6750	7500	0.2	26.1	0.2	0.1	11.87	0.006
Upper layer 2	16.2	17.2	0.00005	6750	7500	0.2	26.1	0.2	0.1	11.87	0.006
Upper layer 3	16.4	17.4	0.00005	15000	20192.3	0.2	26.4	0.3	0.1	11.87	0.006
Upper layer 4	16.5	17.5	0.00005	7500	8333.3	0.2	26.5	0.2	0.1	11.87	0.006
Upper layer 5	16.8	17.8	0.00005	8250	9166.7	0.2	27.0	0.2	0.1	11.87	0.006
Upper layer 6	17.1	18.1	0.00005	9000	10000	0.2	27.4	0.2	0.1	11.87	0.006
Upper layer 7	17.7	18.7	0.00005	10666.7	14358.9	0.2	30.3	0.3	0.1	11.87	0.006
Upper layer 8	17.3	18.3	0.00005	9500	12788.5	0.2	27.7	0.3	0.1	11.87	0.006
Lower layer 1	13.5	15.0	0.00005	2500	-	0.2	25	0.20	0.10	11.87	0.00600
Lower layer 2	19.5	20.5	0.00005	20000	-	0.2	35	0.35	0.70	2.85	0.00144
Lower layer 3	20.0	21.0	0.0005	65000	-	0.2	45	0.45	1.00	0.545	0.00028

4.5 MATERIAL DAMPING RATIOS

In "PLAXIS", material damping within the soil models includes friction and the development of plasticity but not viscosity. In order to make up for this, a damping term that is proportional to the mass and the stiffness of the system is assumed, where:

$$C = \alpha M + \beta K \quad \text{..... (4.2)}$$

where C is the damping, M the mass, K the stiffness and α and β are the Rayleigh damping coefficients.

The damping coefficients can be determined from two given damping ratios that correspond to two frequencies of vibration. Due to the dependence of the damping ratio on the soil's dynamic shear modulus, the damping ratio was taken as a variable governed by the in-situ shear of the soil, rather than the frequency. To this effect, G/Gmax in formula 2.12 was taken as ranging from 0.1 to 1 in order to calculate the damping ratio of the different subgrade and underlying layers according to the expected level of deformation created by the dynamic compaction process. The following formula was used to quantify the Rayleigh damping coefficients:

$$D = \frac{\alpha}{2\varpi} + \frac{\beta\varpi}{2} \quad \text{..... (4.3)}$$

It should be noted that the same damping ratio for the respective soil type was used for both frequency levels of 5 and 10 Hz, which are common vibration impact levels in the compaction of soil.

4.6 NUMERICAL MODEL ASSUMPTIONS

The following assumptions are made with respect to the numerical model presented herein:

1. Regardless of the type of soils composing the layer(s), upon application of the compaction energy, the upper layer will absorb or filter the same amount of energy and transfer the remainder to the lower layer.
2. As energy waves reach the interface between the 2 layers, some energy is absorbed by the lower layer and some is reflected back into the upper layer. The highest degree of compaction is achieved when all of the energy is reflected back into the upper layer (upper boundary). Accordingly, the lowest level of compaction is achieved when all of the applied energy is absorbed by the lower layer (lower boundary).
3. The level of compaction obtained in the upper layer is a function of the energy lost to the lower layer. Therefore, the less energy lost to the lower layer, the higher the degree of compaction achieved.
4. For the modelization of the field, the boundaries are placed far away from the point of impact in order to avoid spurious energy wave reflections. However, this is not the case when modeling the Proctor or laterally confined conditions, as it is desired to have energy waves reflected back into the soil medium.

4.7 NUMERICAL MODEL VALIDATION

The developed numerical model was validated using the experimental Proctor test data. That is, the various dry unit weights used to determine the optimum water content for each sample were input into the model. The resulting vertical deformations at the point of impact were plotted against the known moisture content corresponding to the dry unit weights used in the Proctor tests, as shown in figures 4.4 to 4.12. The optimum moisture content for each sample was then obtained by taking the highest point of the best fit curve, as the maximum dry unit weight yields the smallest vertical deformation at the point of impact. The numerical results for optimum moisture content were then compared against the experimental results, as summarized by Table 4.3.

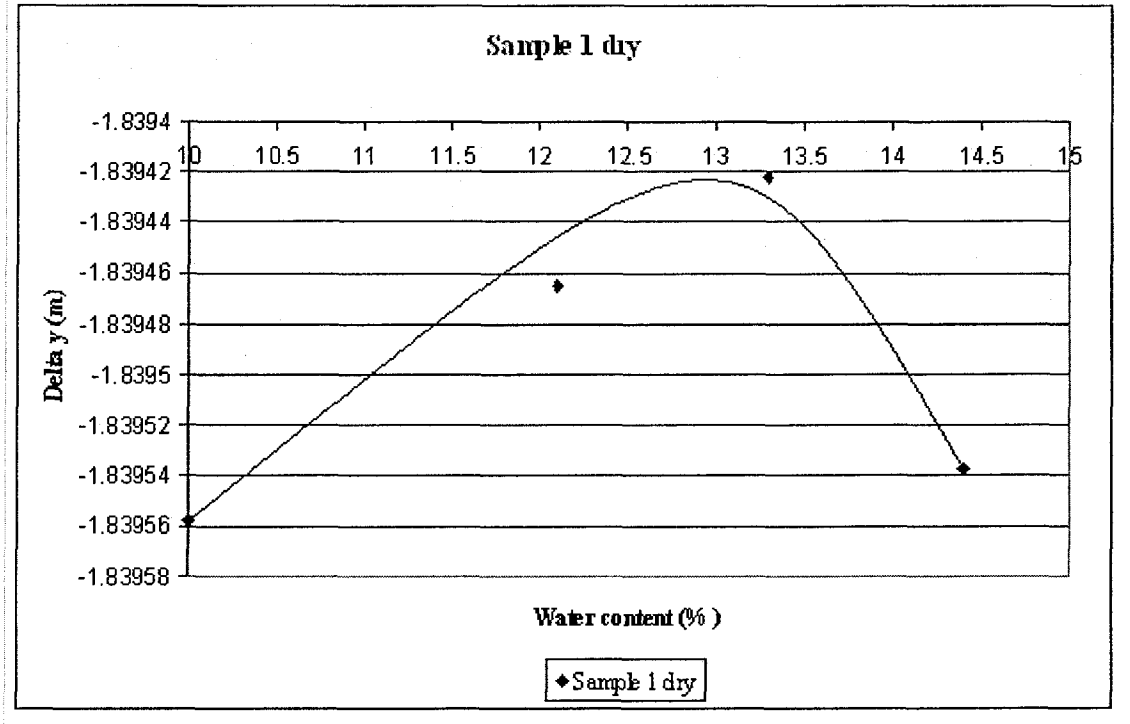

Figure 4.5: Validation curve for Sample 1

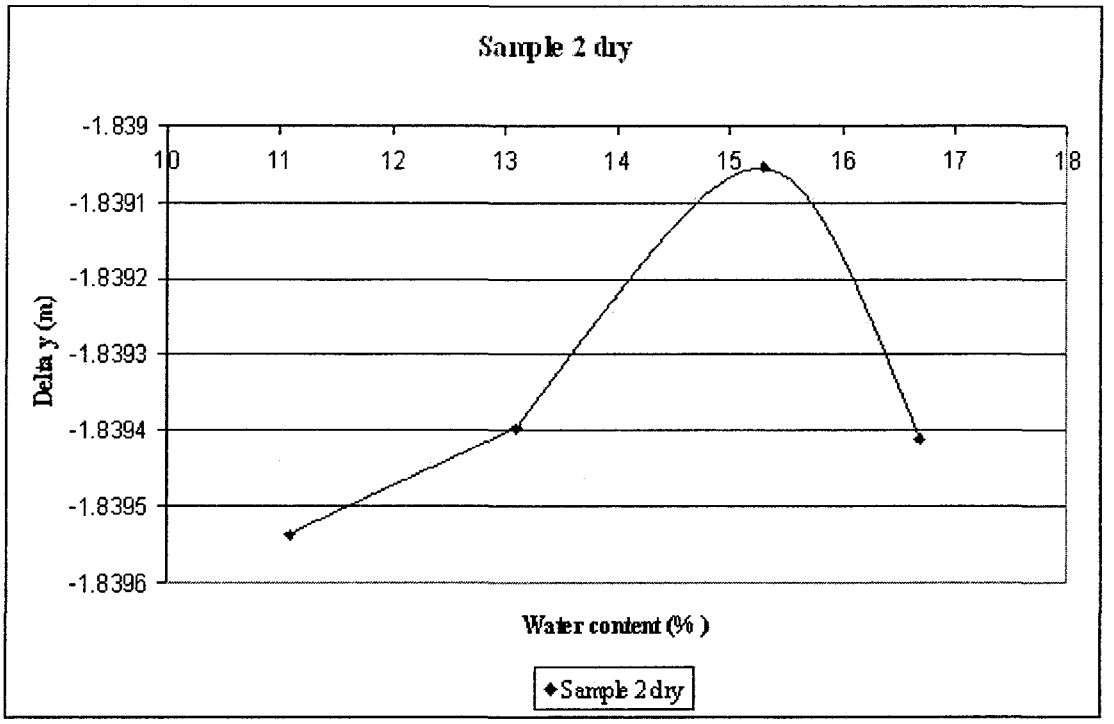

Figure 4.6: Validation curve for Sample 2

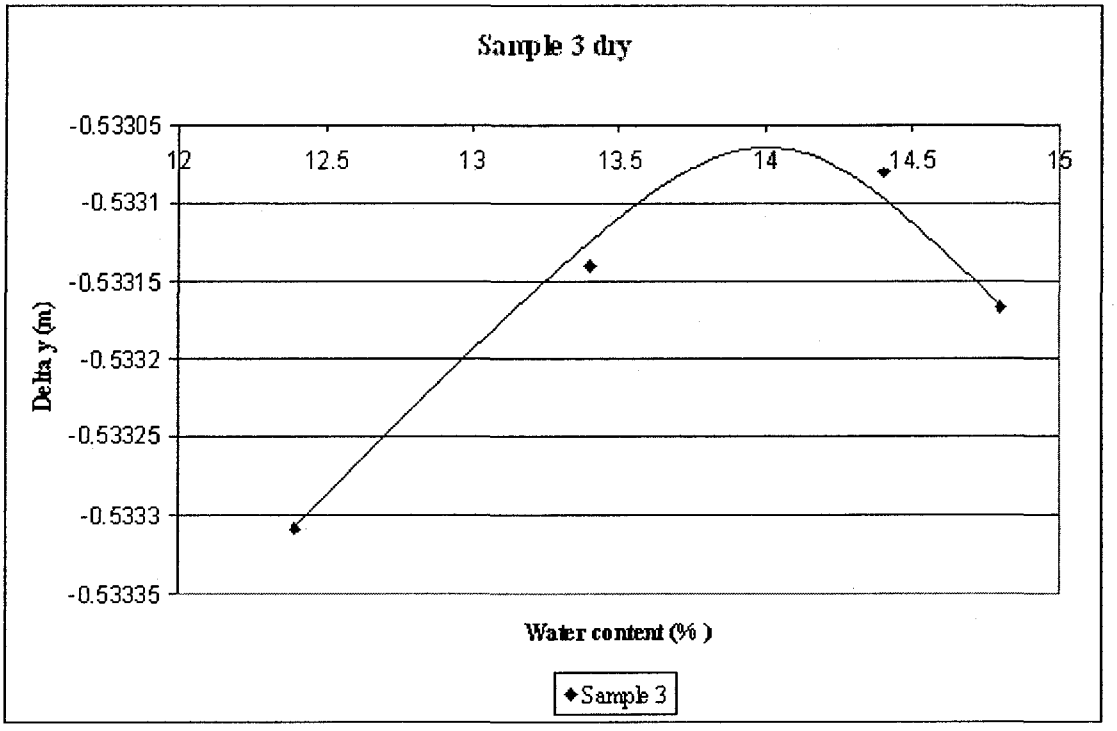

Figure 4.7: Validation curve for Sample 3

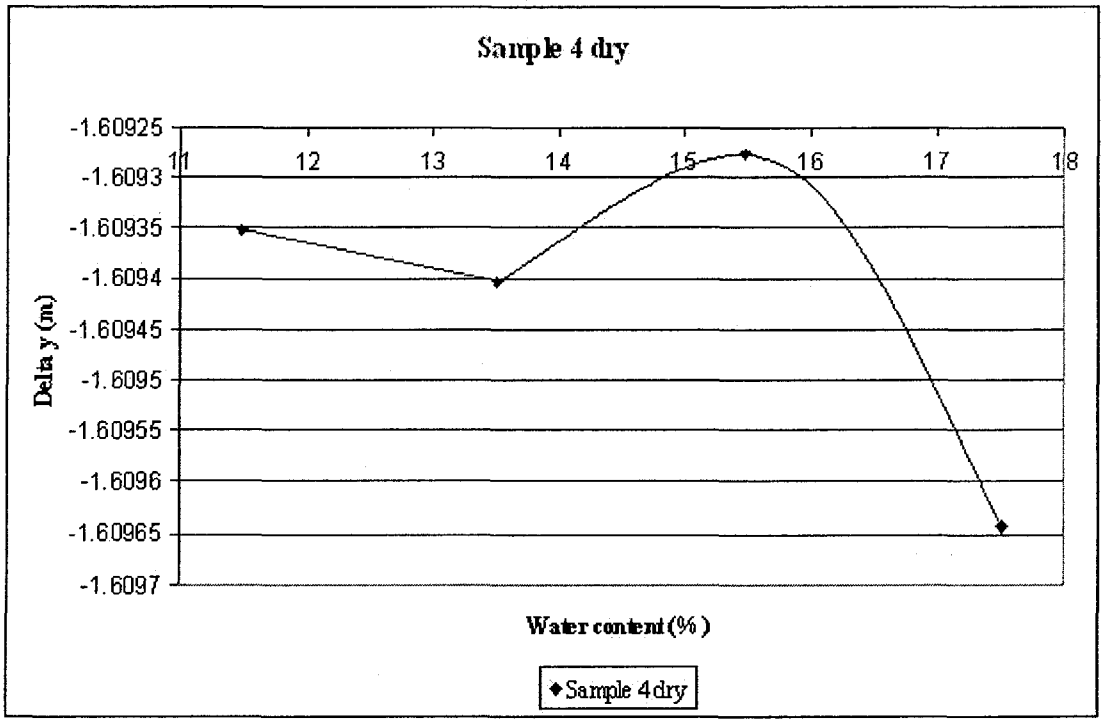

Figure 4.8: Validation curve for Sample 4

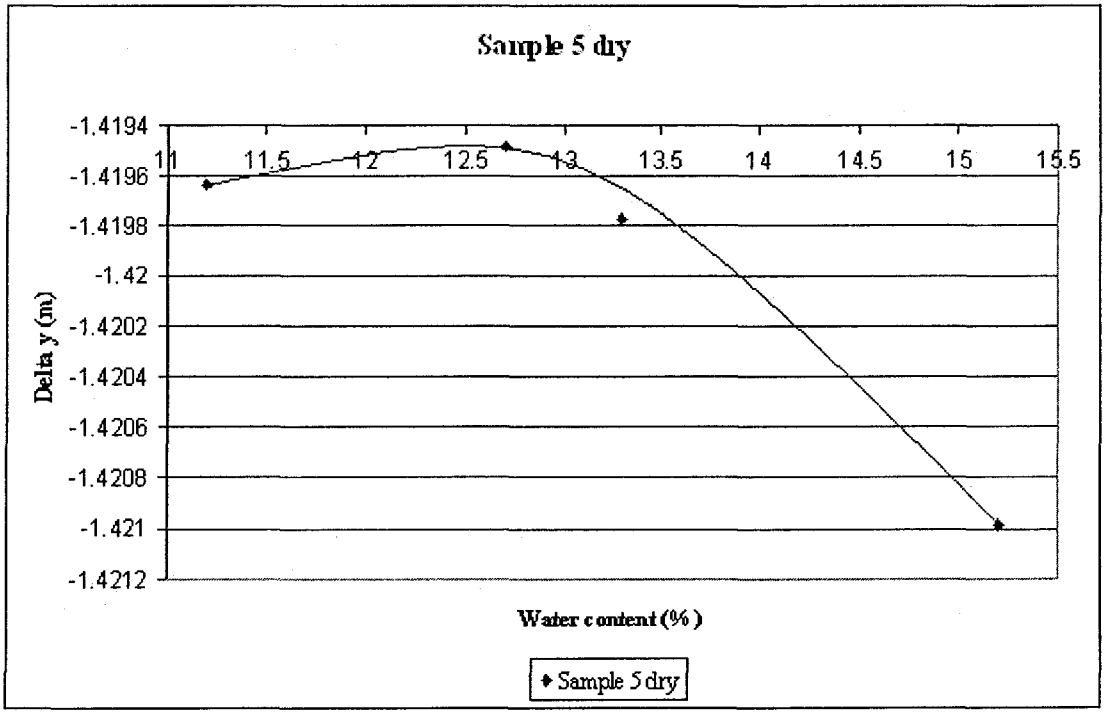

Figure 4.9: Validation curve for Sample 5

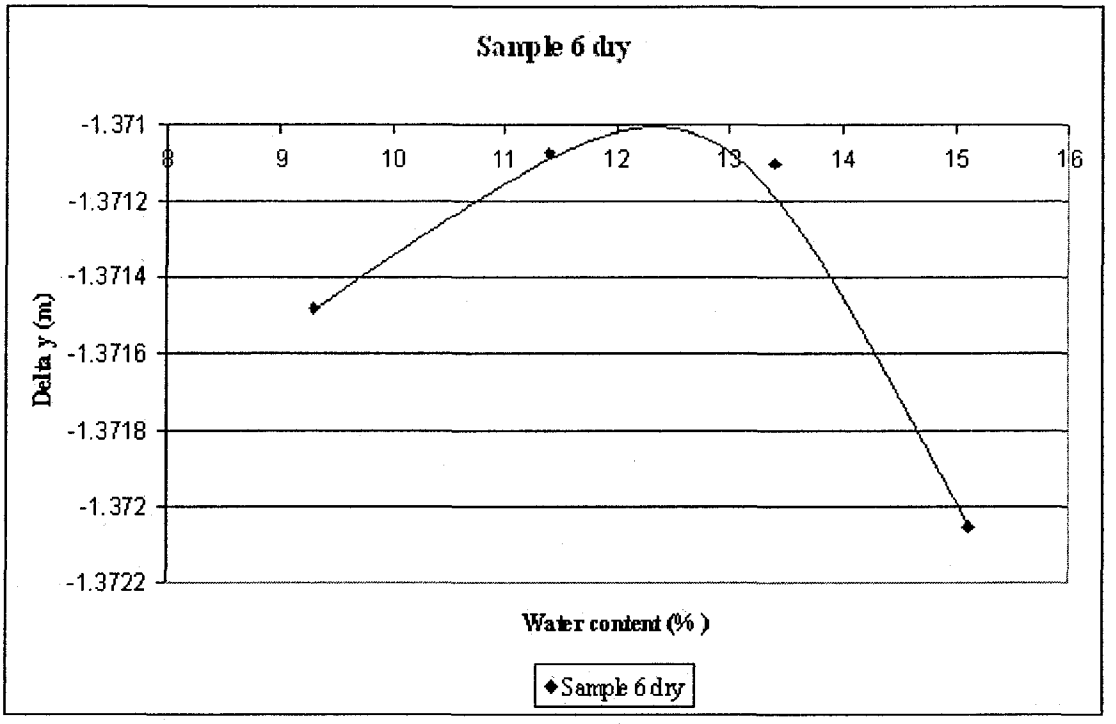

Figure 4.10: Validation curve for Sample 6

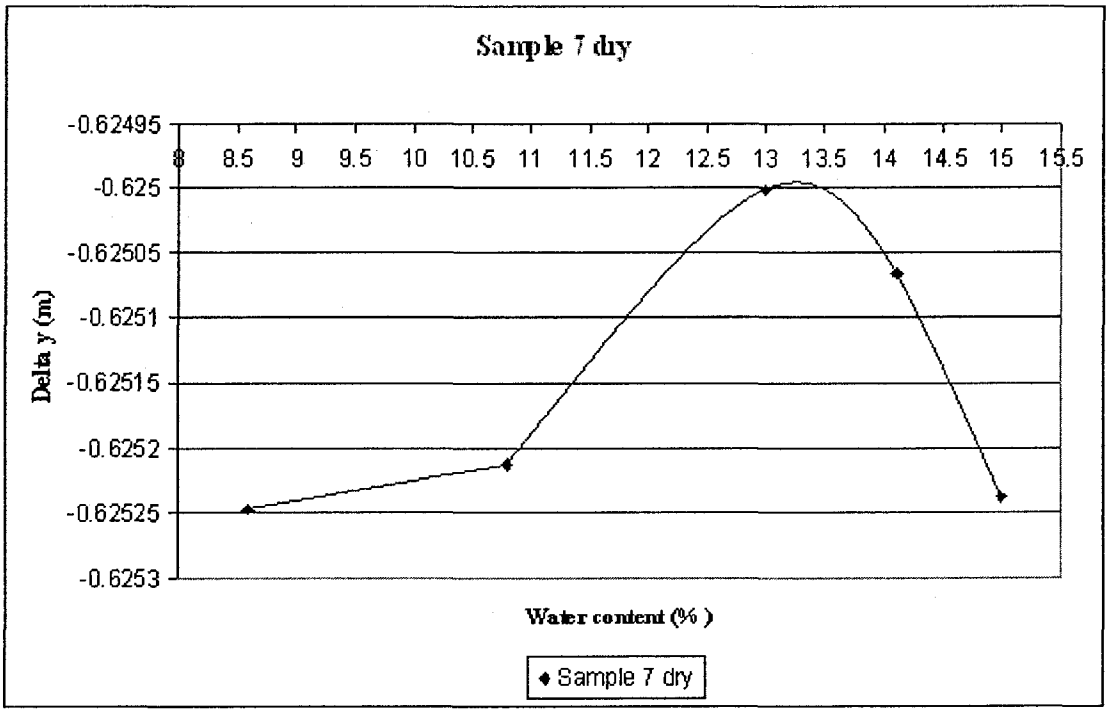

Figure 4.11: Validation curve for Sample 7

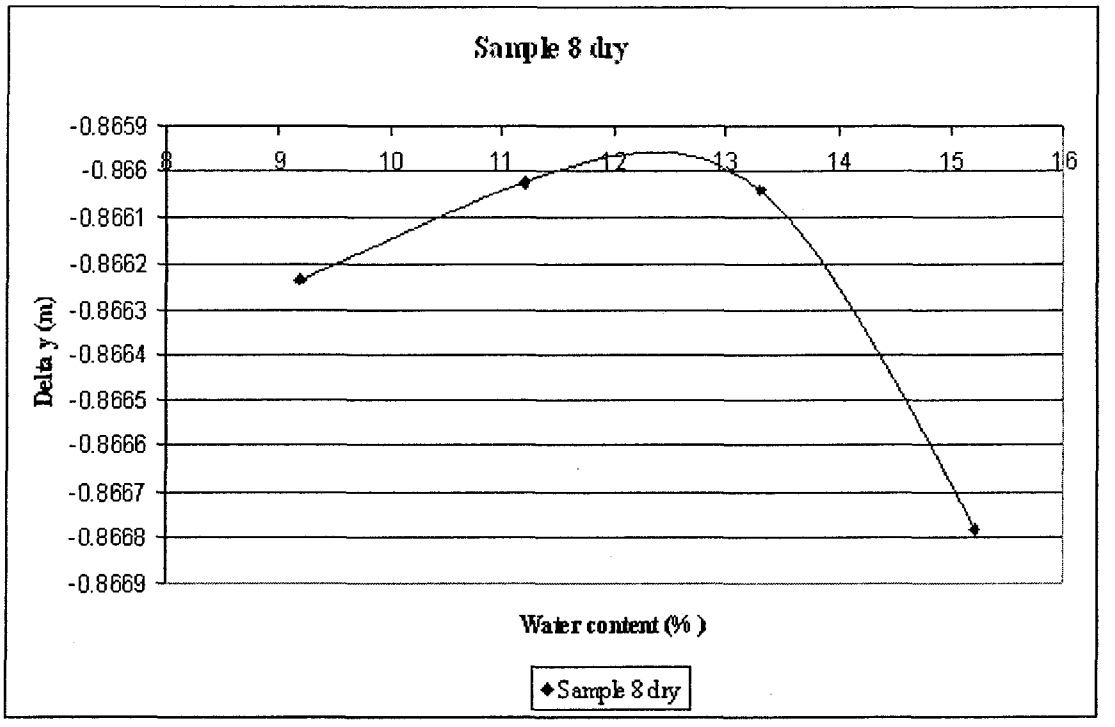

Figure 4.12: Validation curve for Sample 8

Table 4.2: Comparison of laboratory and numerical model OMC

Sample No.	Lab optimum water content (OWC)	Numerical model optimum water content (OWC)	% difference
1	13.0%	12.9%	0.8
2	15.3%	15.3%	0.0
3	14.0%	14.0%	0.0
4	15.5%	15.3%	1.3
5	13.7%	12.8%	6.6
6	12.2%	12.3%	3.9
7	13.5%	13.3%	1.5
8	12.5%	12.4%	0.8

The percentage difference between the numerical and experimental values obtained for the optimal moisture content range from 0 to 6.6%, accordingly, the numerical model

and test procedure were validated. The numerical model was used then to generate data for a wide range of parameters.

4.8 NUMERICAL MODEL RESULTS

Following the validation of the model, the value for the maximum dry unit weight was input into the Proctor model in order to allow for a comparison of the compaction with the differing boundary conditions. The following table summarizes the vertical deformation results yielded at the point of impact by the Proctor model for the maximum dry unit weight of each sample. The deformed mesh and the vertical deformations upon impact are depicted in figures 4.13 and 4.14 respectively.

Table 4.3: Vertical deformation for maximum unit weight using Proctor model

Sample number	Δy (m)
1	-1.839303
2	-1.839303
3	-0.398113
4	-1.60907
5	-1.418887
6	-1.267666
7	-0.624409
8	-0.812061

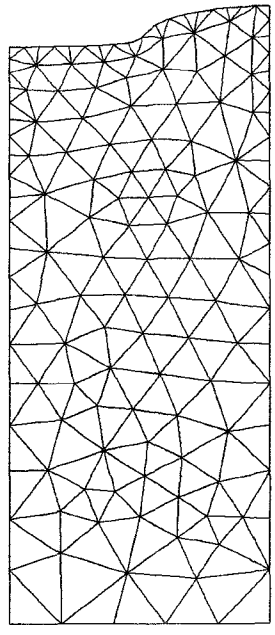

Figure 4.13: Deformed mesh upon impact

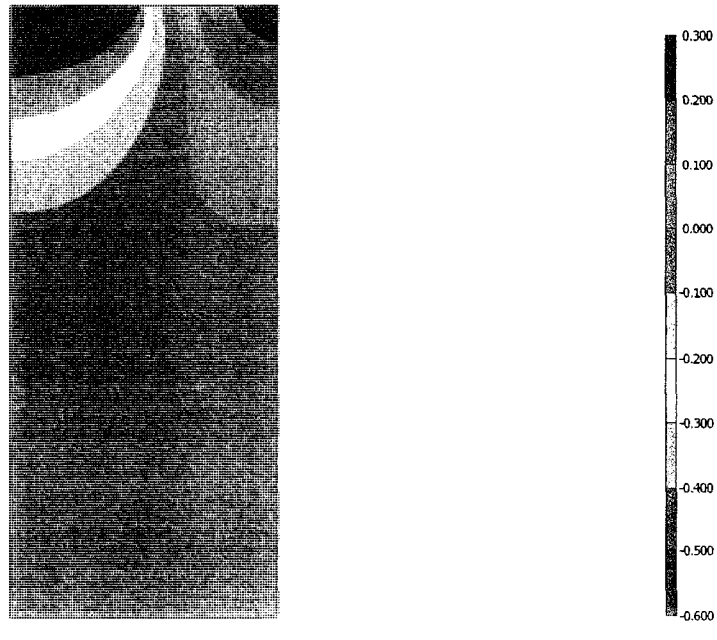

Figure 4.14: Shadings of vertical deformation upon impact for Proctor model

The lower boundary condition was then modified to simulate the case where the base of the Proctor mold is removed and replaced by a lower layer ranging from loose to dense material (Figure 4.15). An absorbent boundary was placed at the bottom of the model. The vertical deformations at both the point of impact and the interface of the two layers are presented in Table 4.5. Both the vertical deformations of the Proctor and the laterally confined model are presented for comparison purposes in Table 4.6.

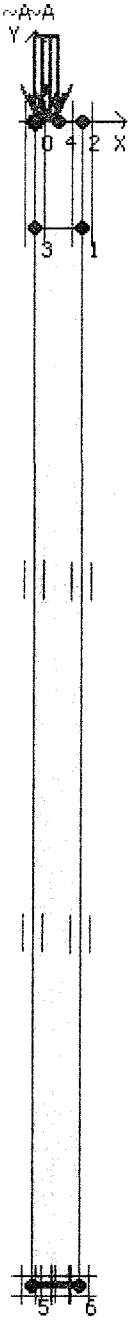

Figure 4.15: Laterally confined model geometry and boundary conditions

Figures 4.16 to 4.23 present the variation of the vertical deformation at the point of impact (upper layer) of each sample with increasing modulus of elasticity of the lower layer (E2) for the laterally confined model.

Table 4.5: Vertical deformations at points of impact and interface for laterally confined model

Sample number	E2 = 2500		E2 = 20 000		E2 = 65 000	
	Δy at point of impact (m)	Δy at interface (m)	Δy at point of impact (m)	Δy at interface (m)	Δy at point of impact (m)	Δy at interface (m)
1	-2.507963	-0.583273	-1.84243	-0.000108	-1.807088	-8.8E-05
2	-2.507963	-0.583273	-1.84243	-0.000108	-1.807088	-8.8E-05
3	-1.277831	-0.585521	-0.621481	0.000271	-0.549809	0.001552
4	-2.291773	-0.586028	-1.628389	-0.000667	-1.713243	-0.000132
5	-2.219078	-0.588315	-1.557188	-0.001024	-1.516346	-0.00014
6	-2.062174	-0.591365	-1.401224	-0.001461	-1.359219	-0.000152
7	-1.358078	-0.591411	-0.675918	0.001063	-0.634146	0.004717
8	-1.549067	-0.587215	-0.861968	-0.000141	-0.823861	0.003125

Table 4.6: Comparison of Proctor and laterally confined vertical deformations

Sample number	Proctor	Laterally confined					
		E2 = 2500		E2 = 20 000		E2 = 65 000	
	Δy at point of impact (m)	Δy at point of impact (m)	Δy at point of interface (m)	Δy at point of impact (m)	Δy at point of interface (m)	Δy at point of impact (m)	Δy at point of interface (m)
1	-1.839303	-2.507963	-0.583273	-1.84243	-0.000108	-1.807088	-8.8E-05
2	-1.839303	-2.507963	-0.583273	-1.84243	-0.000108	-1.807088	-8.8E-05
3	-0.532857	-1.277831	-0.585521	-0.621481	0.000271	-0.549809	0.001552
4	-1.60907	-2.291773	-0.586028	-1.628389	-0.000667	-1.713243	-0.000132
5	-1.418887	-2.219078	-0.588315	-1.557188	-0.001024	-1.516346	-0.00014
6	-1.267666	-2.062174	-0.591365	-1.401224	-0.001461	-1.359219	-0.000152
7	-0.624409	-1.358078	-0.591411	-0.675918	0.001063	-0.634146	0.004717
8	-0.812061	-1.549067	-0.587215	-0.861968	-0.000141	-0.823861	0.003125

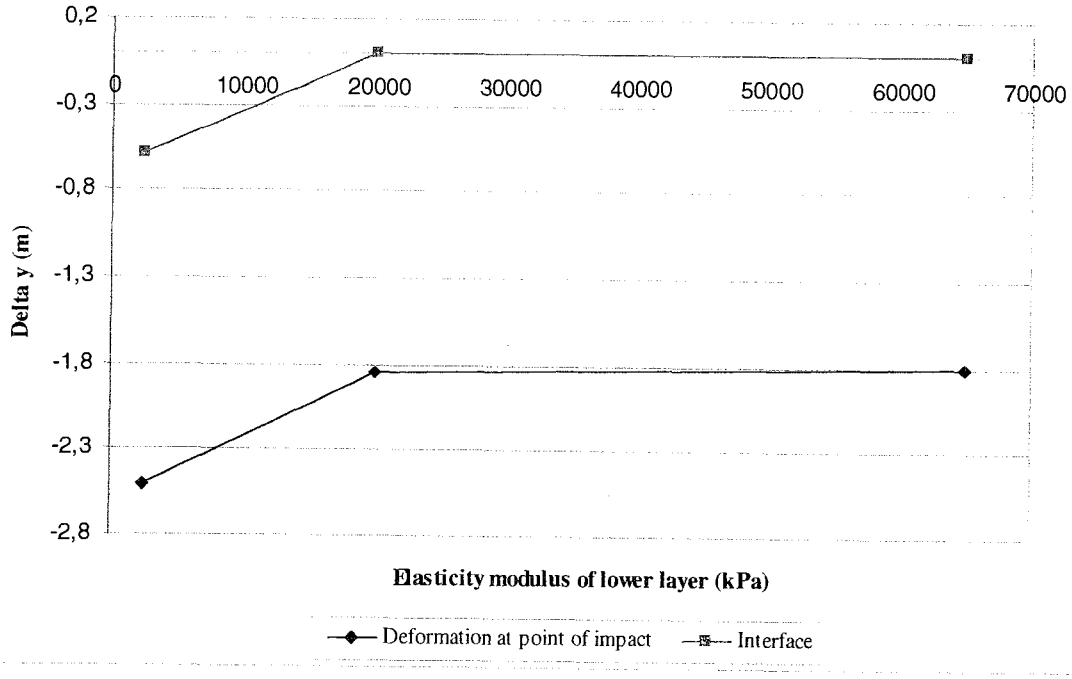

Figure 4.16: Vertical deformation of sample 1 at point of impact versus E2

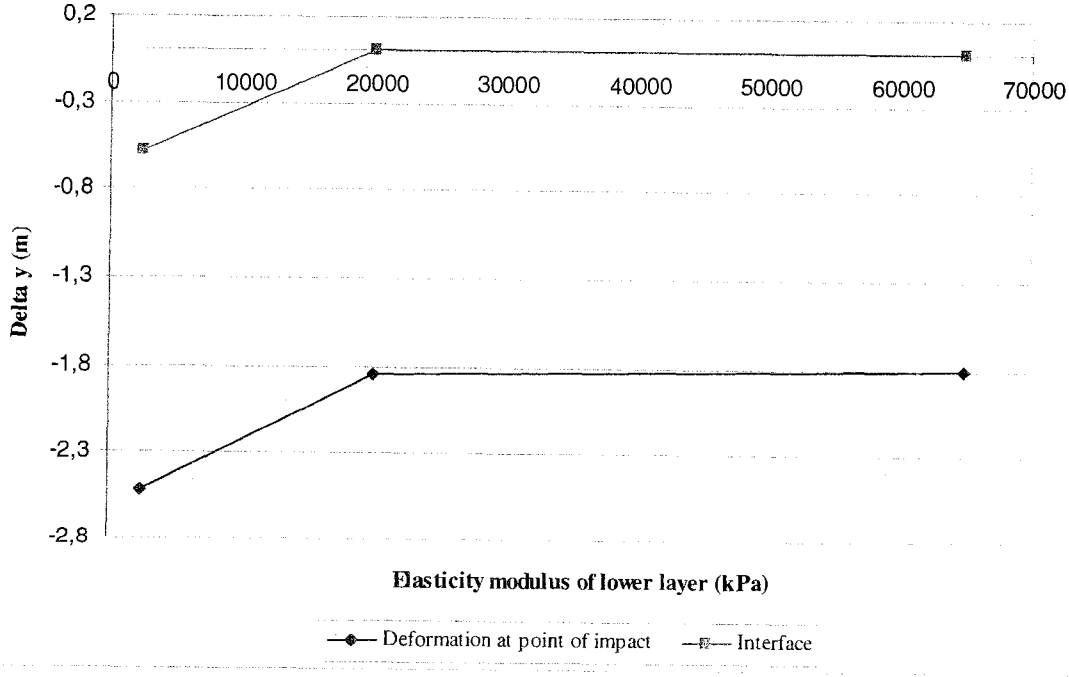

Figure 4.17: Vertical deformation of sample 2 at point of impact versus E2

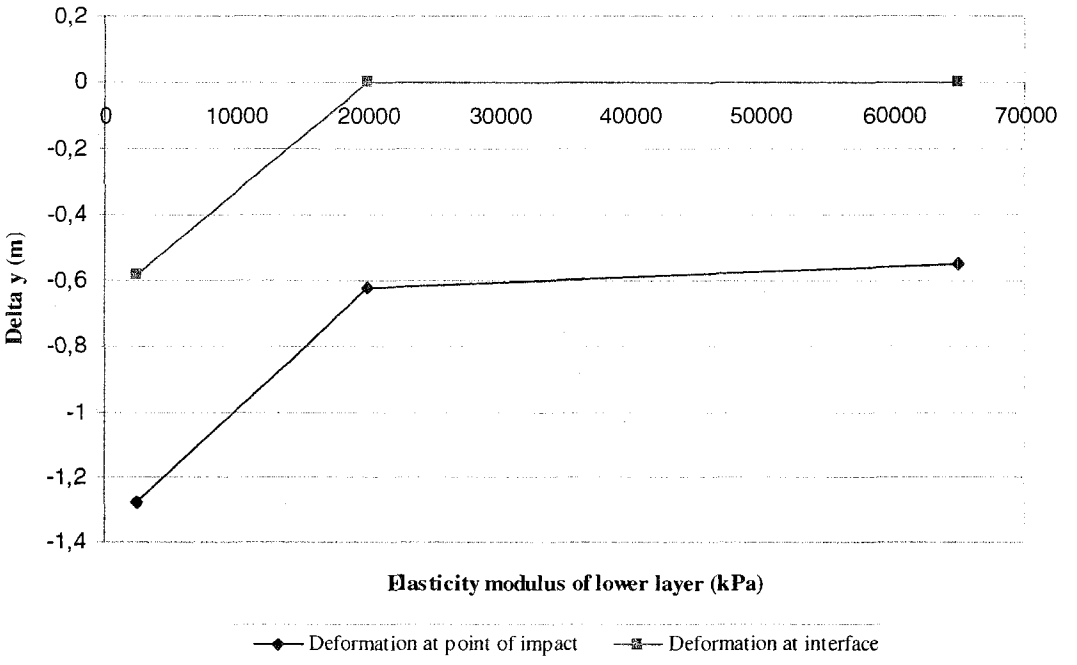

Figure 4.18: Vertical deformation of sample 3 at point of impact versus E2

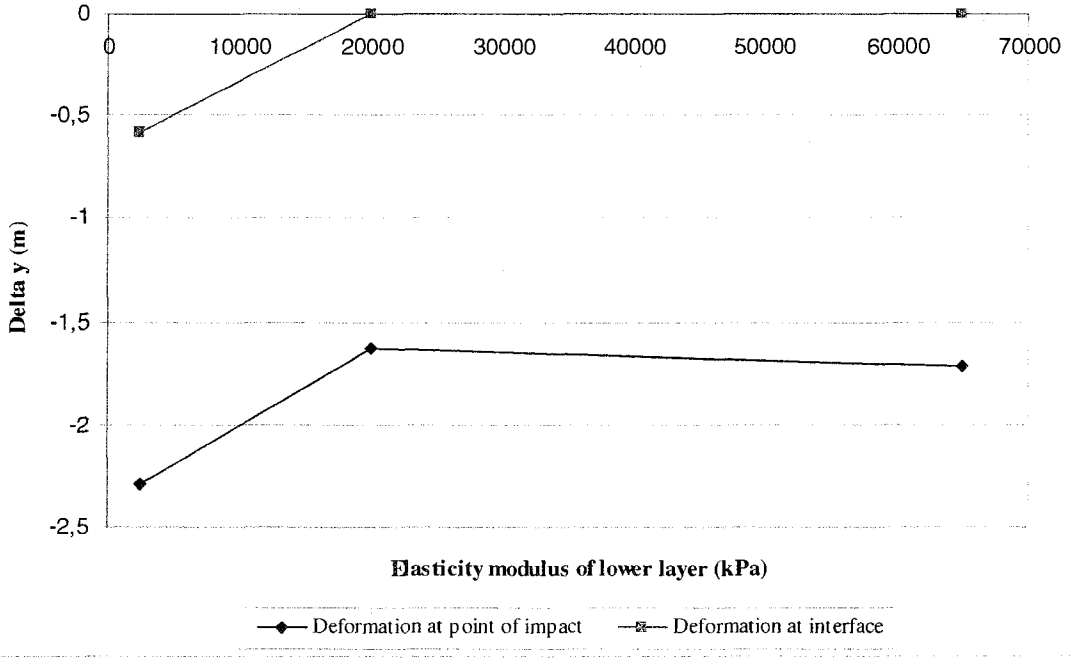

Figure 4.19: Vertical deformation of sample 4 at point of impact versus E2

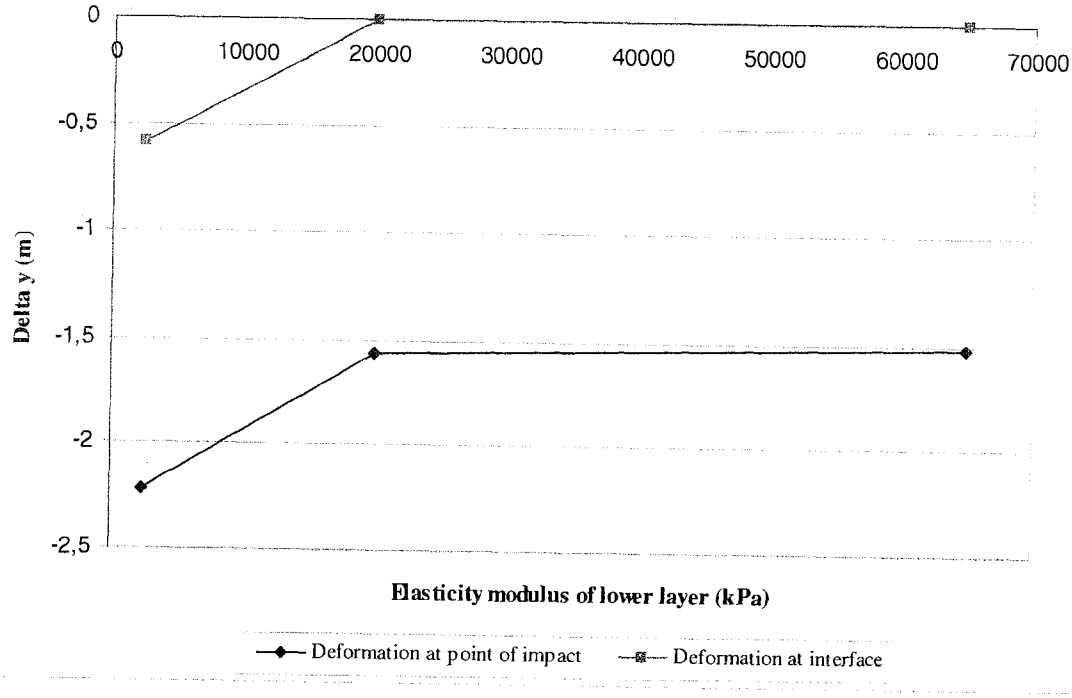

Figure 4.20: Vertical deformation of sample 5 at point of impact versus E2

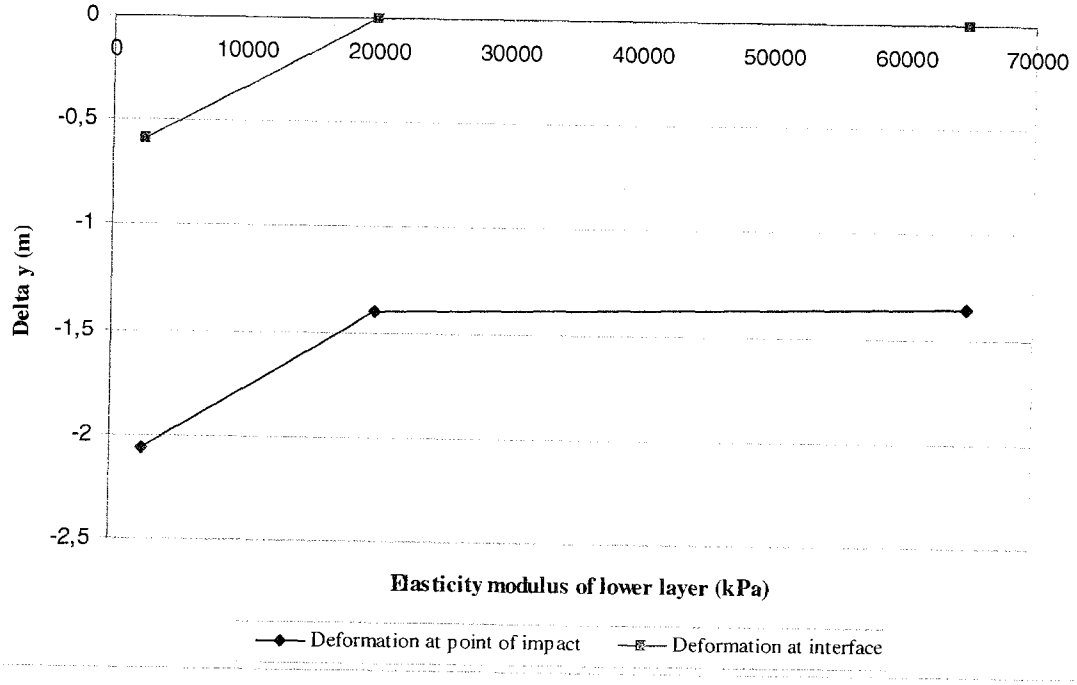

Figure 4.21: Vertical deformation of sample 6 at point of impact versus E2

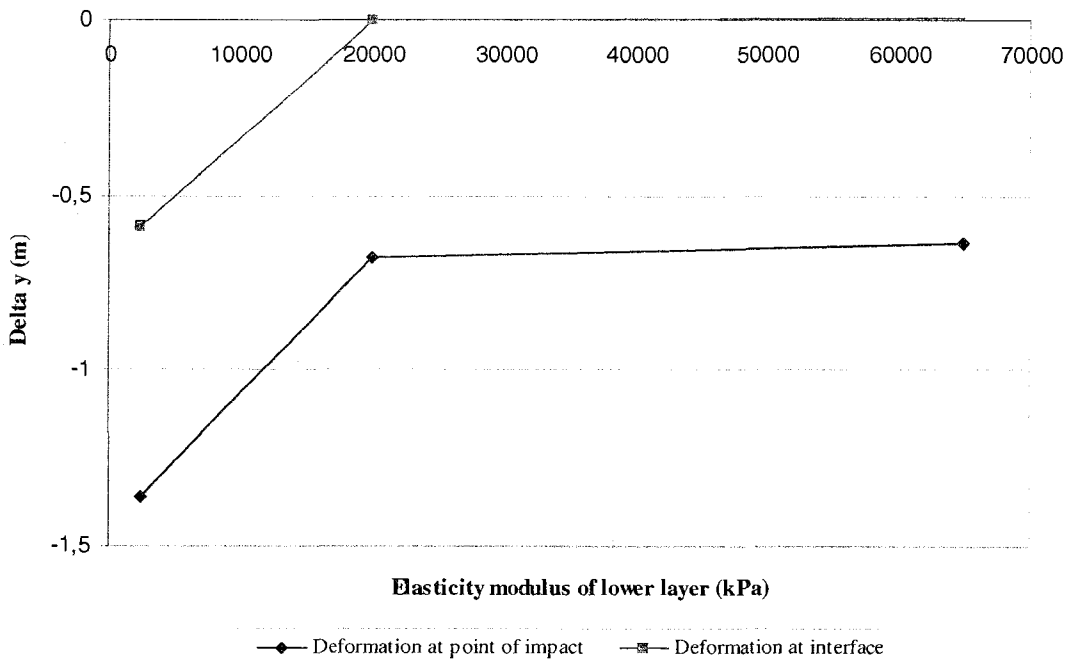

Figure 4.22: Vertical deformation of sample 7 at point of impact versus E2

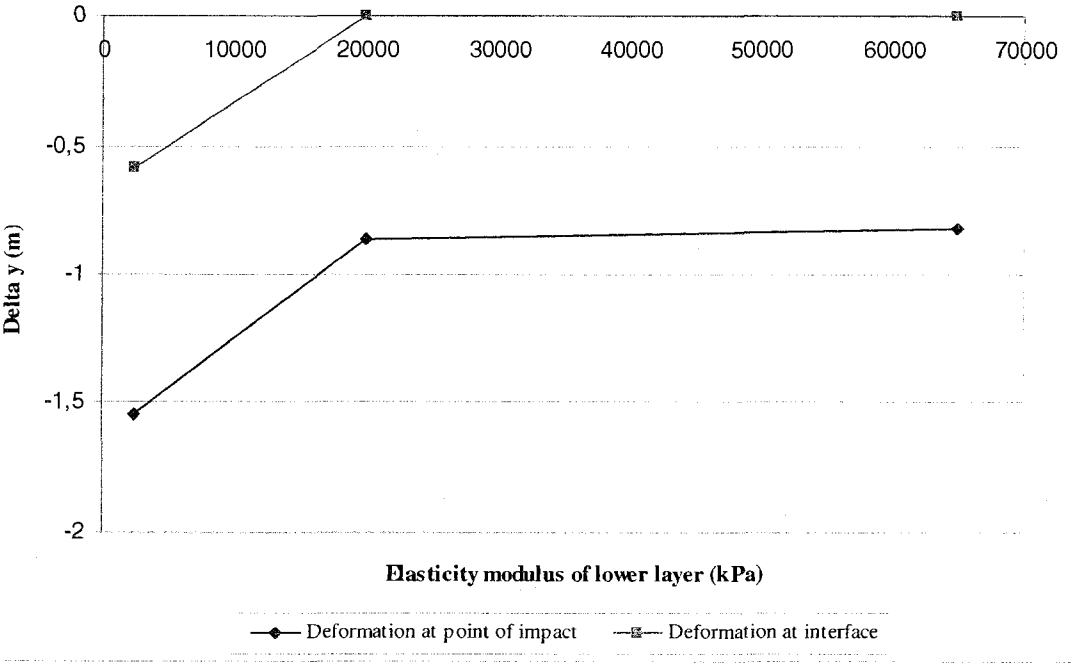

Figure 4.23: Vertical deformation of sample 8 at point of impact versus E2

Finally, the field case was simulated using the maximum dry unit weight of each sample for an upper layer 2.3 m thick and a lower layer ranging from loose to dense. Absorbent boundaries were placed at the bottom and the outer lateral side of the model (Figure 4.24). The following table (Table 4.7) presents the vertical deformations obtained for each sample (upper layer) at the point of impact and at the interface between the 2 layers for the 3 lower layer cases (ranging from loose to dense).

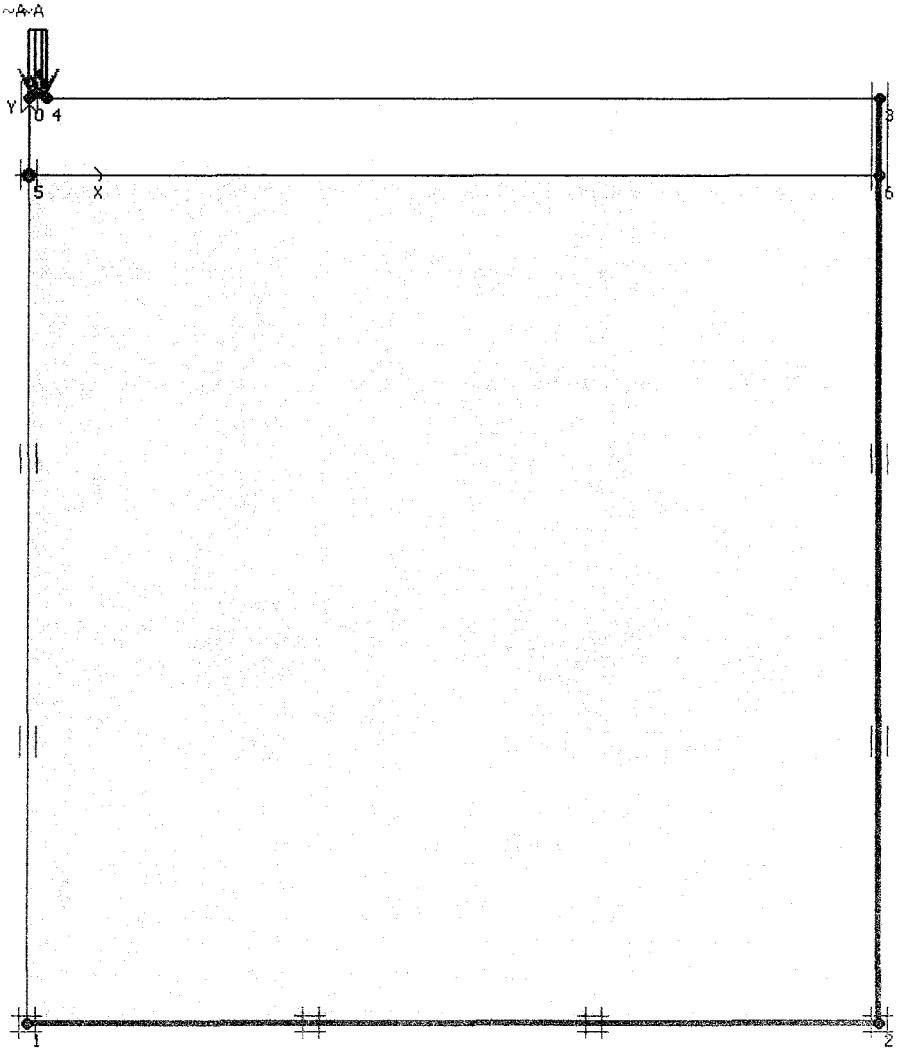

Figure 4.24: Field model geometry and boundary conditions

Table 4.7: Vertical deformations at point of impact and interface for field model

Sample number	E2 = 2500		E2 = 20 000		E2 = 65 000	
	Δy at point of impact (m)	Δy at interface (m)	Δy at point of impact (m)	Δy at interface (m)	Δy at point of impact (m)	Δy at interface (m)
1	-5.777391	-0.348258	-4.956469	-0.076823	-4.428351	-0.007078
2	-5.777391	-0.348258	-4.956469	-0.076823	-4.428351	-0.007078
3	-2.494264	-0.242667	-2.447296	0.021986	-1.85911	0.004351
4	-5.232149	-0.348167	-4.891018	0.023796	-4.57413	0.004579
5	-4.755572	-0.345979	-4.650064	0.023052	-4.074041	0.004398
6	-4.365637	-0.34377	-3.980245	0.022432	-3.666135	0.004231
7	-2.856685	-0.30776	-2.55315	0.020773	-2.021212	0.003864
8	-3.418835	-0.307342	-3.165017	0.021639	-2.604735	0.004109

Figures 4.25 to 4.32 present the variation of the vertical deformation at the point of impact (upper layer) of each sample with increasing modulus of elasticity of the lower layer for the field case.

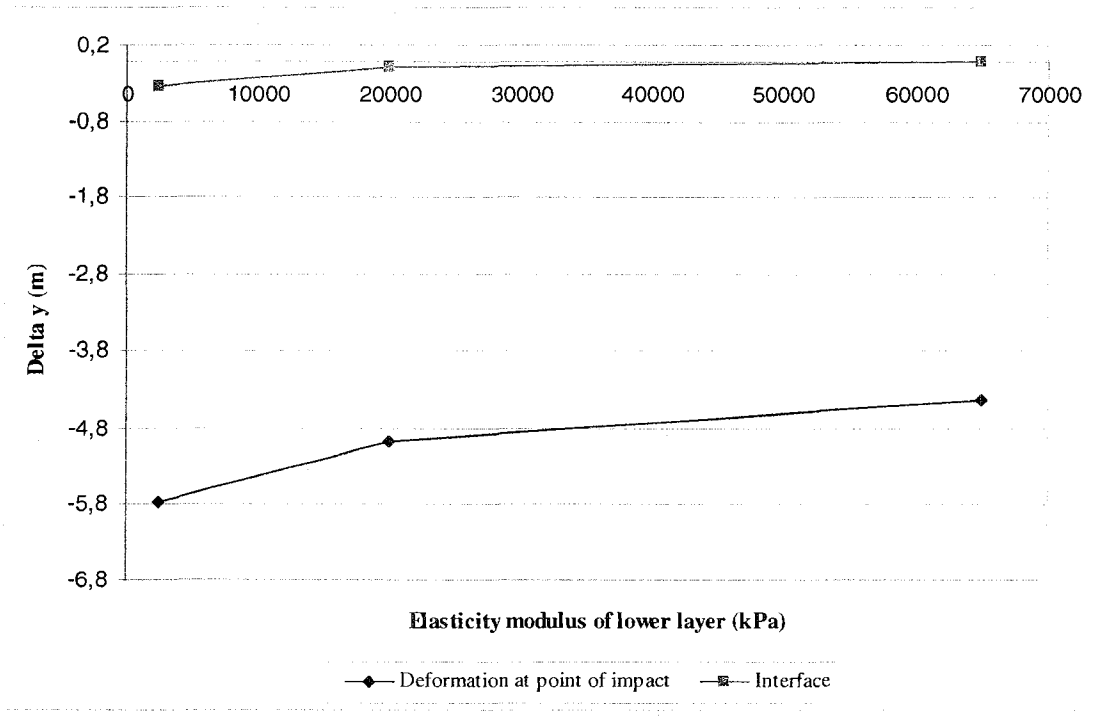

Figure 4.25: Vertical deformation of sample 1 at point of impact versus E2 (field)

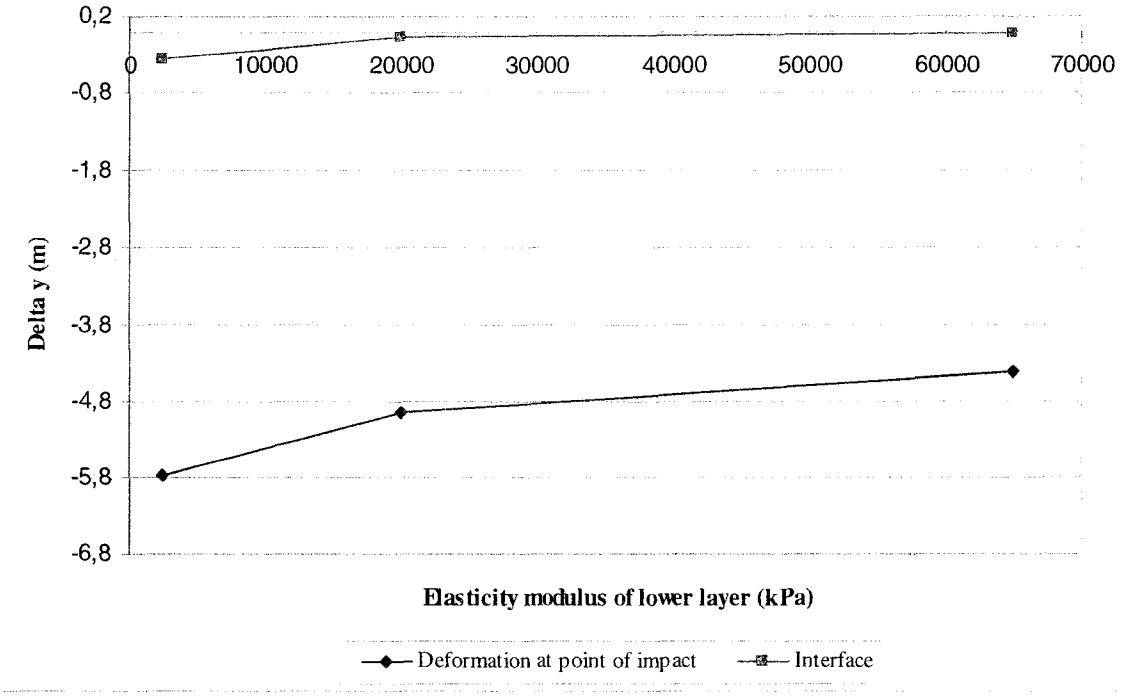

Figure 4.26: Vertical deformation of sample 2 at point of impact versus E2 (field)

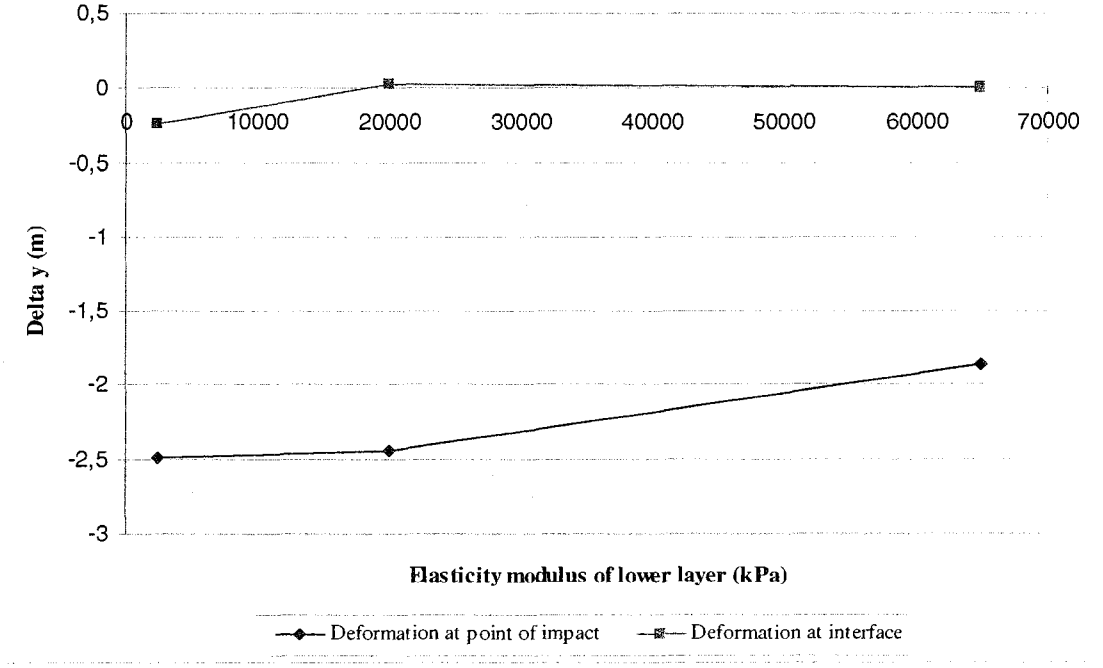

Figure 4.27: Vertical deformation of sample 3 at point of impact versus E2 (field)

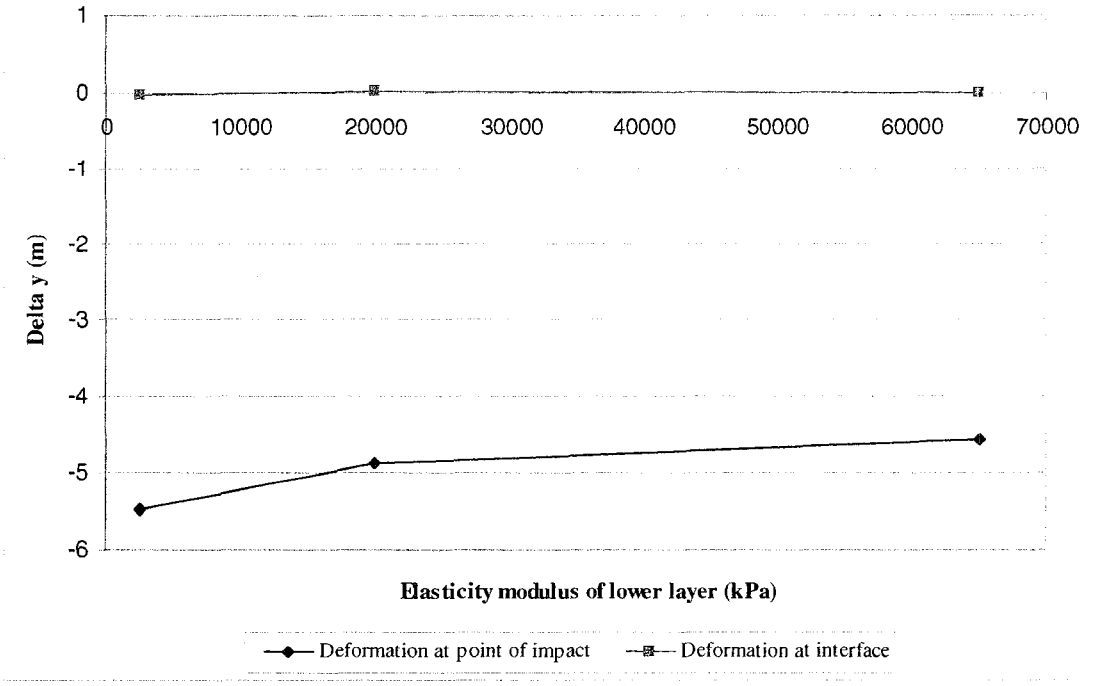

Figure 4.28: Vertical deformation of sample 4 at point of impact versus E2 (field)

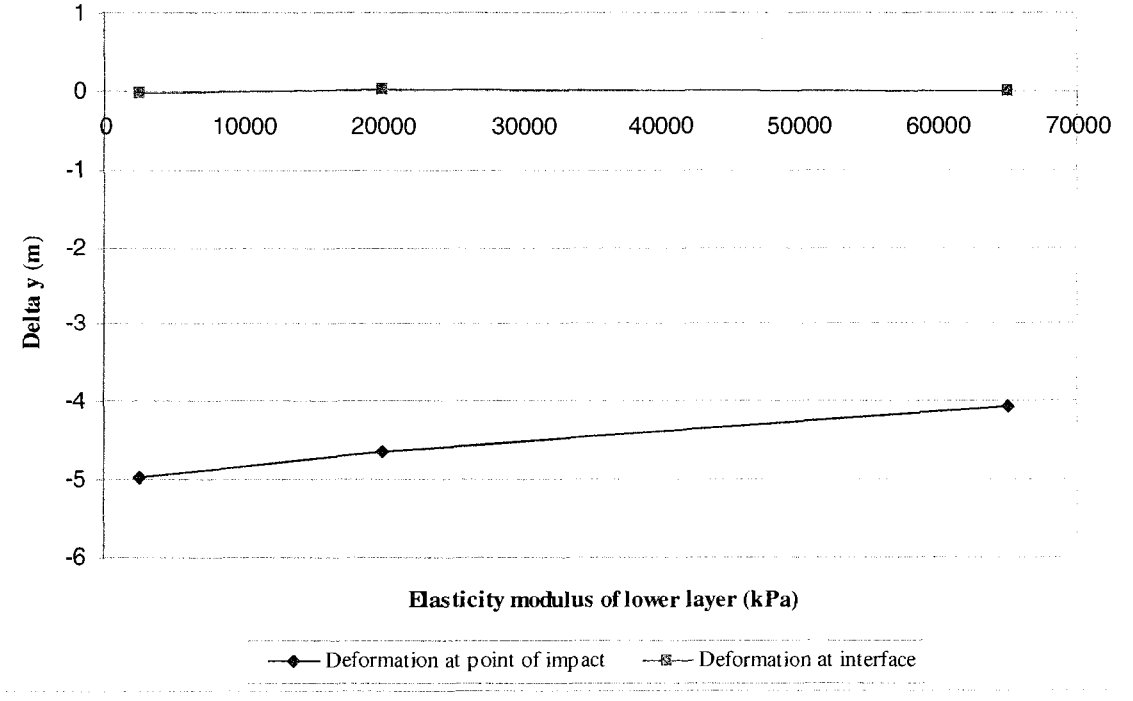

Figure 4.29: Vertical deformation of sample 5 at point of impact versus E2 (field)

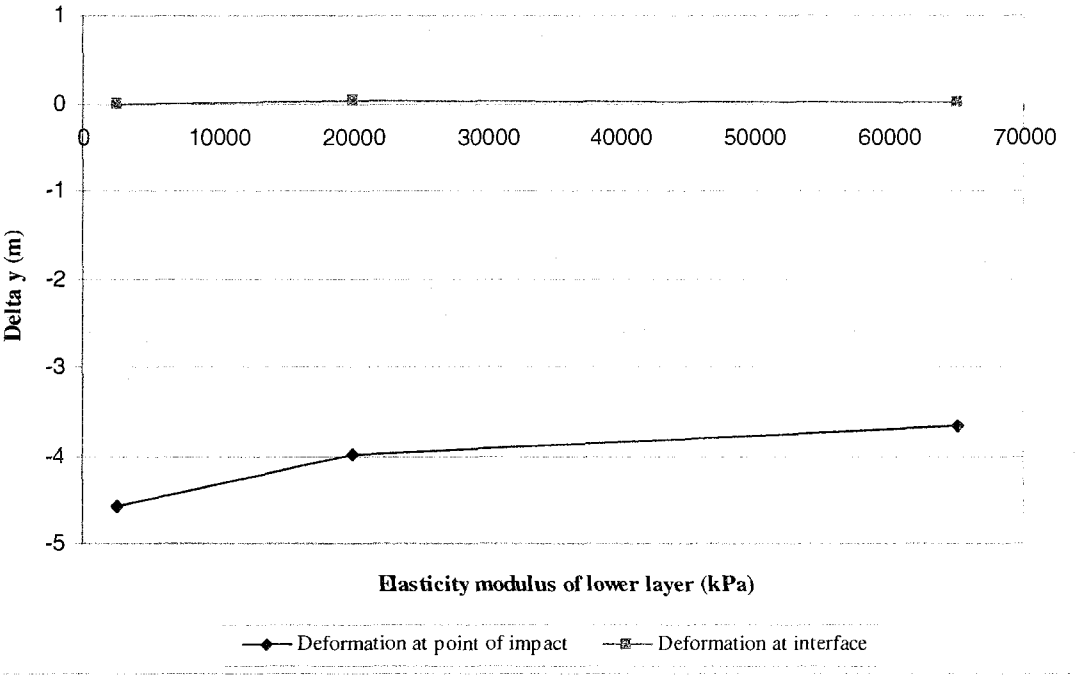

Figure 4.30: Vertical deformation of sample 6 at point of impact versus E2 (field)

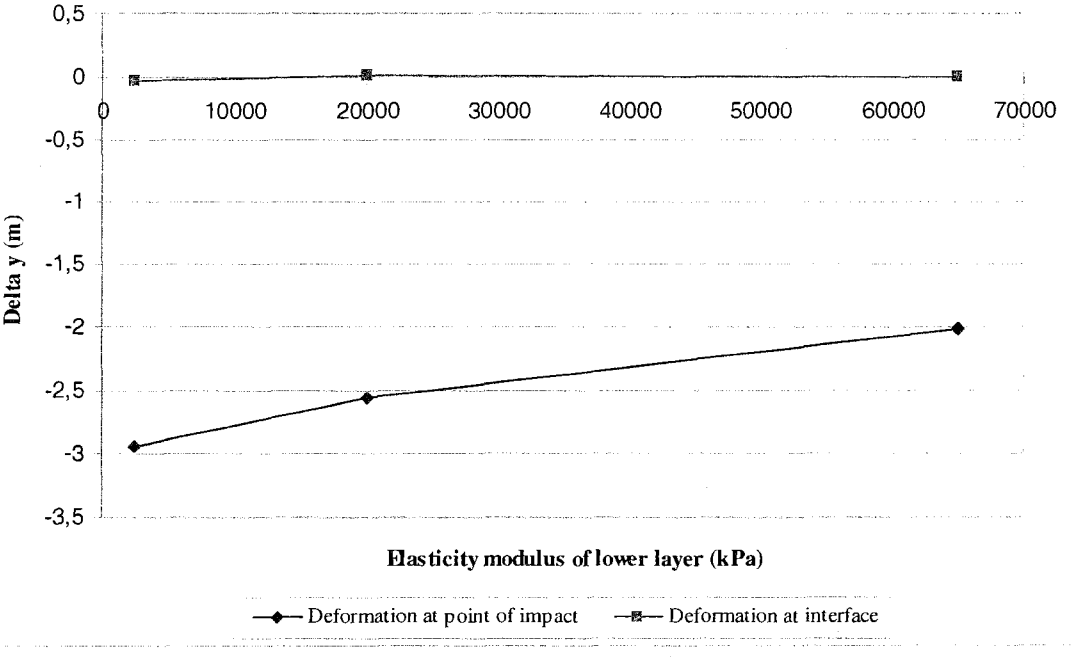

Figure 4.31: Vertical deformation of sample 7 at point of impact versus E2 (field)

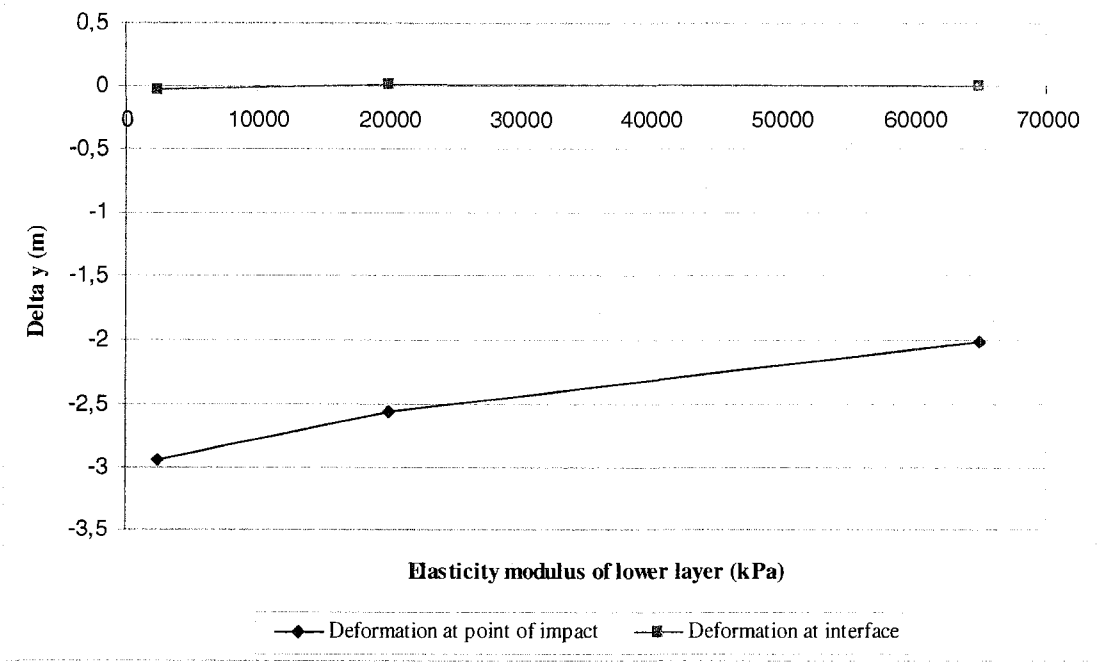

Figure 4.32: Vertical deformation of sample 8 at point of impact versus E2 (field)

4.9 DATA ANALYSIS

From figures 4.16 to 4.23, for the laterally confined case, it can be seen that as the vertical deformation at the interface approaches 0 m, the upper layer is actually being compacted beyond the initial measured Proctor deformation. This is observed for all samples with values of 20 000 and 65 000 kPa for the underlying layer's modulus of elasticity. A similar trend can be observed in figures 4.26 to 4.32 for the field case. In both cases, this is due to the applied energy waves coming into contact with a stronger underlying layer, of which some are absorbed and others are reflected back into the upper layer, further compaction of the upper layer. However, when the underlying layer is weaker than the subgrade layer (i.e. E2=2 500 kPa), the lower layer absorbs the energy waves reaching it; the overlying layer is then less compacted.

It was also noted that both the graphs of the vertical deformation at the point of impact versus the elasticity modulus of the lower layer for the laterally confined model and the field model demonstrate the same trend; the upper layer moves down according to the lower layer's deformation. However, in order to determine whether or not the underlying layer has had any effect with respect to the compaction of the upper layer, it is necessary to determine the actual deformation exhibited by the upper layer. That is, the vertical deformation of the upper layer without accounting for the movement of the lower layer. Therefore, the vertical deformation of the interface was subtracted from that of the point of impact for comparison purposes. The results for the laterally confined model and the field model are respectively presented in the following tables:

Table 4.4: Actual vertical deformation at point of impact for the laterally confined model

Sample number	Actual vertical deformation at point of impact (m)		
	E2 = 2500 kPa	E2 = 20 000 kPa	E2 = 65 000
1	-1.92469	-1.842322	-1.807
2	-1.92469	-1.842322	-1.807
3	-0.69231	-0.62121	-0.551361
4	-1.705745	-1.627722	-1.713111
5	-1.630763	-1.556164	-1.516206
6	-1.470809	-1.399763	-1.359067
7	-0.766667	-0.676981	-0.638863
8	-0.961852	-0.861827	-0.826986

Table 4.5: Actual vertical deformation at point of impact for the field model

Sample number	Actual vertical deformation at point of impact (m)		
	E2 = 2500 kPa	E2 = 20 000 kPa	E2 = 65 000
1	-5.42913	-4.87965	-4.42127
2	-5.42913	-4.87965	-4.42127
3	-2.2516	-2.46928	-1.86346
4	-4.88398	-4.91481	-4.57871
5	-4.40959	-4.67312	-4.07844
6	-4.02187	-4.00268	-3.67037
7	-2.54893	-2.57392	-2.02508
8	-3.11149	-3.18666	-2.60884

In order to demonstrate the above statements numerically, the percentage difference between the Proctor deformation and the actual vertical deformation of the laterally confined model at the point of impact were calculated, as was that between the Proctor model and the actual vertical deformation of the field model. A positive percentage greater than zero indicates that applied energy was lost to the underlying layer, whereas a negative one indicates that some of the energy was reflected back into the upper layer, further compacting it. If there is no difference (0%), this means that the upper layer was compacted exactly as in the Proctor model. Tables 4.11 and 4.12 present the results obtained.

Table 4.6: Percentage difference of actual vertical deformations between the Proctor model and the laterally confined model

Sample number	% difference between Proctor and laterally confined model vertical deformation results		
	E2 = 2500 kPa	E2 = 20 000 kPa	E2 = 65 000
1	4.6	0.2	-1.8
2	4.6	0.2	-1.8
3	29.9	16.6	3.5
4	6.0	1.2	6.5
5	14.9	9.7	6.9
6	16.0	10.4	7.2
7	22.8	8.4	2.3
8	18.4	6.1	1.8

The % differences obtained in Table 4.13 indicate that as the modulus of elasticity of the lower layer increases, so does the compaction of the upper layer. It is even seen for sample 1 and 2 that when the lower layer has an elasticity modulus of 65 000 kPa, the upper layer is compacted beyond the Proctor deformation.

Table 4.7: Percentage difference of actual vertical deformations between the Proctor model and the field model

Sample number	% difference between Proctor and laterally confined model vertical deformation results		
	E2 = 2500 kPa	E2 = 20 000 kPa	E2 = 65 000
1	195.2	165.3	140.4
2	195.2	165.3	140.4
3	322.6	363.4	249.7
4	203.5	205.4	184.6
5	210.8	229.4	187.4
6	217.3	215.8	189.5
7	308.2	312.2	224.3
8	283.2	292.4	221.3

The results of Table 4.12 follow the same trend of the results presented in Table 4.11; i.e. increasing the level of compaction of the upper layer with increasing the elasticity modulus of the lower layer. Furthermore, they also demonstrated that the boundaries of the Proctor apparatus are not duplicating the field condition, as the % difference ranges from 140.4 to 363.4%.

Therefore, a trend of increasing compaction of the upper layer with increasing elasticity modulus of the lower layer was observed and it was found that the Proctor boundaries are not valid for dynamic field compaction.

4.10 RESULTS FOR A WEAK SUBGRADE LAYER OVERLYING A DEEP DEPOSIT

As the results obtained for the equivalent Proctor depth of 2.3 m demonstrated that the underlying layer does indeed affect the compaction of the upper layer, it was desired to further investigate the role of the underlying layer in the field. This was achieved by modifying the basic geometry of the field model to that of a thin subgrade layer overlying a deep deposit. Both layers are assumed to be sand for a range of stiffness values. The deep deposit has dimensions of 25 m in depth and width, whereas the subgrade layer ranges from 1 m to 3 m thick.

This field case was simulated using the maximum dry unit weight of each sample for the upper layer of 1, 2 and 3 m thick and a lower layer ranging from loose to dense (bottom layers 1 through 3). Absorbent boundaries were placed at the bottom and the outer lateral side of the model. The following tables (Table 4.13 through Table 4.15) present the vertical deformations obtained for each sample (upper layer) at the point of impact and at the interface between the 2 layers for the 3 lower layer cases (ranging from loose to dense). The results for the field model are also presented graphically in the following figures (figures 4.33 to 4.80). Figures 4.33 to 4.56 present the variation of the vertical deformation (Δy) of each sample with increasing thickness of the upper layer (H), whereas figures 4.57 through 4.80 show the variation of the vertical deformation for a given upper layer depth of each sample with increasing modulus of elasticity of the lower layer.

Table 4.8: Vertical deformations at point of impact and interface for field model with upper layer thickness of 1 m

Sample number	E2 = 2500		E2 = 20 000		E2 = 65 000	
	Δy at point of impact (m)	Δy at interface (m)	Δy at point of impact (m)	Δy at point of impact (m)	Δy at interface (m)	Δy at point of impact (m)
1	-9.328349	-3.824488	-5.661009	-1.870517	-3.861289	-0.127409
2	-9.328349	-3.824488	-5.661009	-1.870517	-3.861289	-0.127409
3	-5.301016	-2.250320	-2.579551	-0.900329	-1.440656	-0.290476
4	-8.708214	-3.601555	-5.221622	-1.770294	-3.464246	-0.137503
5	-8.159257	-3.392716	-4.294620	-1.598476	-2.986579	-0.214346
6	-7.711135	-3.229843	-4.553321	-1.594627	-2.706868	-0.198746
7	-5.979867	-2.473239	-3.393269	-1.135299	-1.782155	-0.274337
8	-6.534652	-2.685744	-3.773587	-1.252801	-2.146574	-0.297844

Table 4.9: Vertical deformations at point of impact and interface for field model with upper layer thickness of 2 m

Sample number	E2 = 2500		E2 = 20 000		E2 = 65 000	
	Δy at point of impact (m)	Δy at interface (m)	Δy at point of impact (m)	Δy at point of impact (m)	Δy at interface (m)	Δy at point of impact (m)
1	-6.384738	-0.520849	-5.847355	-0.154117	-5.221197	-0.018680
2	-6.384738	-0.520849	-5.847355	-0.154117	-5.221197	-0.018680
3	-2.755118	-0.332661	-2.109621	-0.071492	-1.732195	-0.010228
4	-5.807496	-0.506015	-5.262843	-0.143465	-4.327860	-0.025587
5	-5.331962	-0.484829	-3.969935	-0.106982	-3.865745	-0.026592
6	-5.159219	-0.419730	-4.395180	-0.080636	-3.490202	-0.027393
7	-3.336141	-0.376402	-2.378665	-0.061515	-1.885459	-0.010906
8	-3.717406	-0.420931	-3.264298	-0.104483	-2.660539	-0.028577

Table 4.10: Vertical deformations at point of impact and interface for field model with upper layer thickness of 3 m

Sample number	E2 = 2500		E2 = 20 000		E2 = 65 000	
	Δy at point of impact (m)	Δy at interface (m)	Δy at point of impact (m)	Δy at point of impact (m)	Δy at interface (m)	Δy at point of impact (m)
1	-6.312203	-0.129822	-6.285769	-0.043208	-5.796537	-0.023258
2	-6.312203	-0.129822	-6.285769	-0.043208	-5.796537	-0.023258
3	-2.559191	-0.165702	-2.126017	-0.022297	-1.891513	-0.002906
4	-5.706577	-0.157849	-5.616040	-0.044164	-4.808536	-0.023630
5	-5.203171	-0.017488	-5.030003	-0.044907	-4.303736	-0.023916
6	-4.452054	-0.175267	-4.283555	-0.045769	-3.892483	-0.020000
7	-3.002163	-0.255711	-2.369676	-0.022446	-2.135342	-0.003327
8	-3.548715	-0.174614	-3.316949	-0.046981	-2.941655	-0.024676

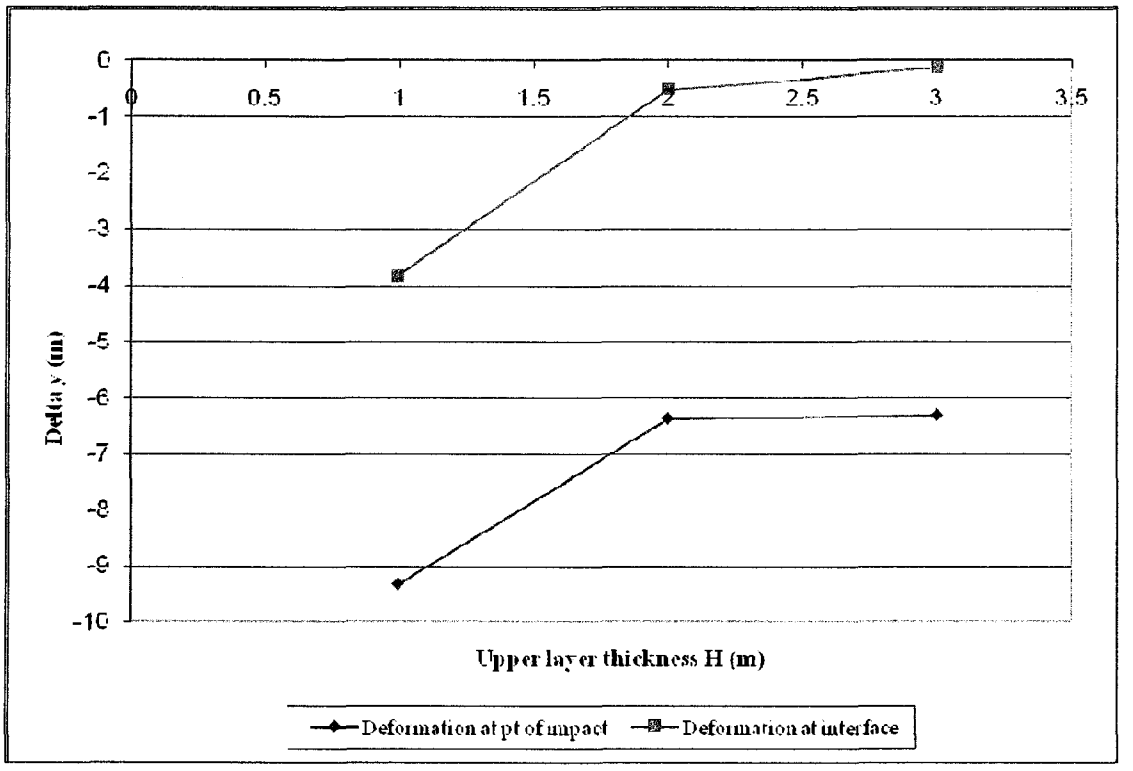

Figure 4.33: Vertical deformation versus depth for sample 1 with E2=2500 kPa

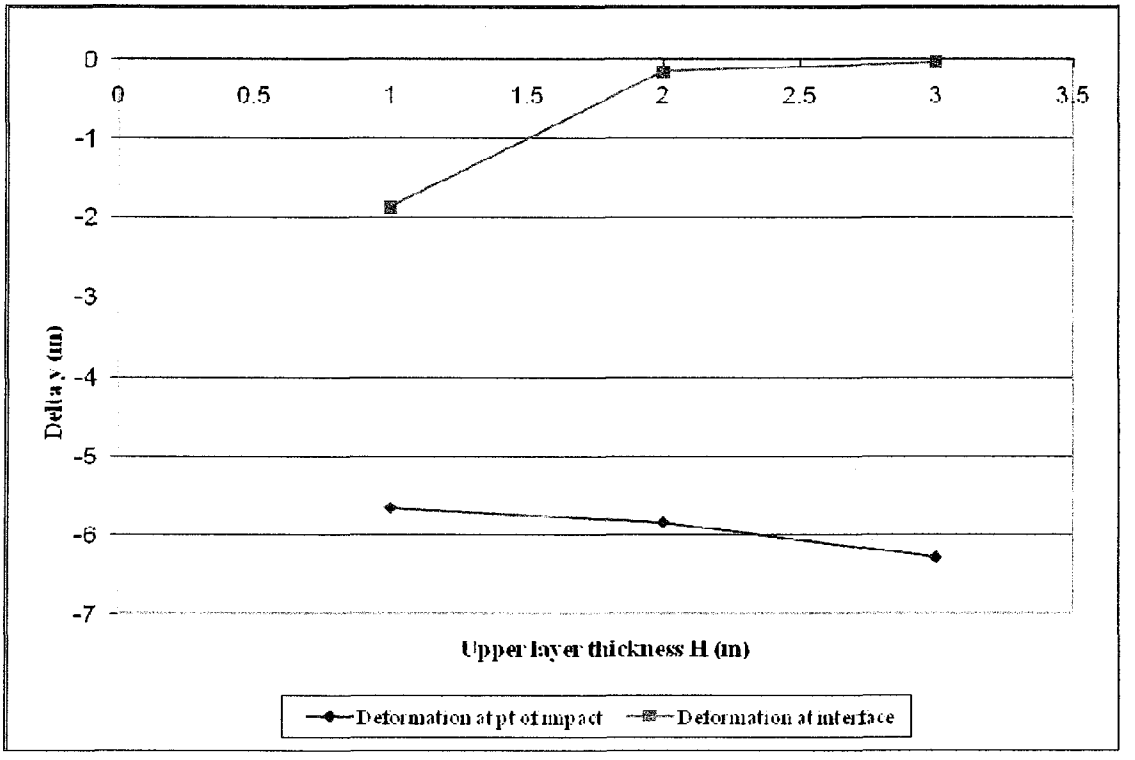

Figure 4.34: Vertical deformation versus depth for sample 1 with E2=20000 kPa

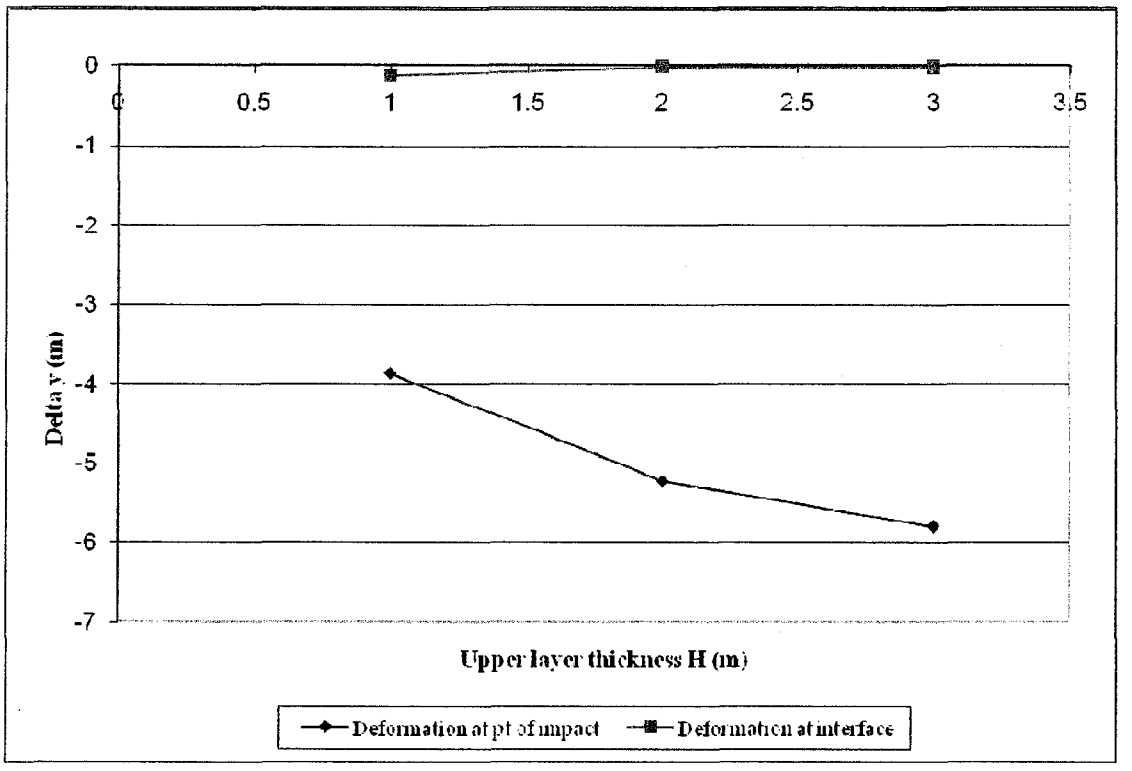

Figure 4.35: Vertical deformation versus depth for sample 1 with E2=65000 kPa

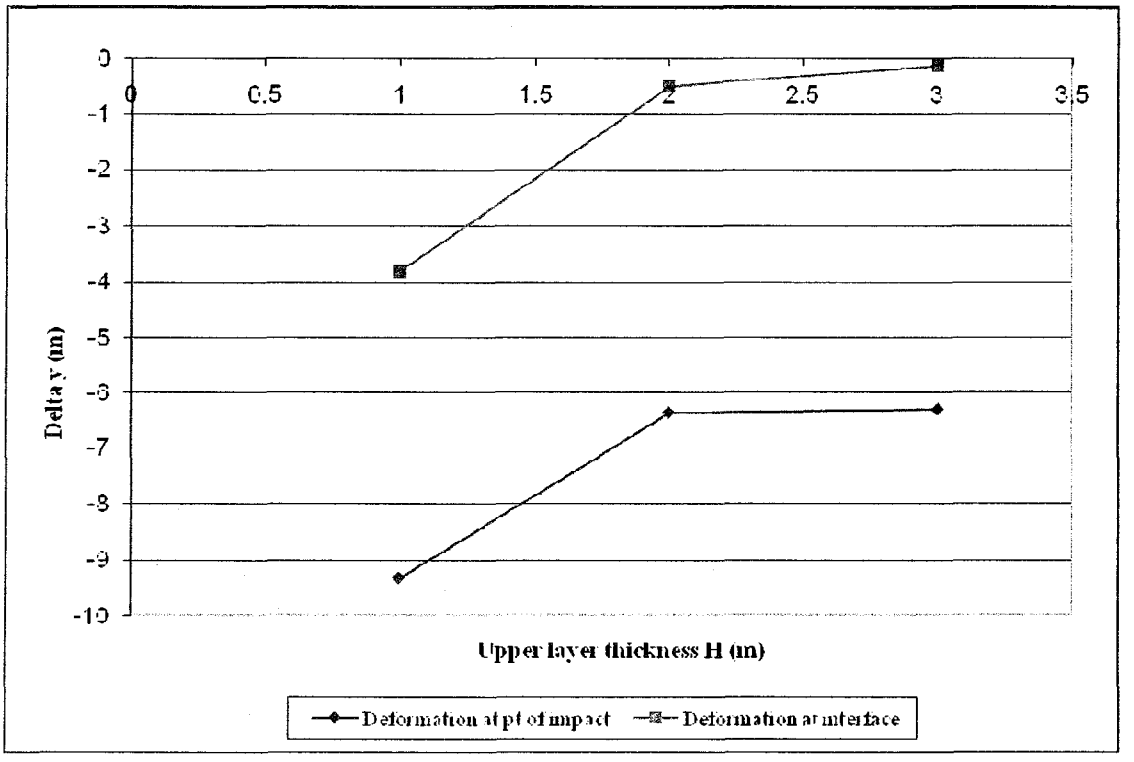

Figure 4.36: Vertical deformation versus depth for sample 2 with E2=2500 kPa

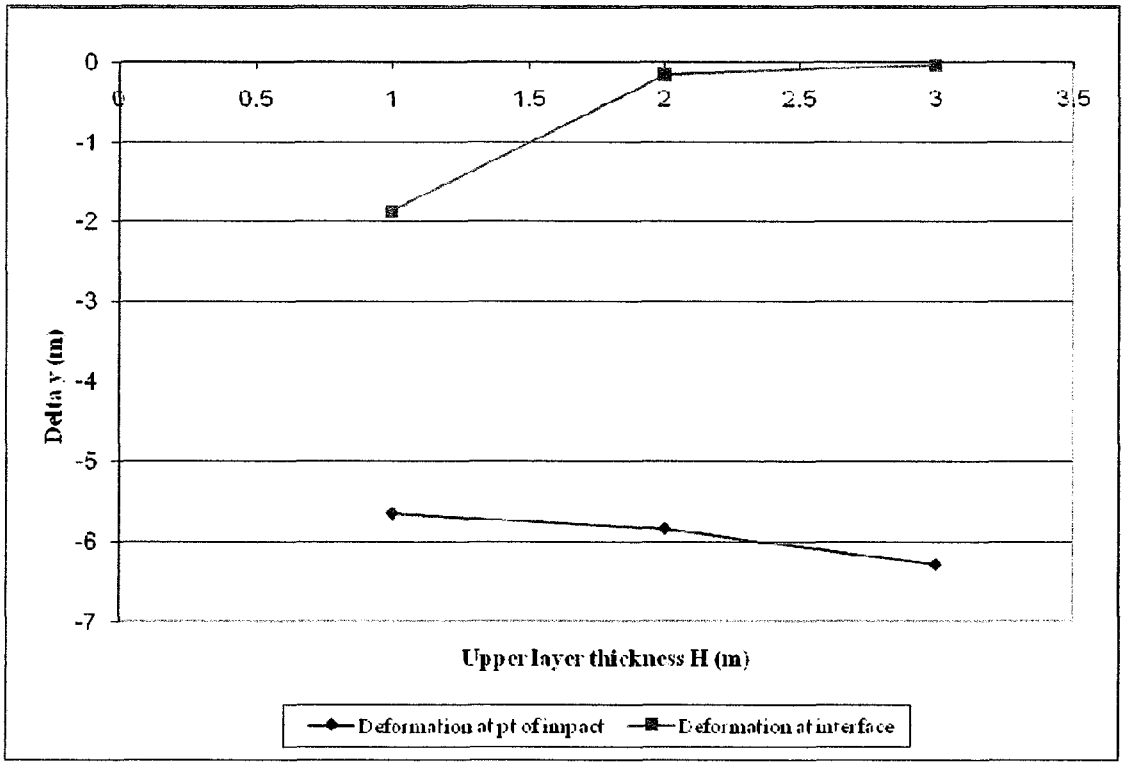

Figure 4.37: Vertical deformation versus depth for sample 2 with E2=20000 kPa

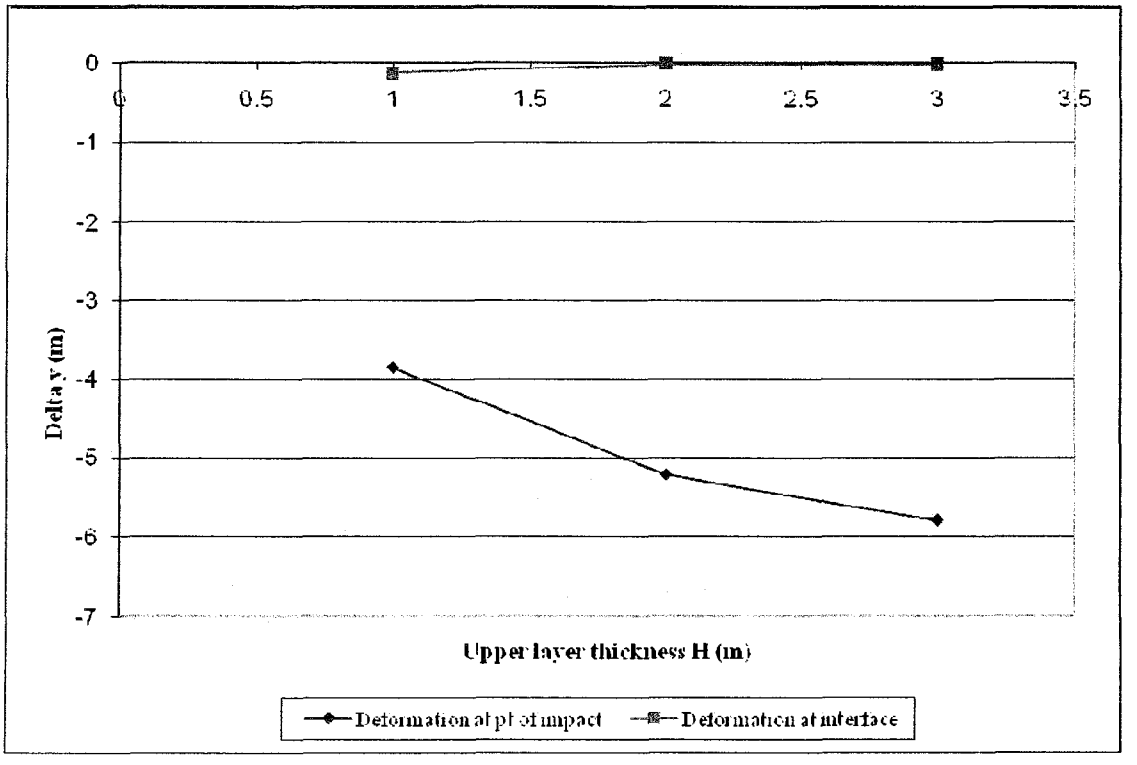

Figure 4.38: Vertical deformation versus depth for sample 2 with E2=65000 kPa

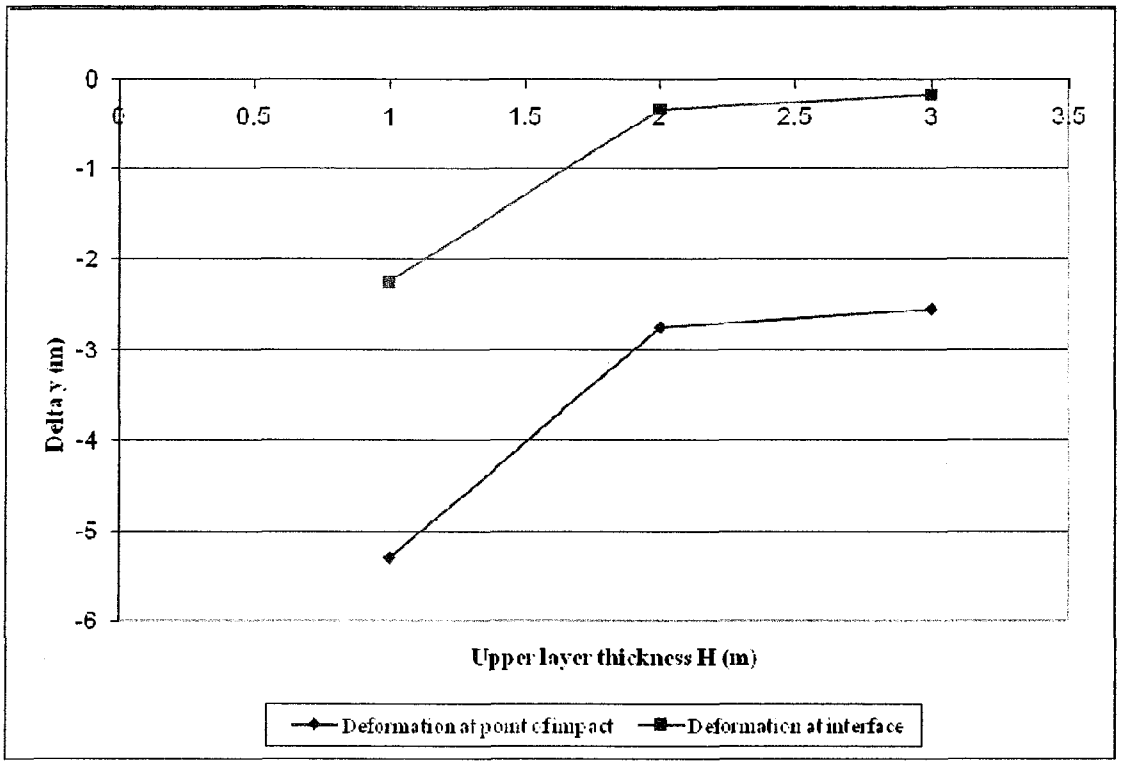

Figure 4.39: Vertical deformation versus depth for sample 3 with E2=2500 kPa

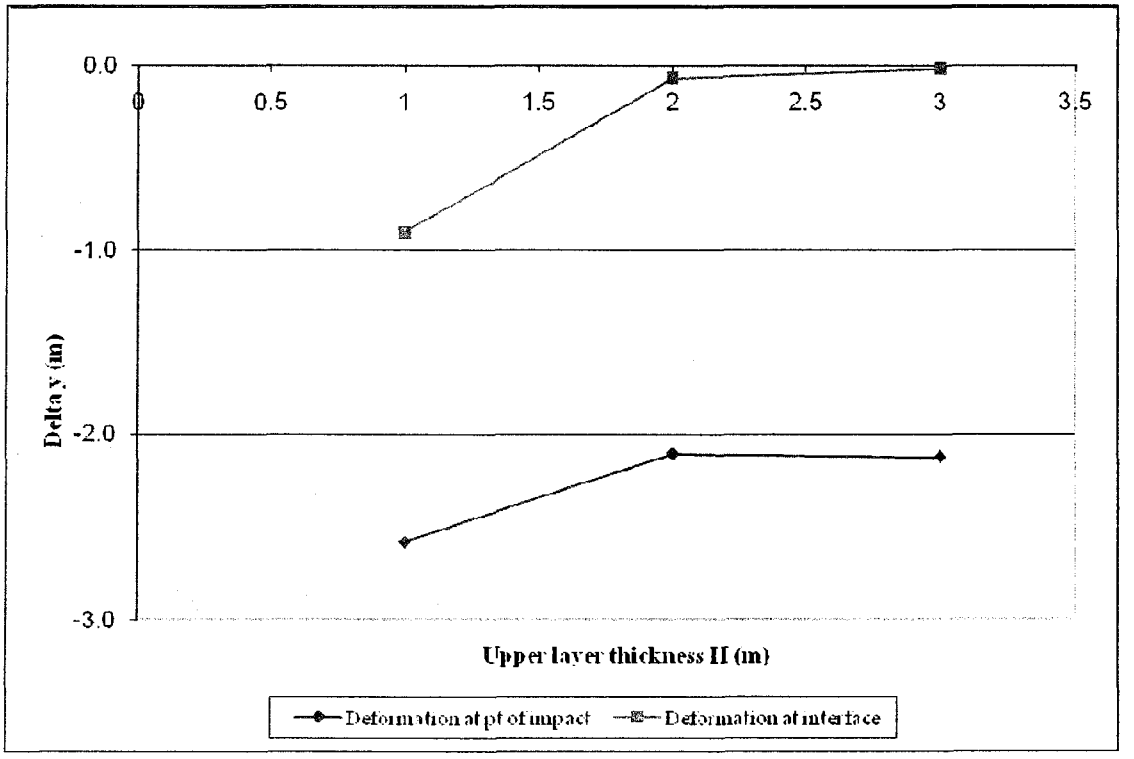

Figure 4.40: Vertical deformation versus depth for sample 3 with E2=20000 kPa

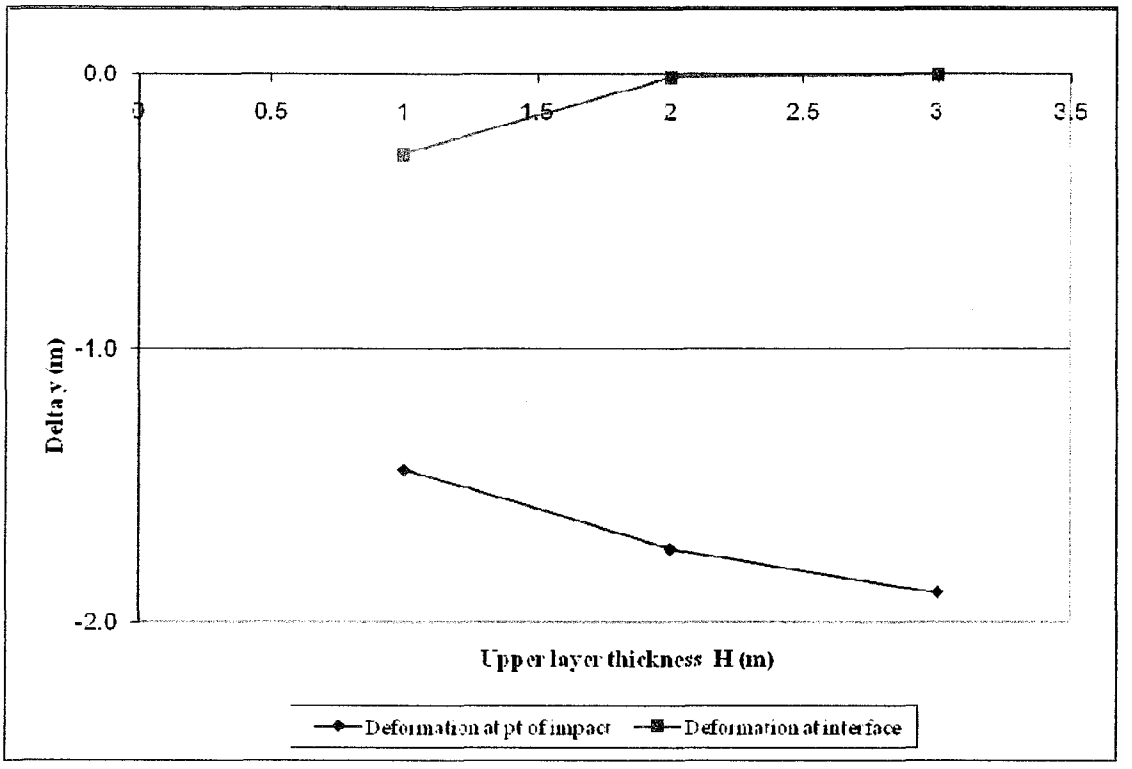

Figure 4.41: Vertical deformation versus depth for sample 3 with E2=65000 kPa

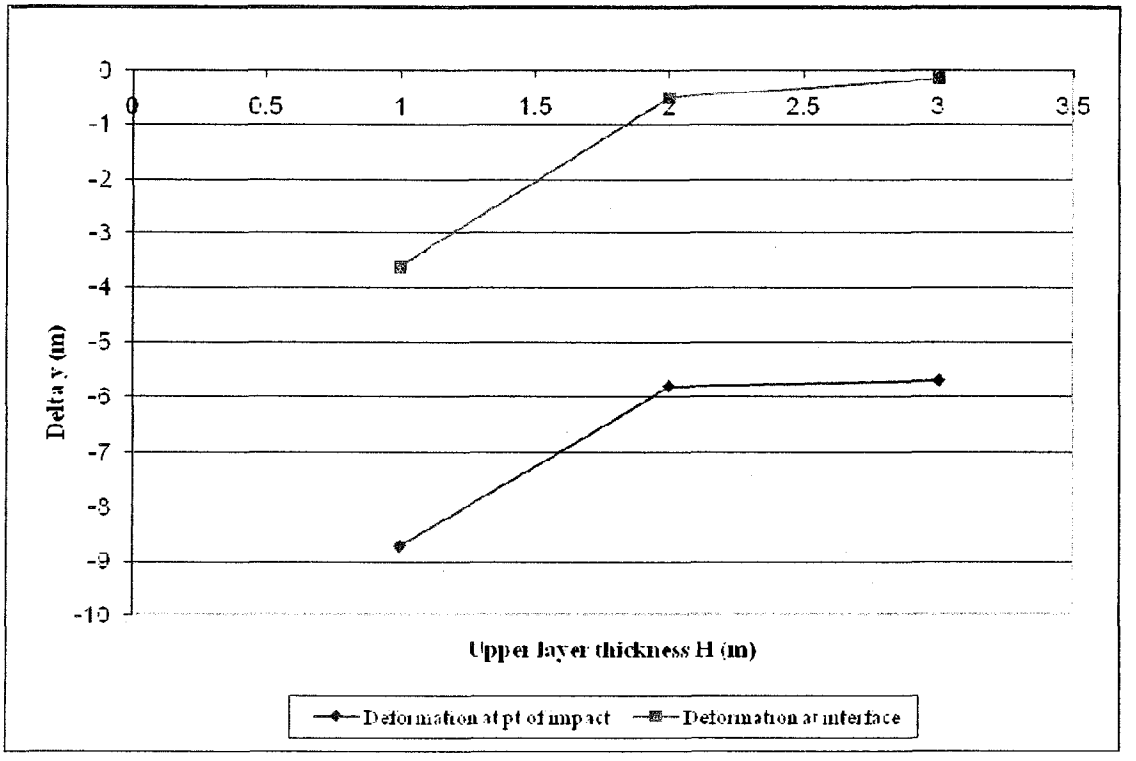

Figure 4.42: Vertical deformation versus depth for sample 4 with E2=2500 kPa

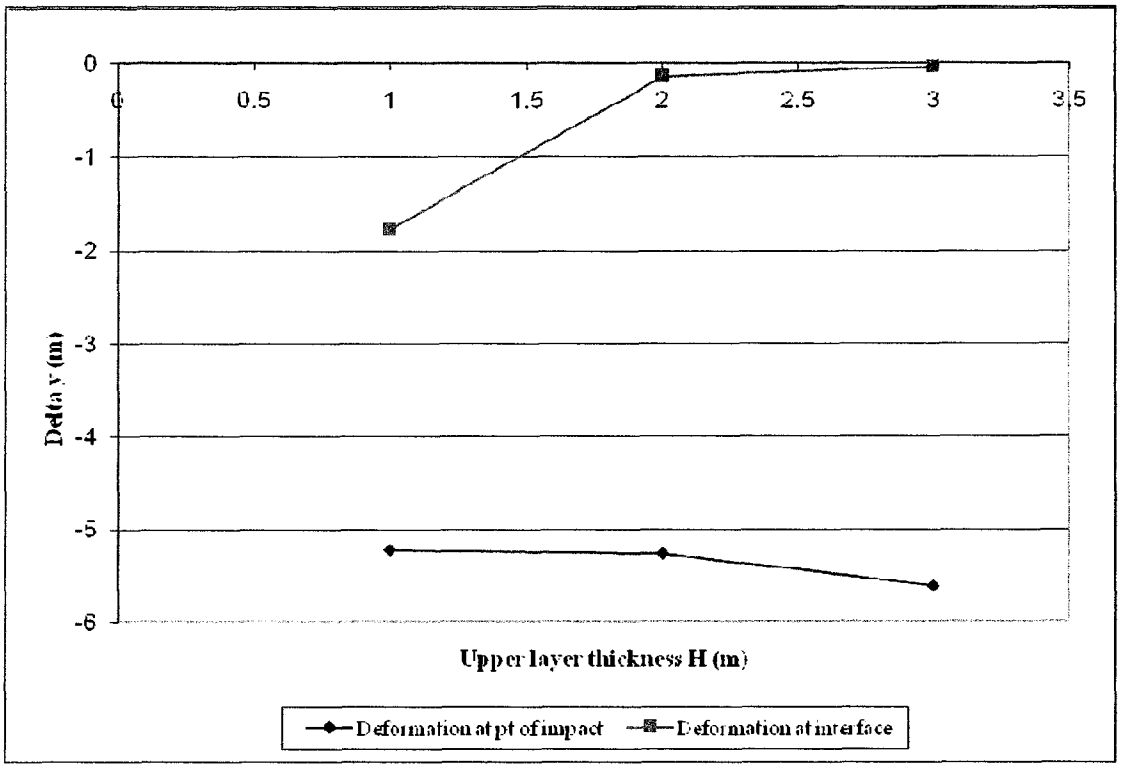

Figure 4.43: Vertical deformation versus depth for sample 4 with E2=20000 kPa

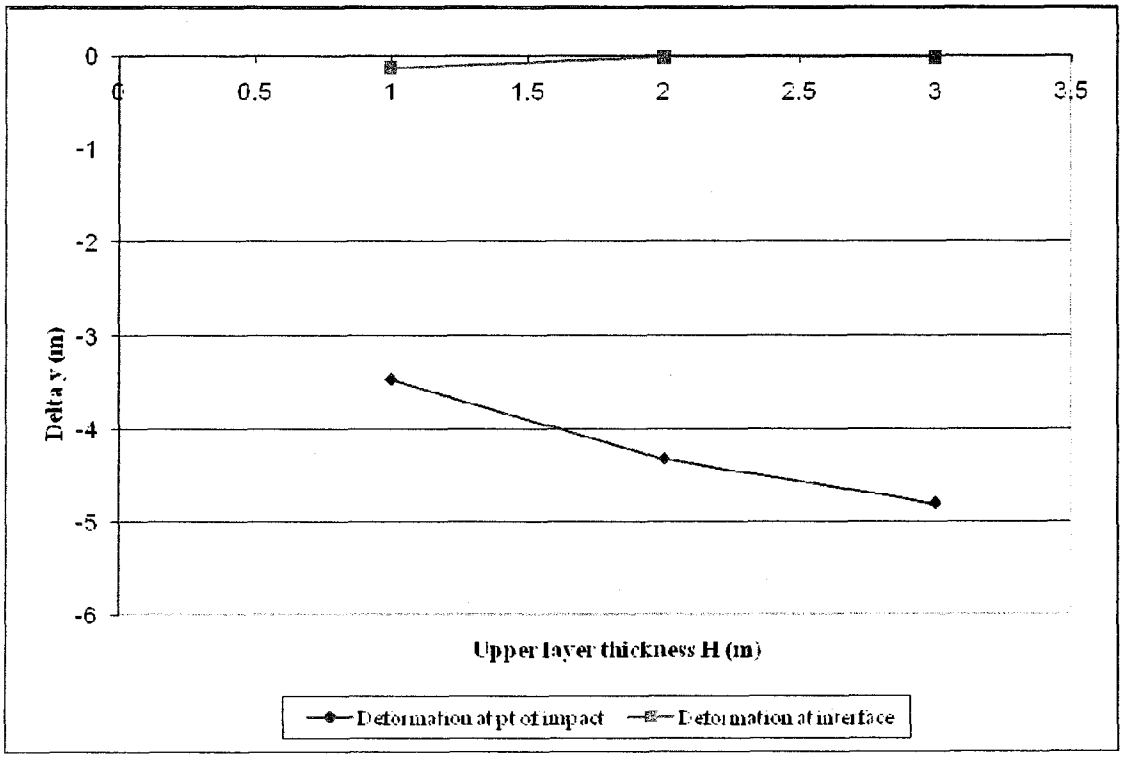

Figure 4.44: Vertical deformation versus depth for sample 4 with E2=65000 kPa

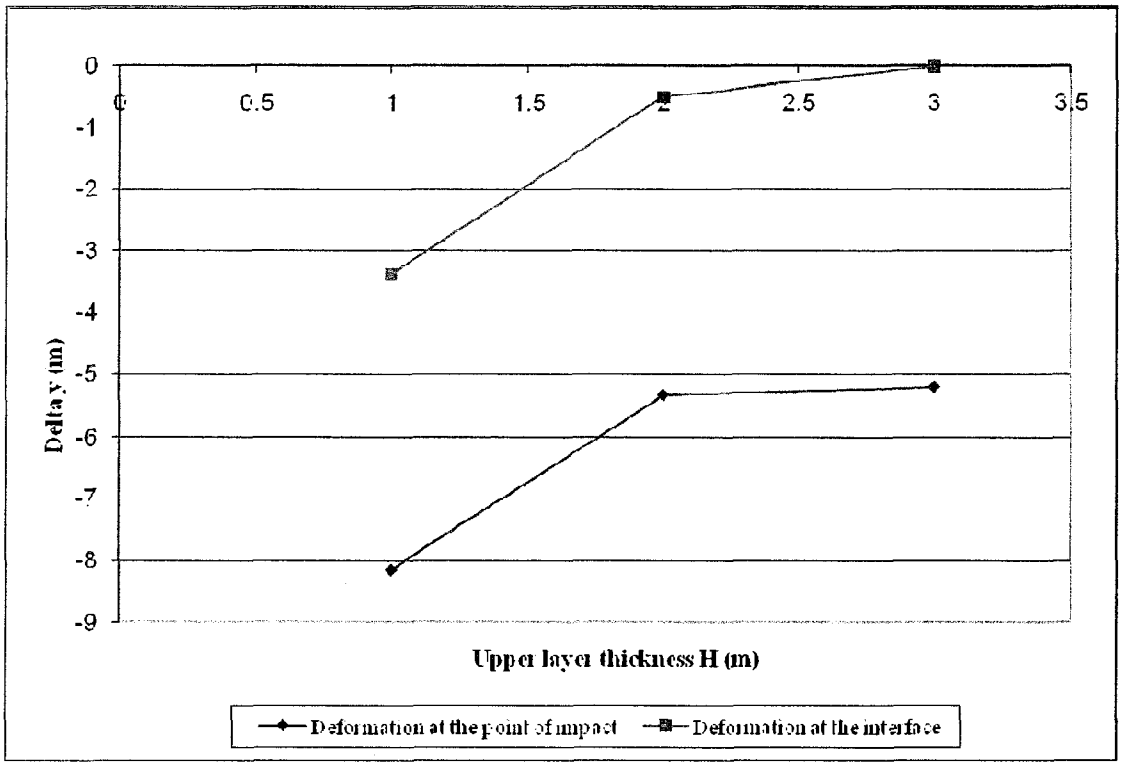

Figure 4.45: Vertical deformation versus depth for sample 5 with E2=2500 kPa

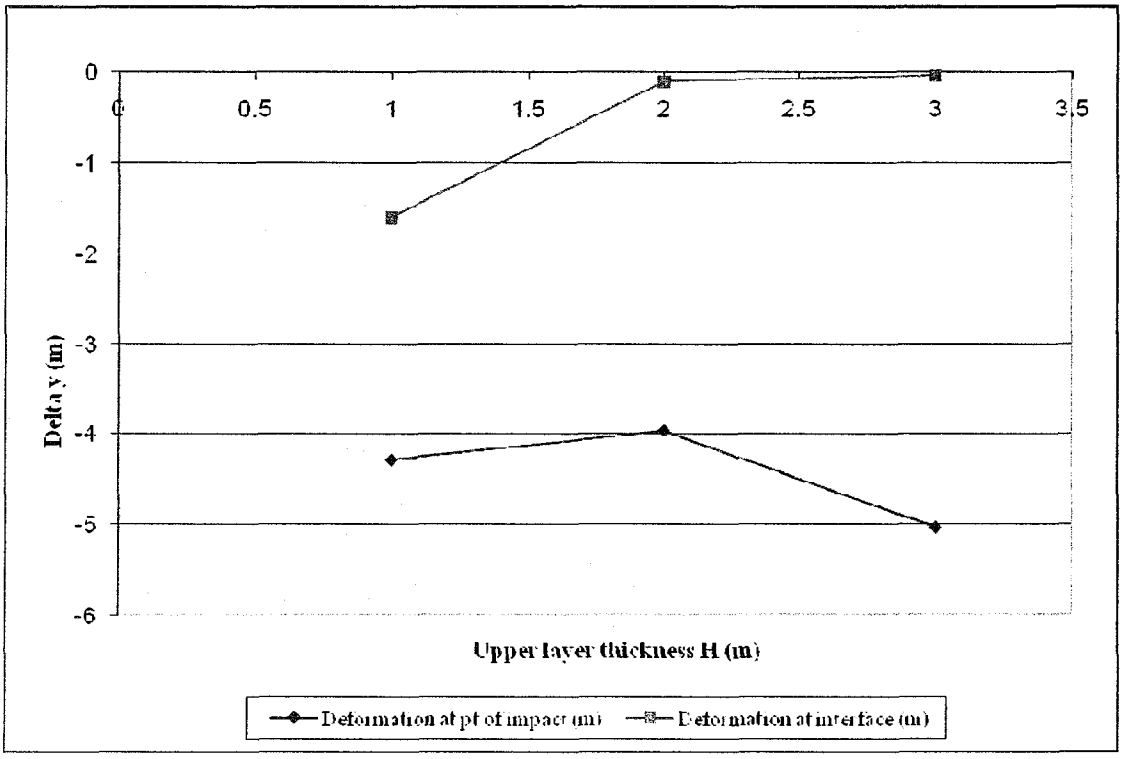

Figure 4.46: Vertical deformation versus depth for sample 5 with E2=20000 kPa

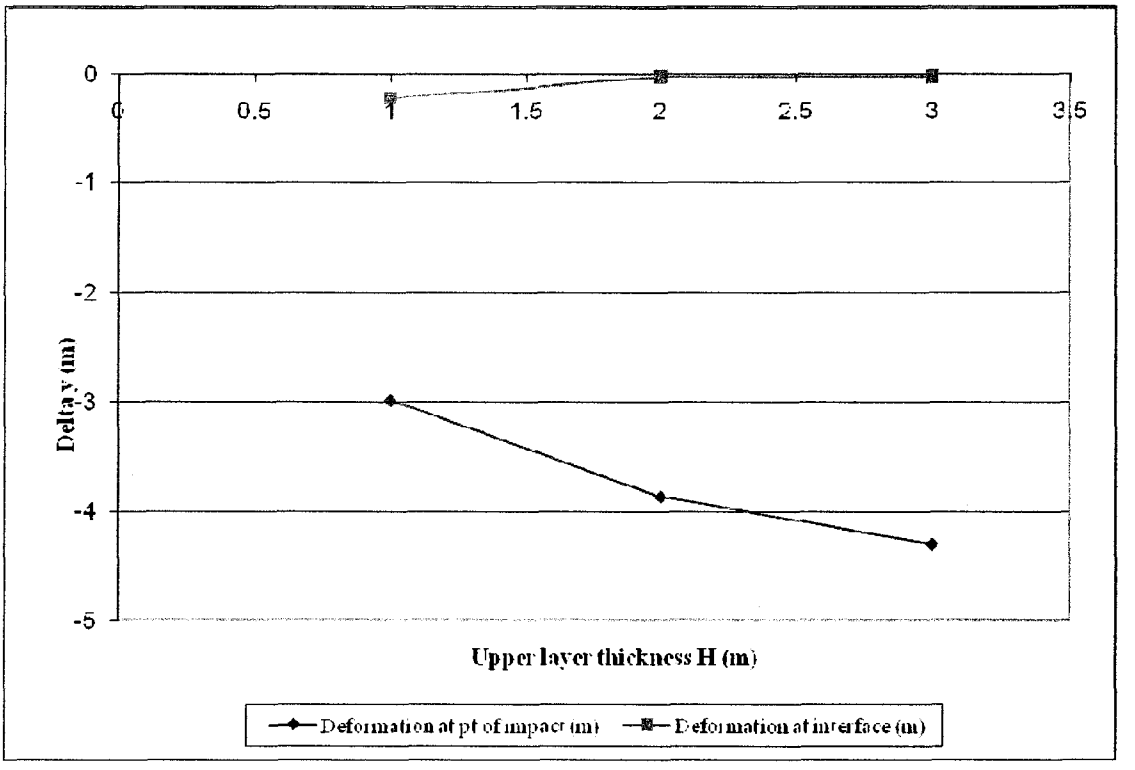

Figure 4.47: Vertical deformation versus depth for sample 5 with E2=65000 kPa

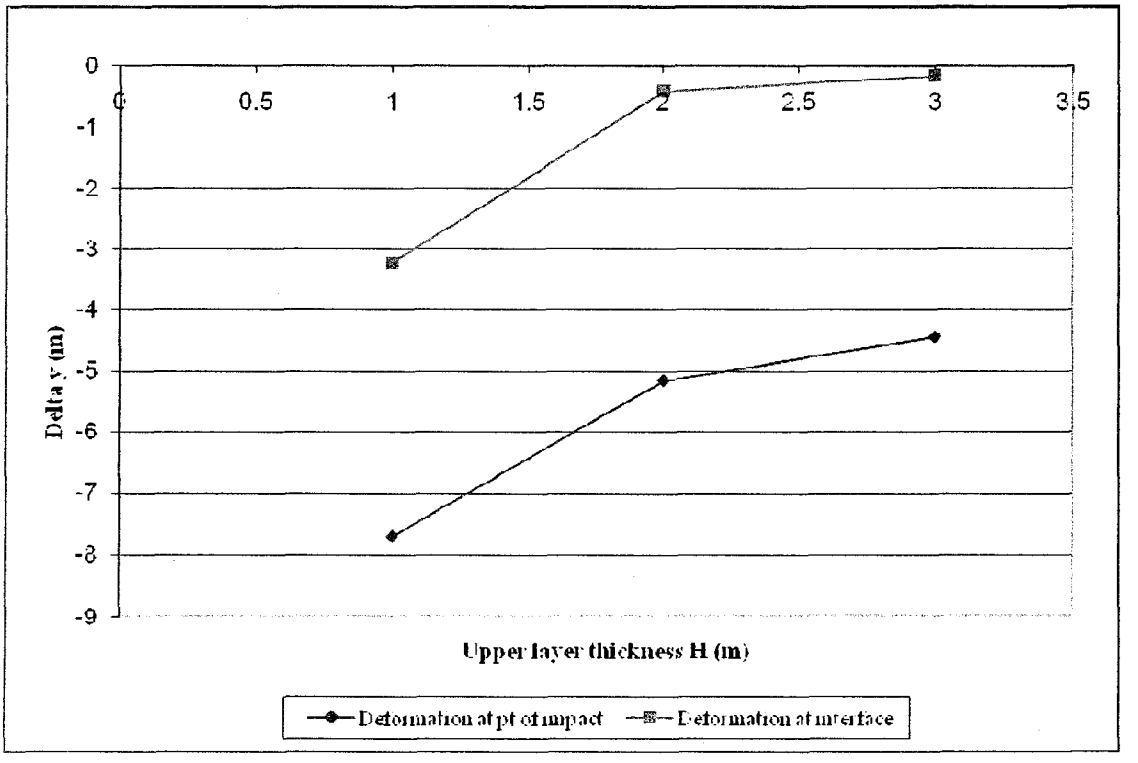

Figure 4.48: Vertical deformation versus depth for sample 6 with E2=2500 kPa

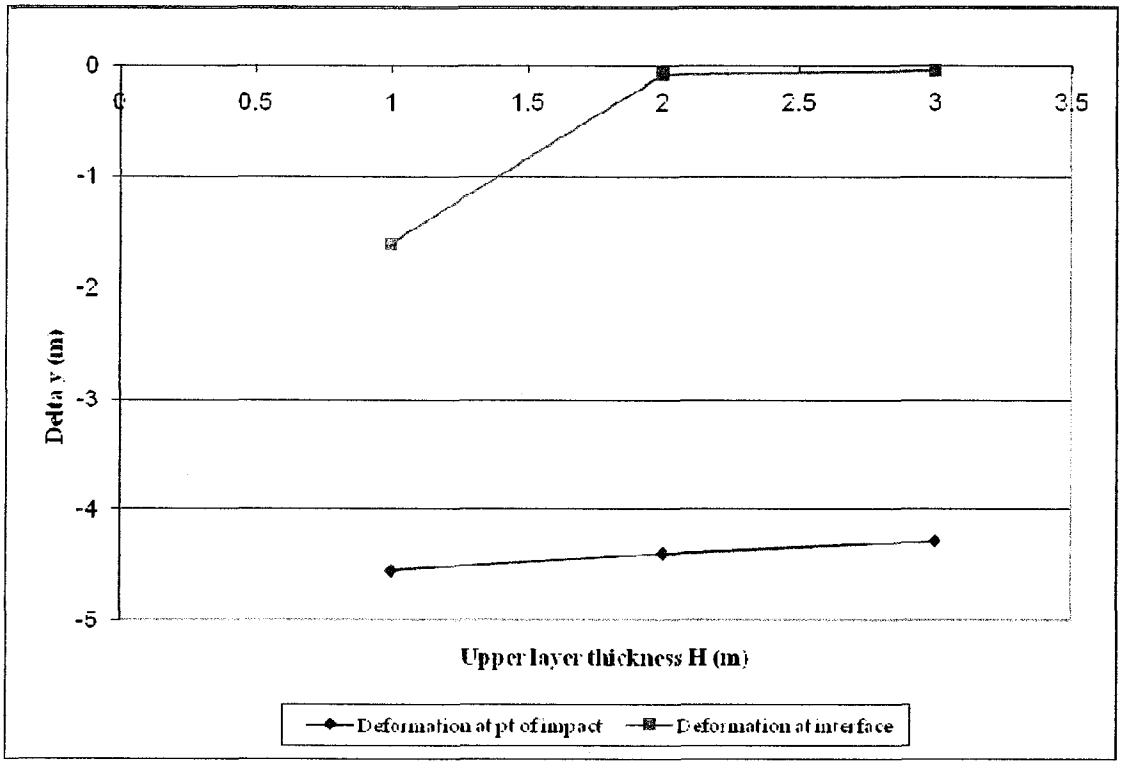

Figure 4.49: Vertical deformation versus depth for sample 6 with E2=20000 kPa

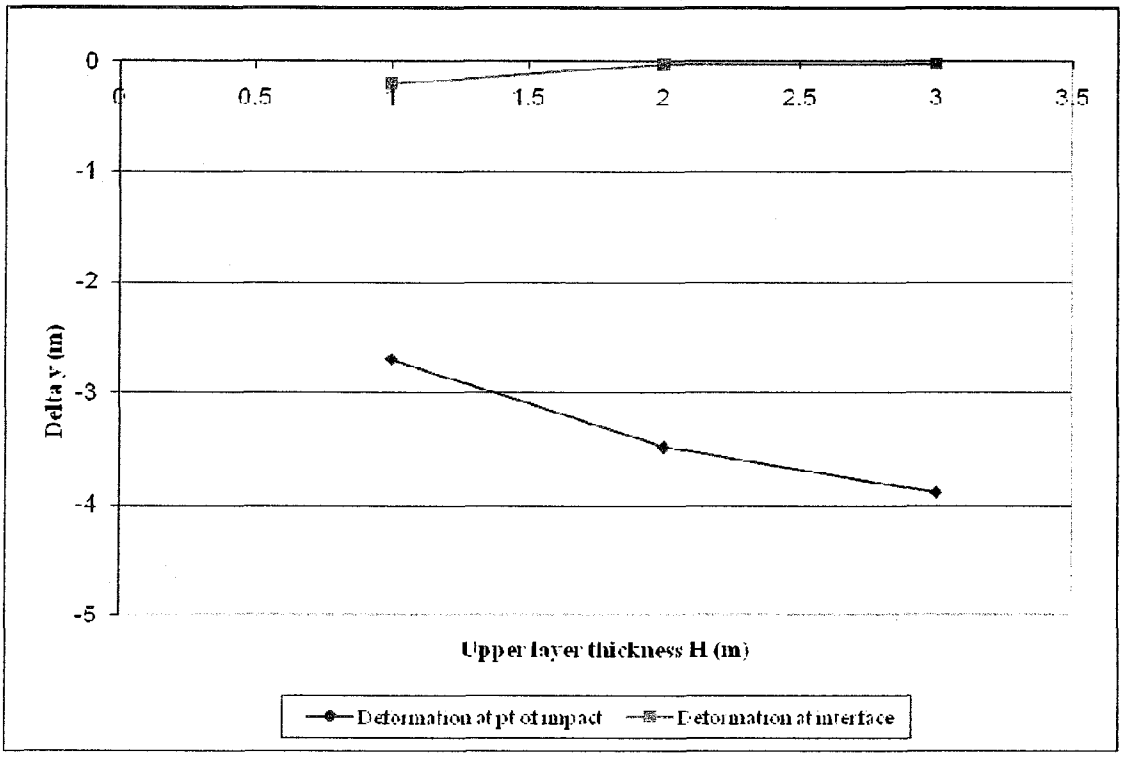

Figure 4.50: Vertical deformation versus depth for sample 6 with E2=65000 kPa

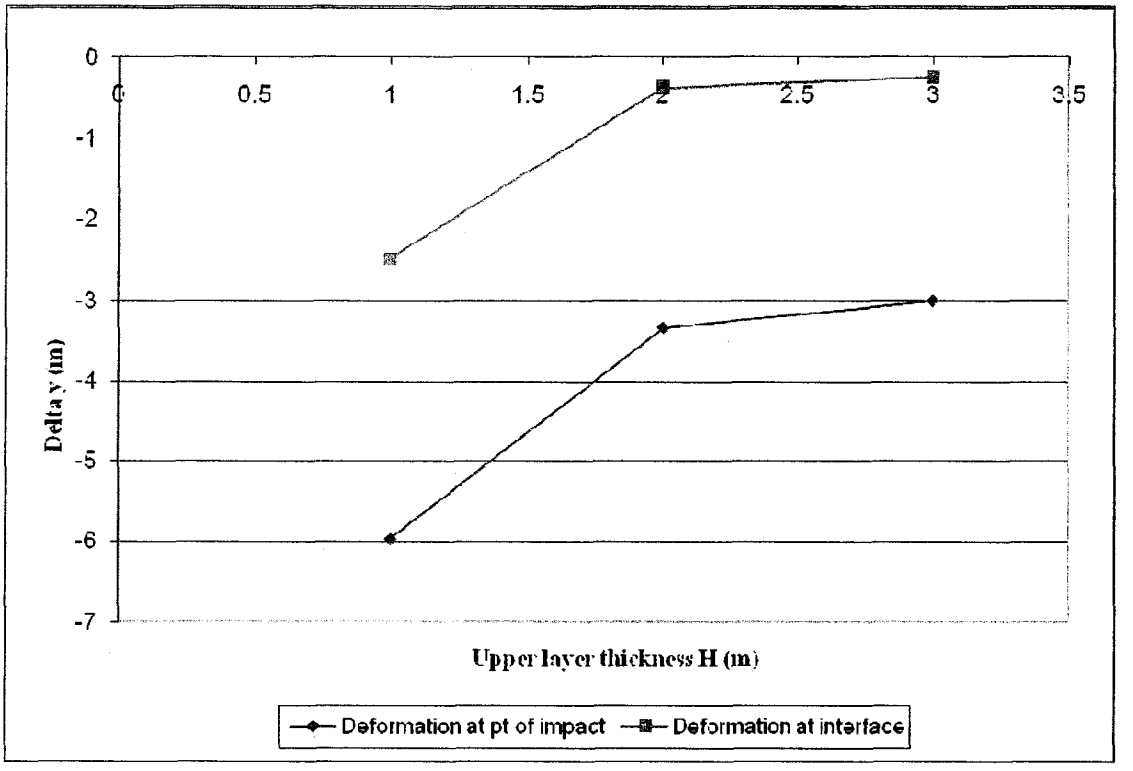

Figure 4.51: Vertical deformation versus depth for sample 7 with E2=2500 kPa

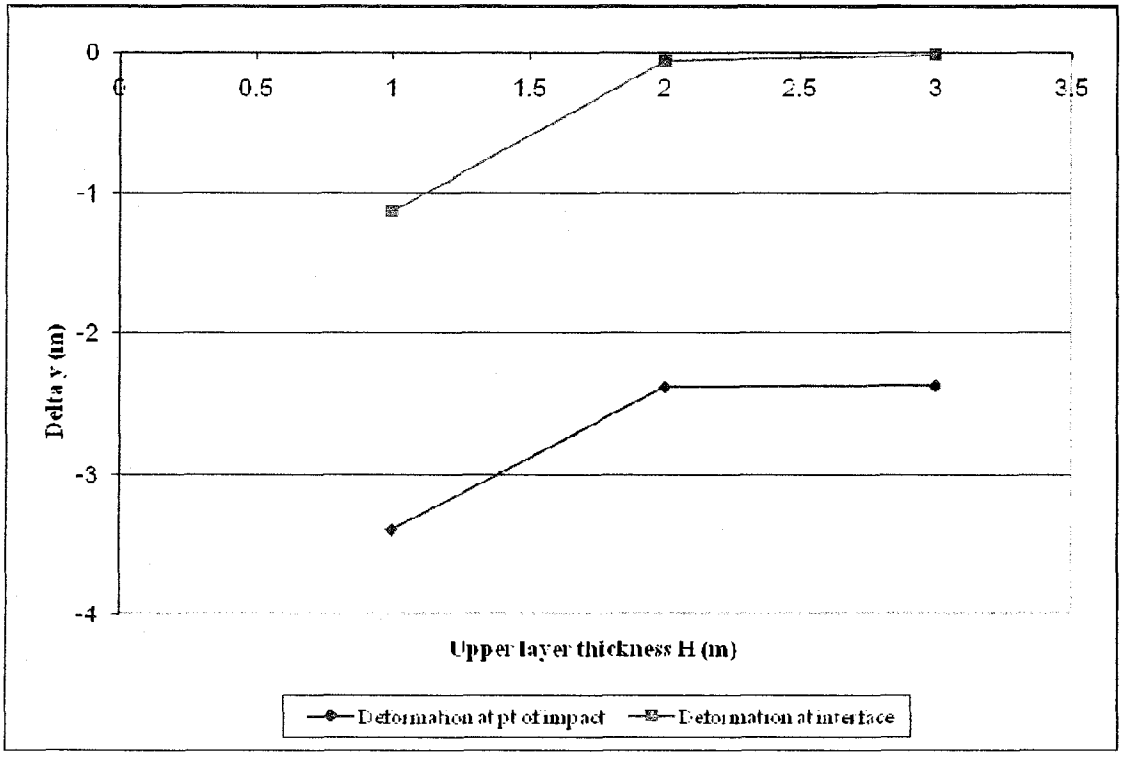

Figure 4.52: Vertical deformation versus depth for sample 7 with E2=20000 kPa

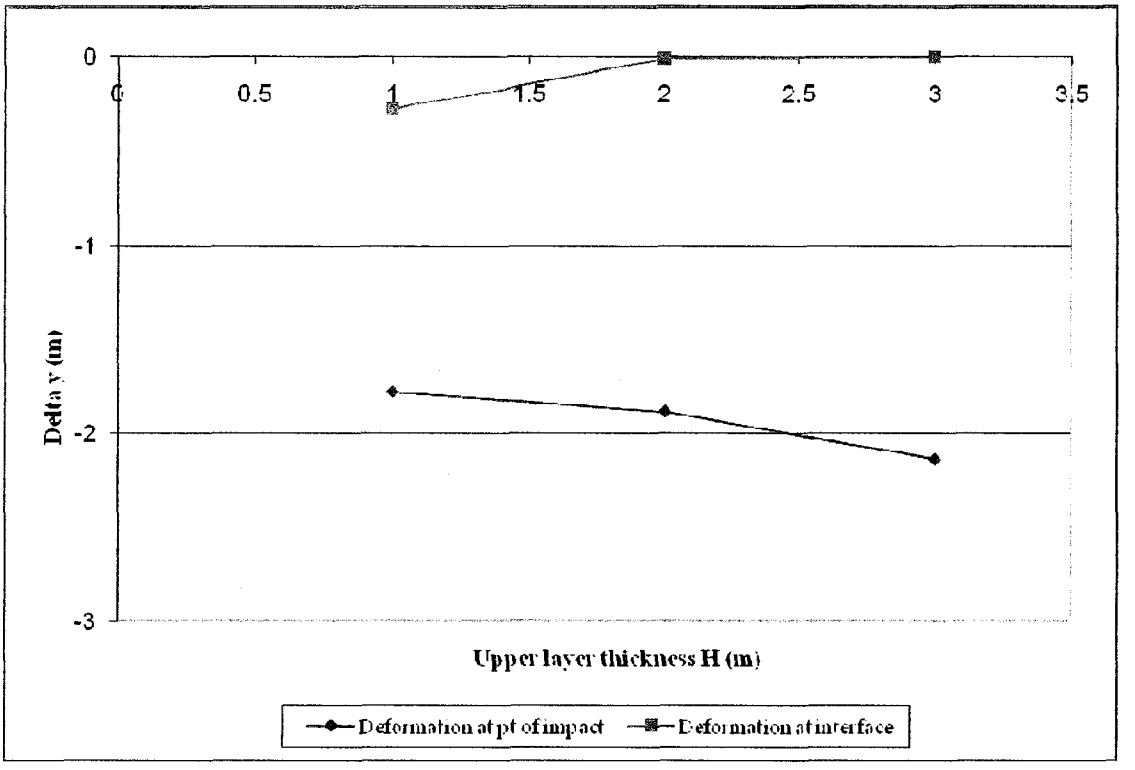

Figure 4.53: Vertical deformation versus depth for sample 7 with E2=65000 kPa

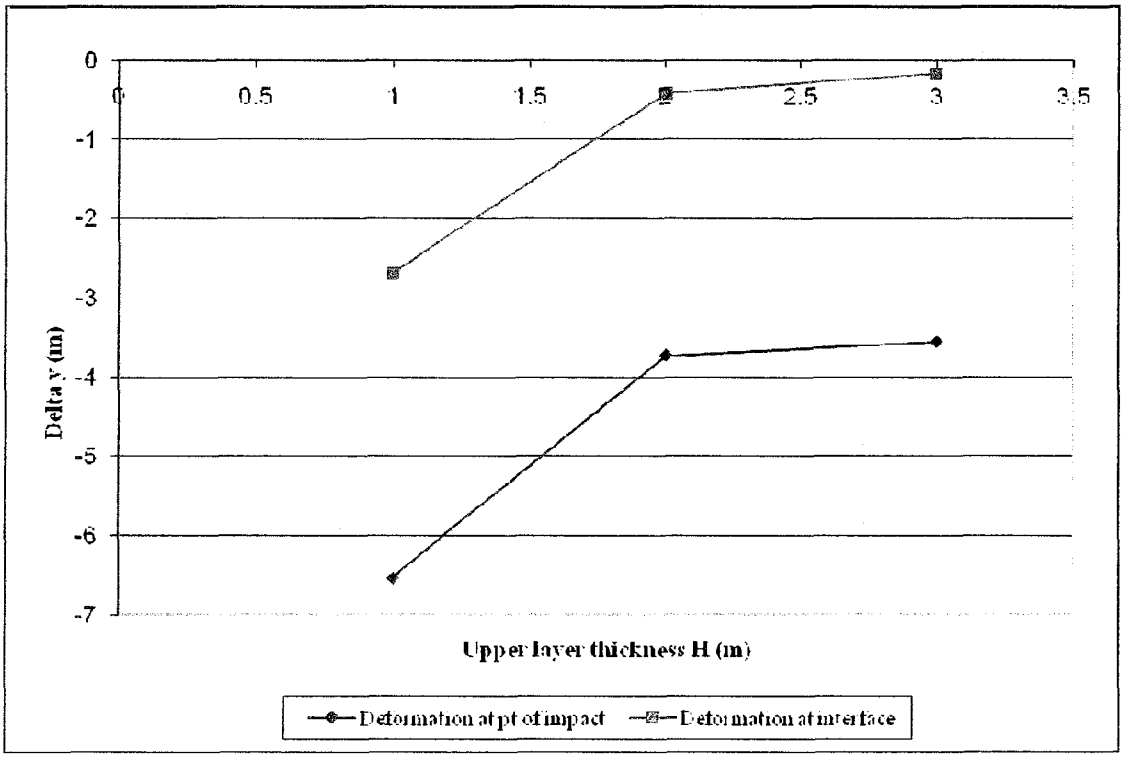

Figure 4.54: Vertical deformation versus depth for sample 8 with E2=2500 kPa

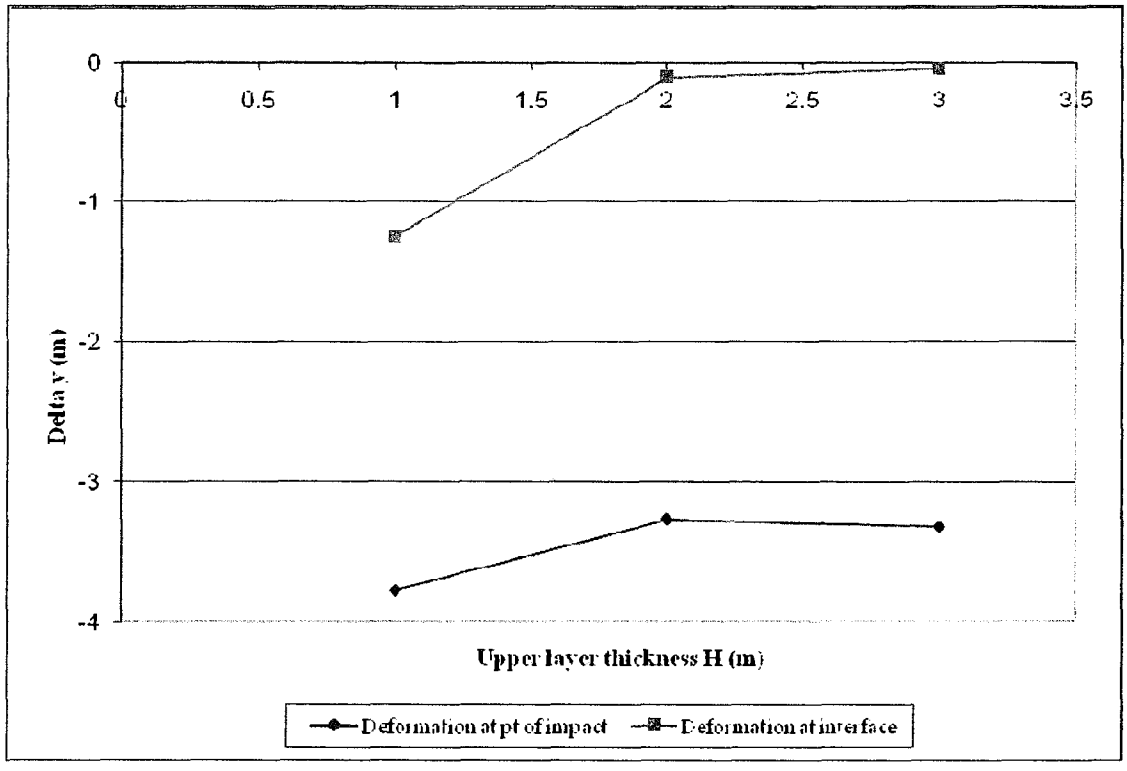

Figure 4.55: Vertical deformation versus depth for sample 8 with E2=20000 kPa

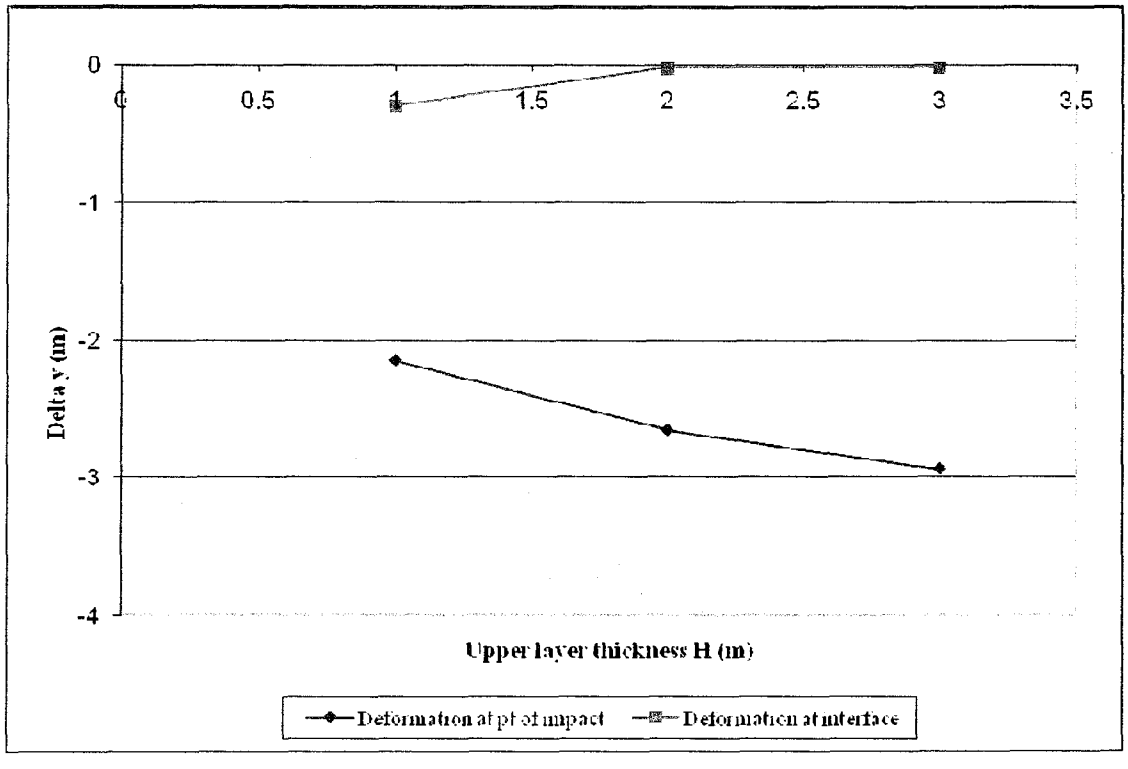

Figure 4.56: Vertical deformation versus depth for sample 8 with E2=65000 kPa

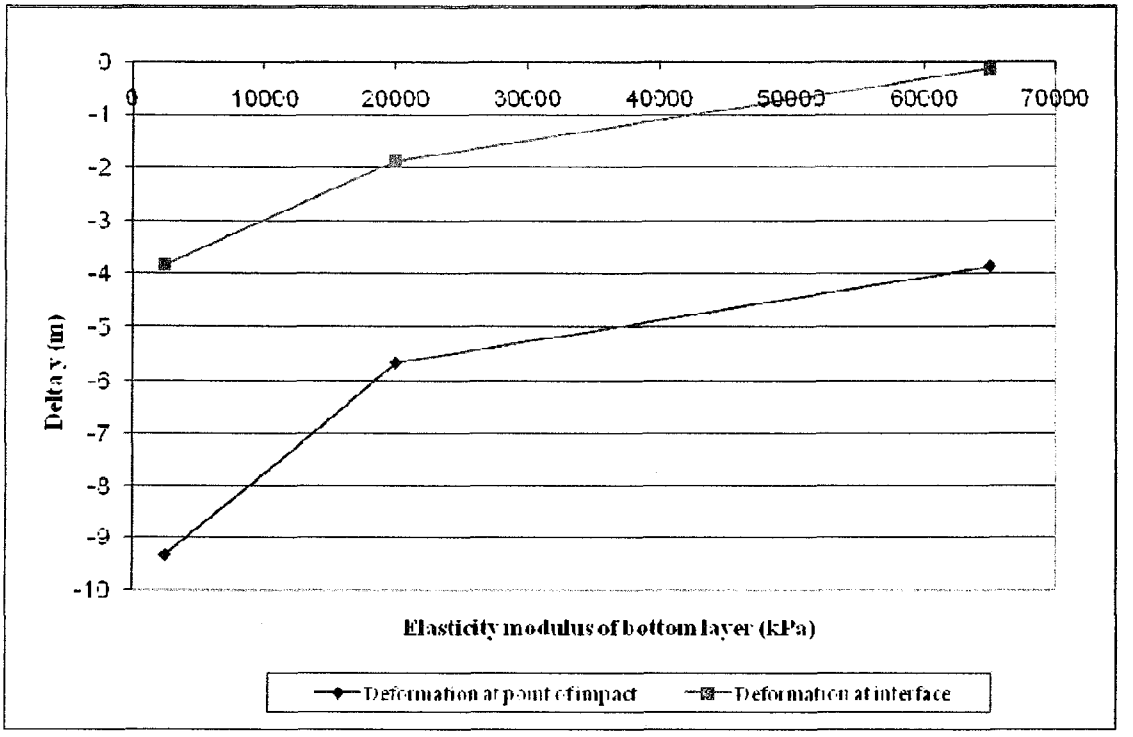

Figure 4.57: Δy of 1 m thick upper layer of sample 1 varying with E2

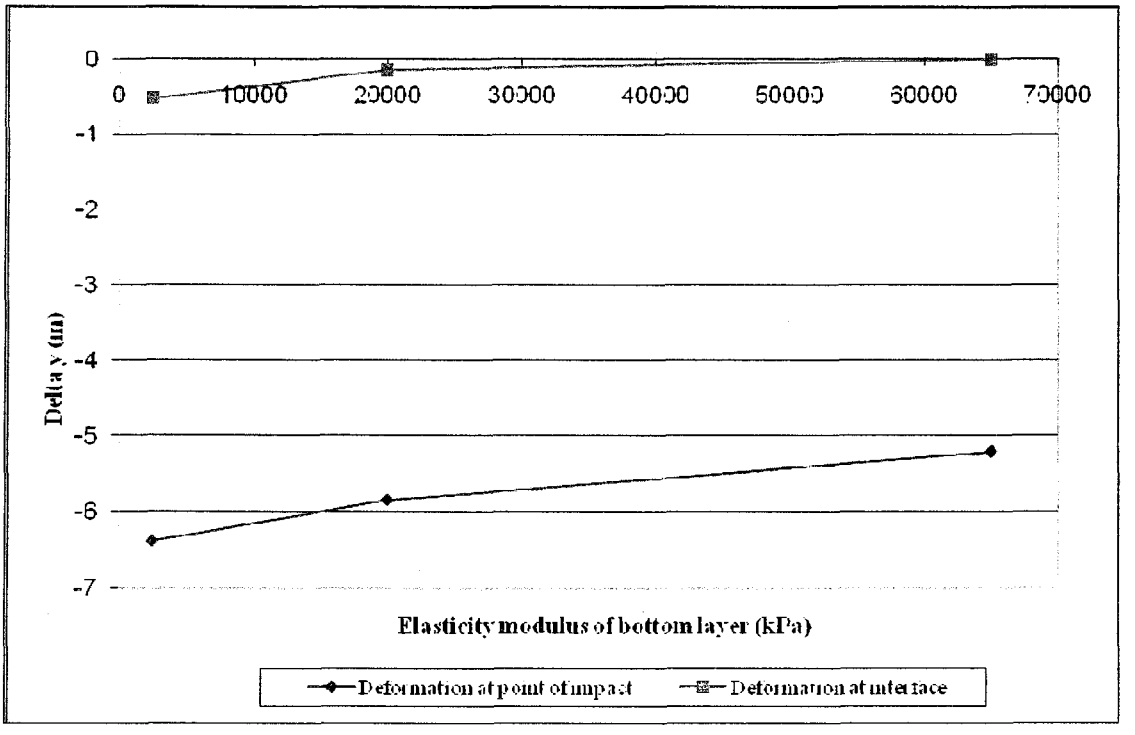

Figure 4.58: Δy of 2 m thick upper layer of sample 1 varying with E2

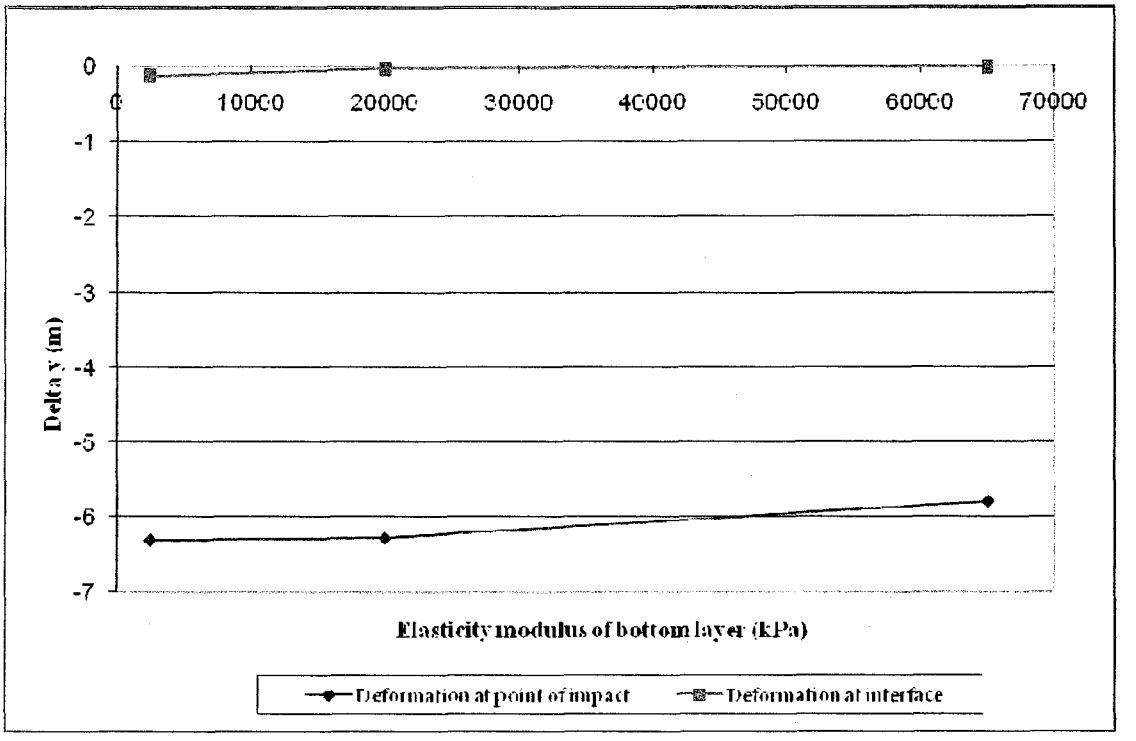

Figure 4.59: Δy of 3 m thick upper layer of sample 1 varying with E2

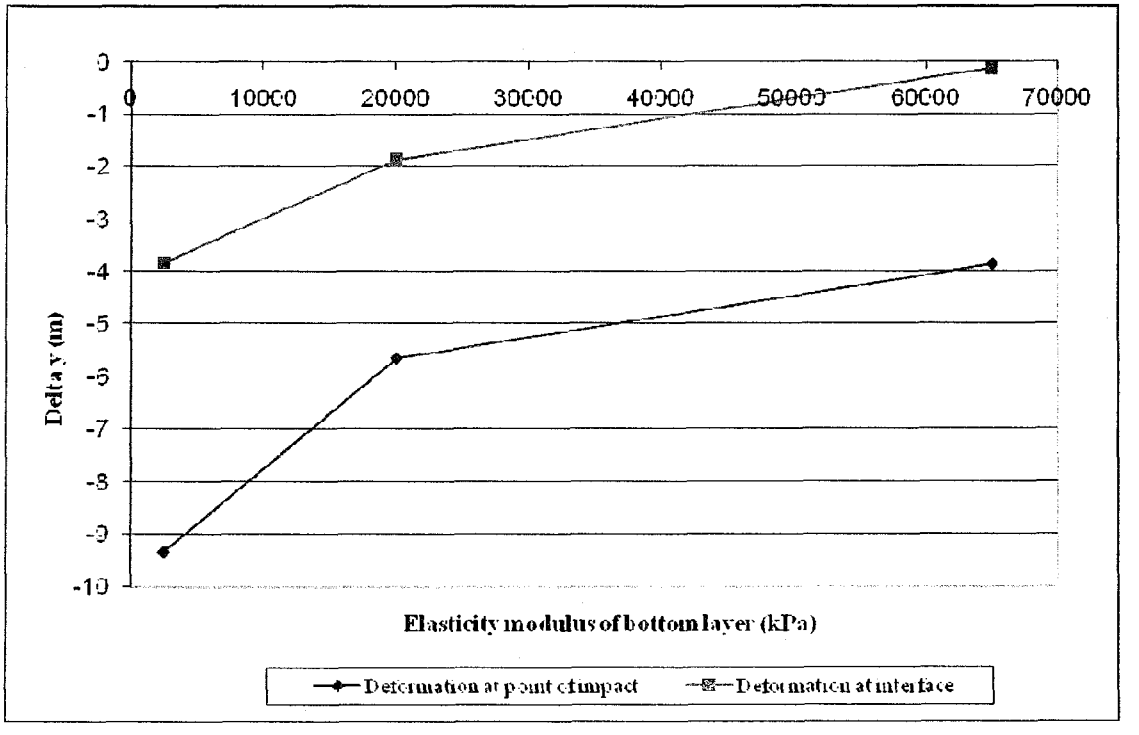

Figure 4.60: Δy of 1 m thick upper layer of sample 2 varying with E2

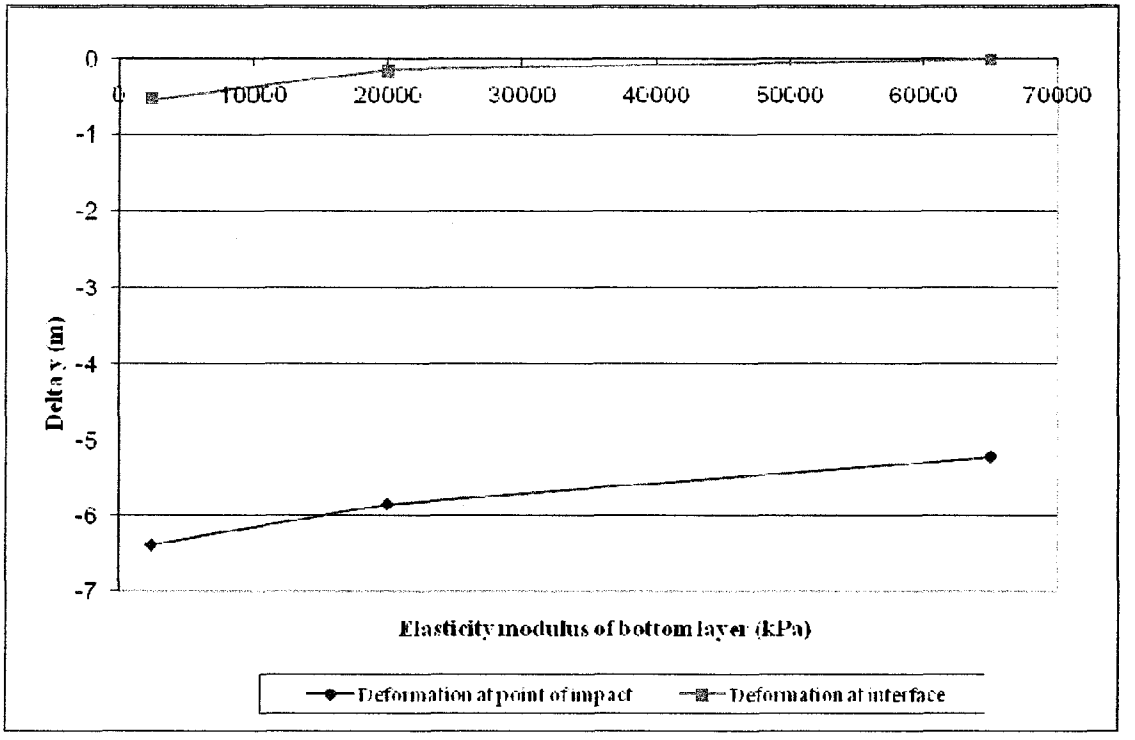

Figure 4.61: Δy of 2 m thick upper layer of sample 2 varying with E2

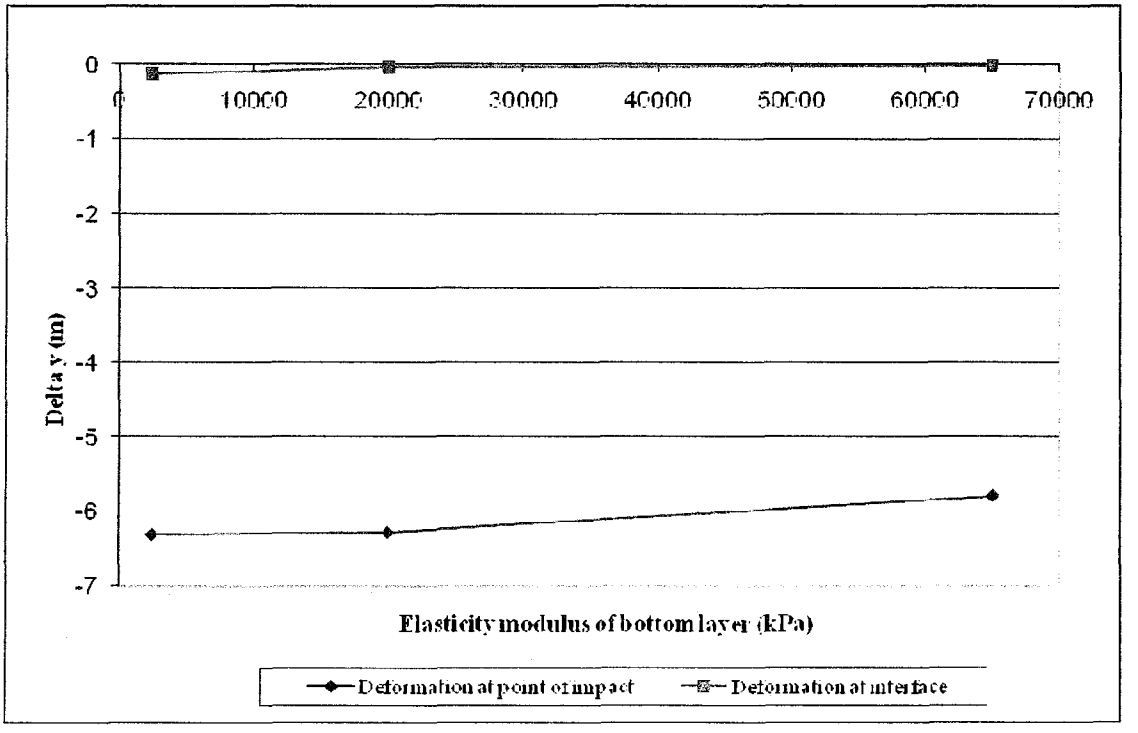

Figure 4.62: Δy of 3 m thick upper layer of sample 2 varying with E2

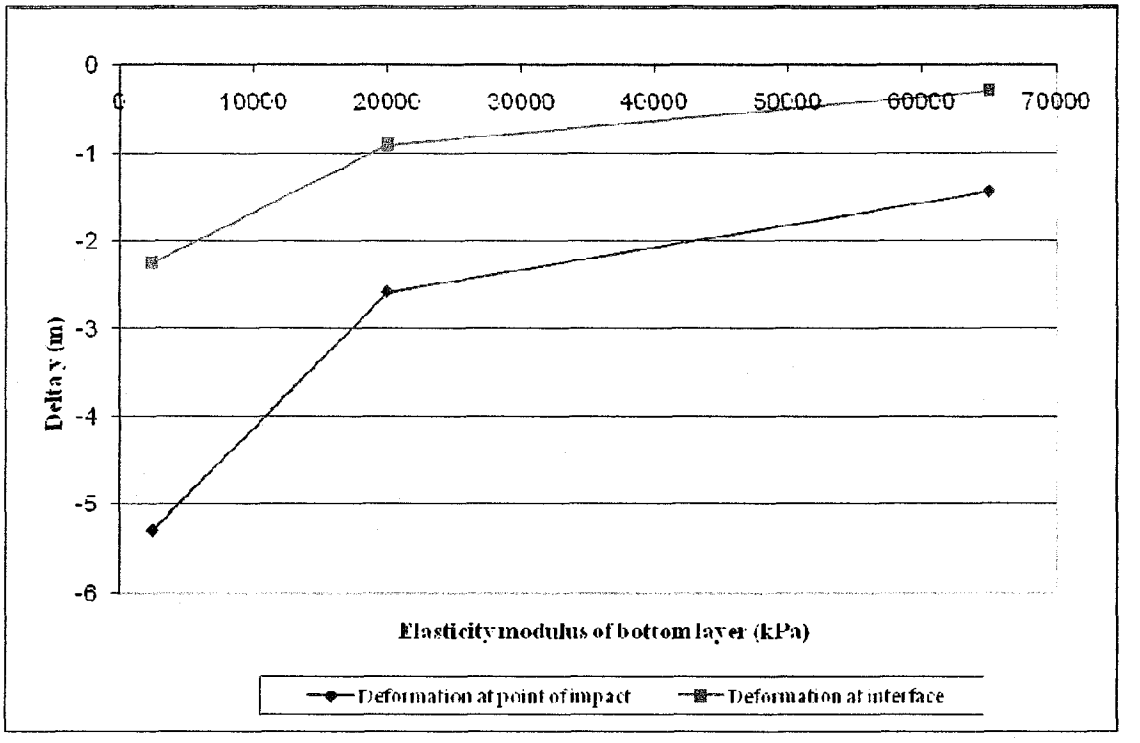

Figure 4.63: Δy of 1 m thick upper layer of sample 3 varying with E2

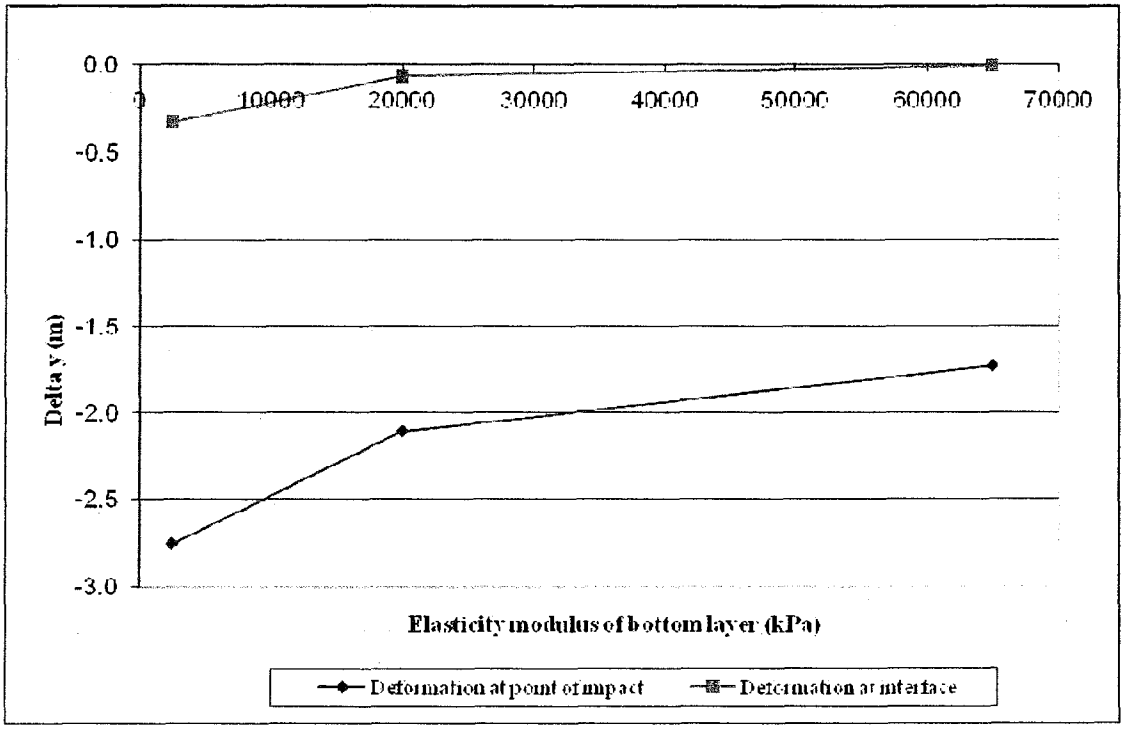

Figure 4.64: Δy of 2 m thick upper layer of sample 3 varying with E2

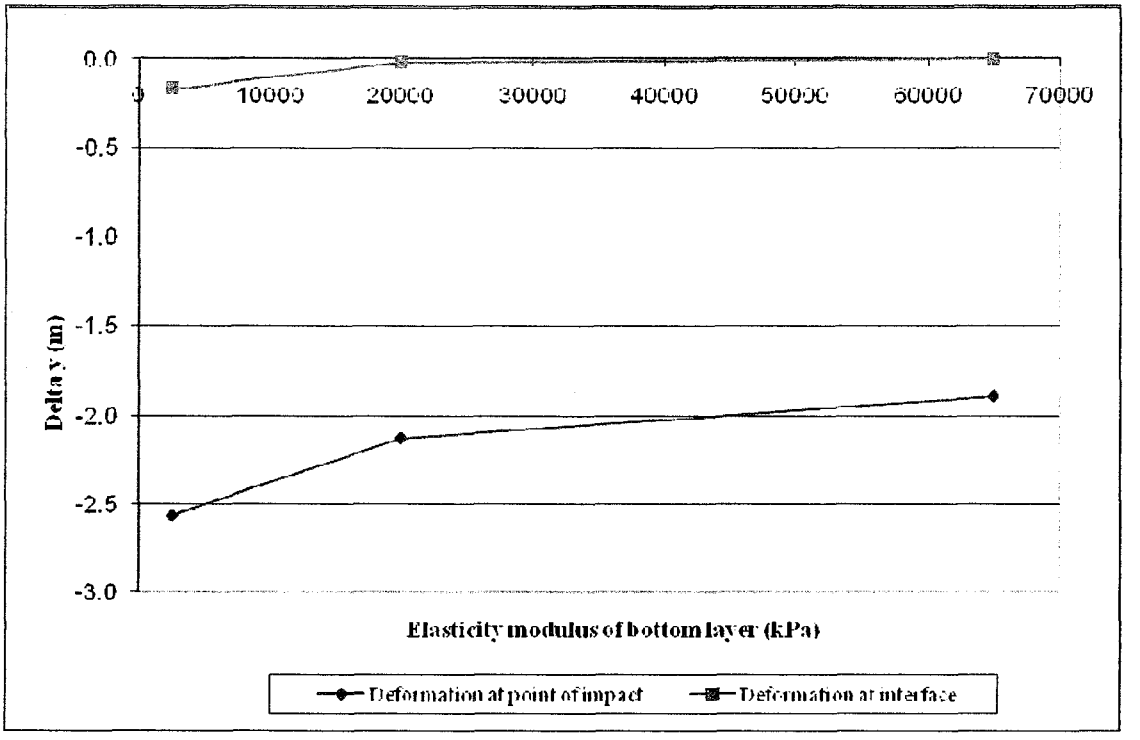

Figure 4.65: Δy of 3 m thick upper layer of sample 3 varying with E2

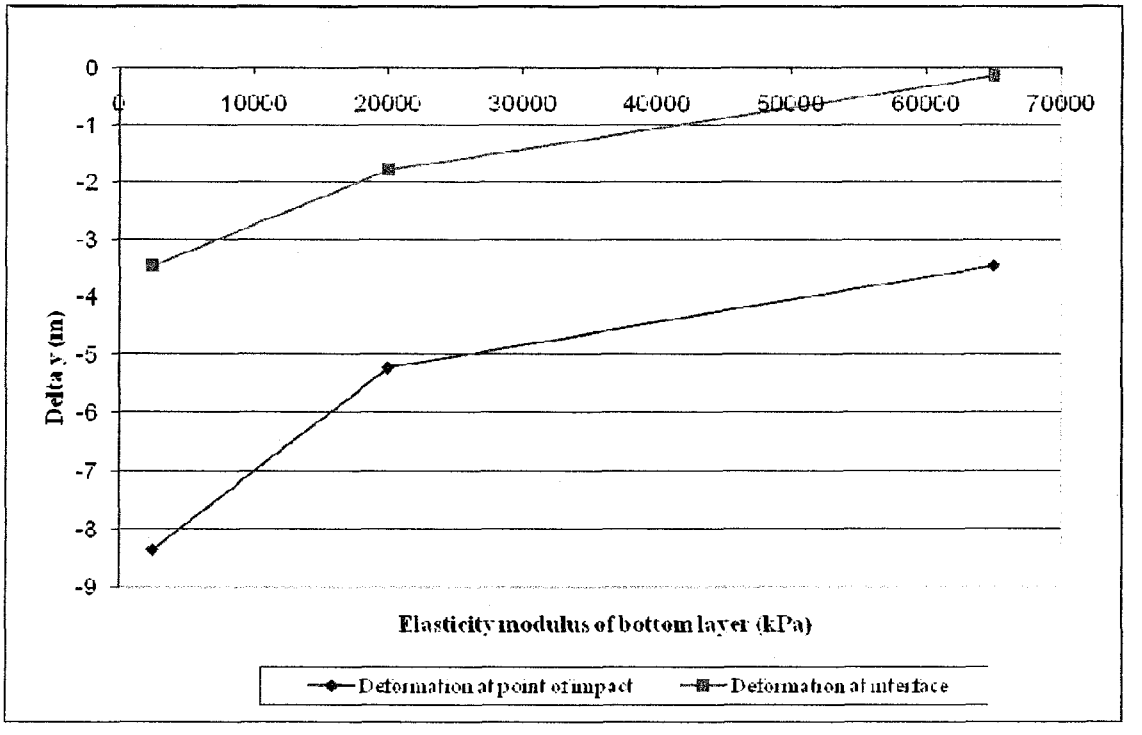

Figure 4.66: Δy of 1 m thick upper layer of sample 4 varying with E2

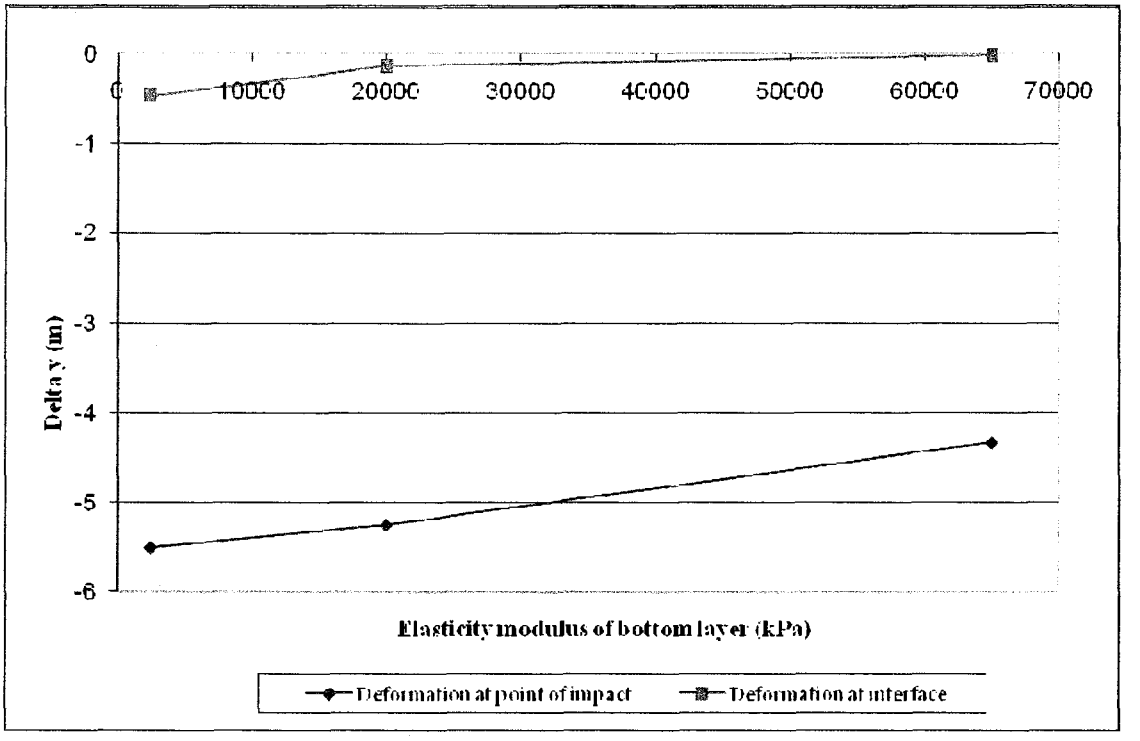

Figure 4.67: Δy of 2 m thick upper layer of sample 4 varying with E2

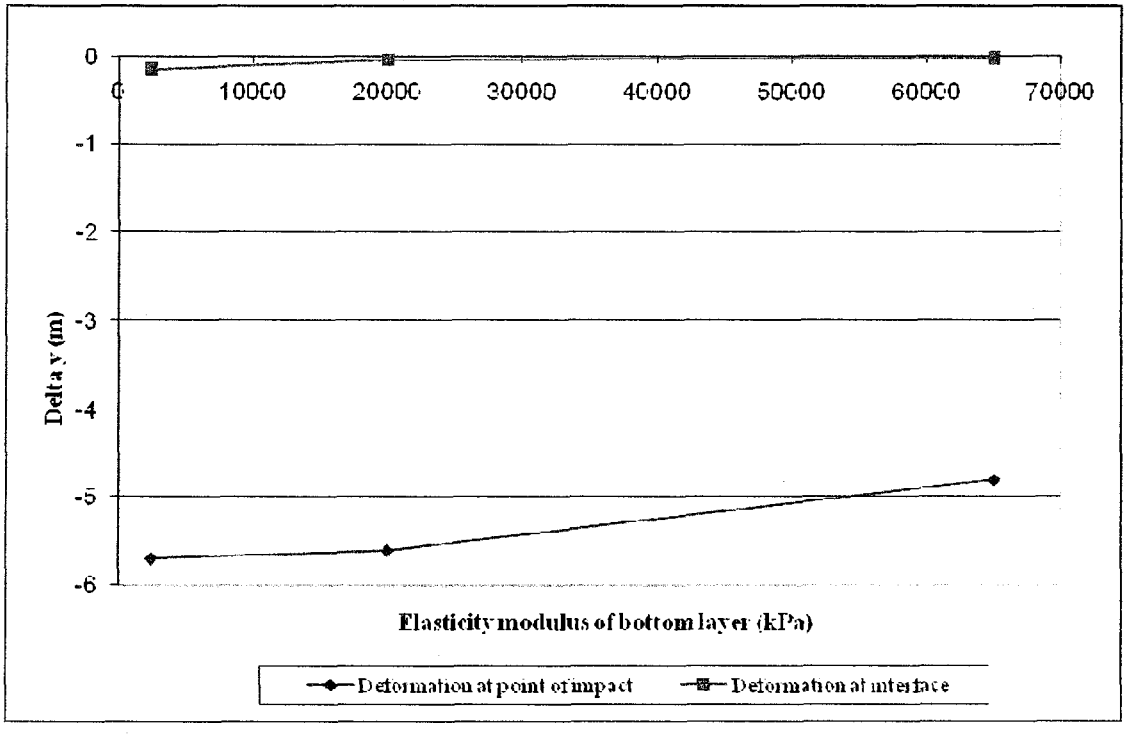

Figure 4.68: Δy of 3 m thick upper layer of sample 4 varying with E2

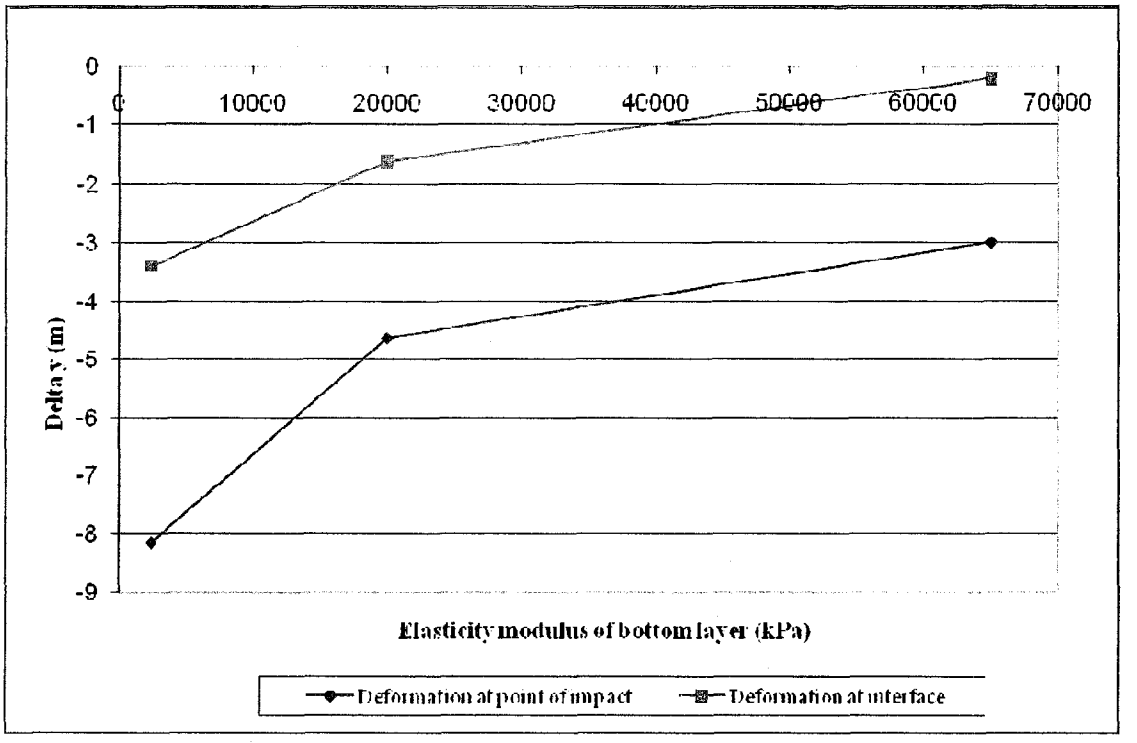

Figure 4.69: Δy of 1 m thick upper layer of sample 5 varying with E2

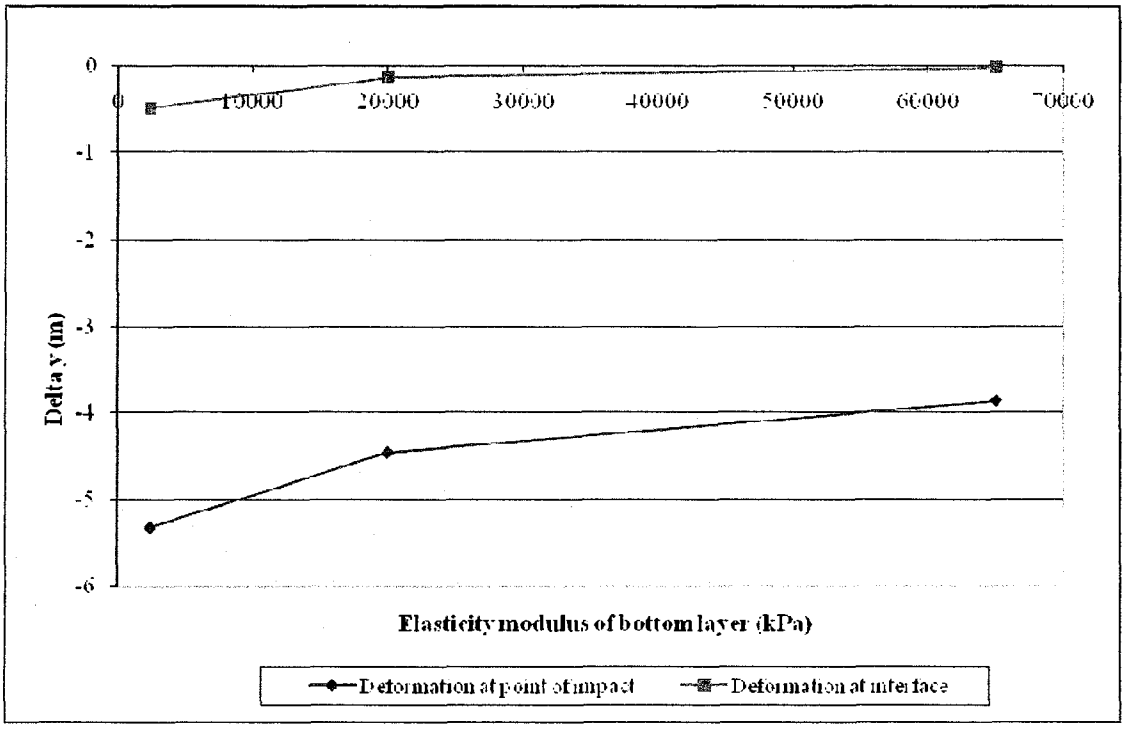

Figure 4.70: Δy of 2 m thick upper layer of sample 5 varying with E2

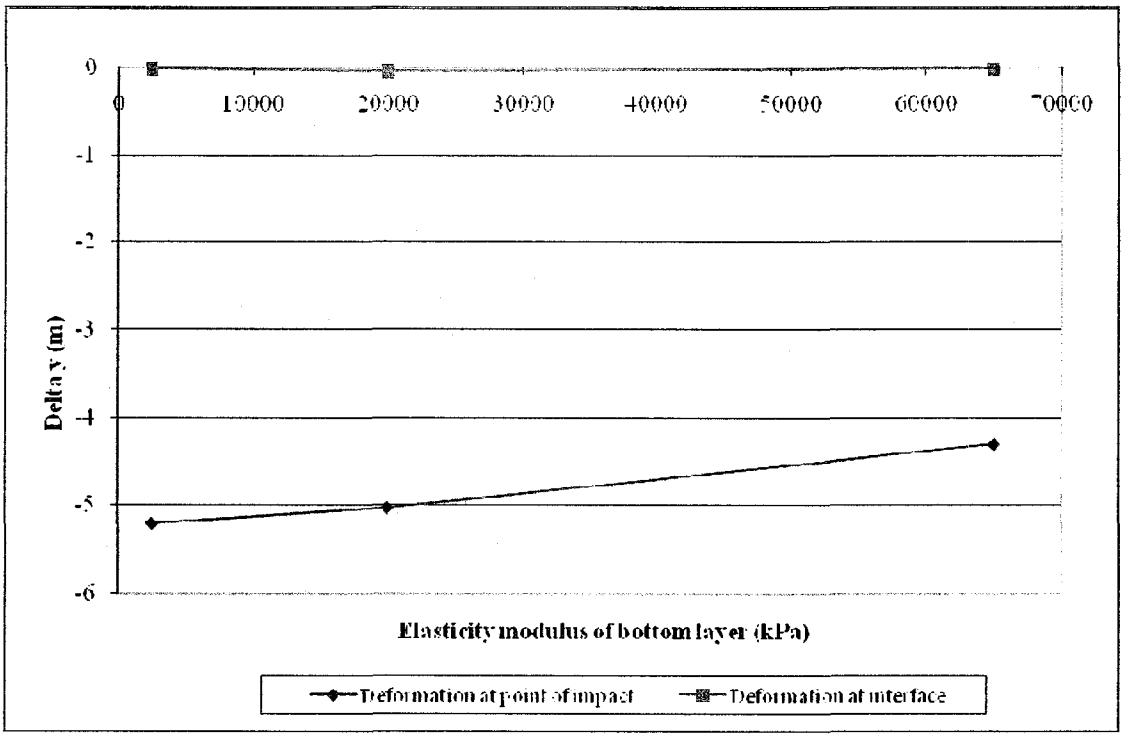

Figure 4.71: Δy of 3 m thick upper layer of sample 5 varying with E2

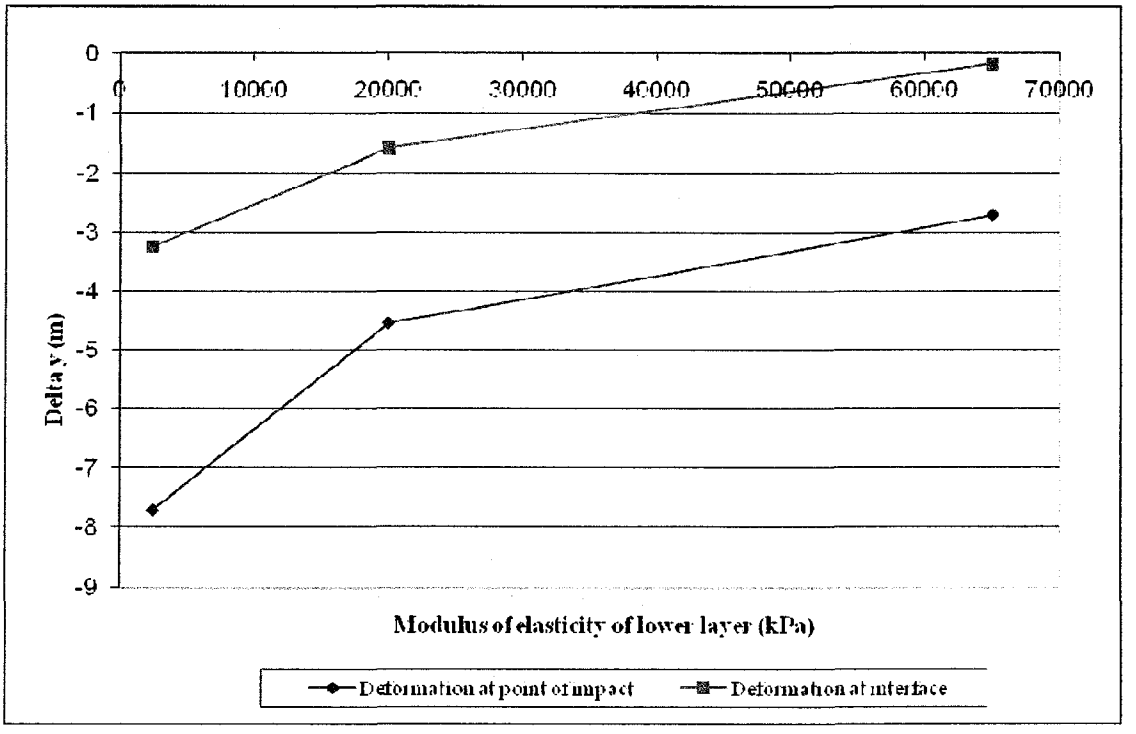

Figure 4.72: Δy of 1 m thick upper layer of sample 6 varying with E2

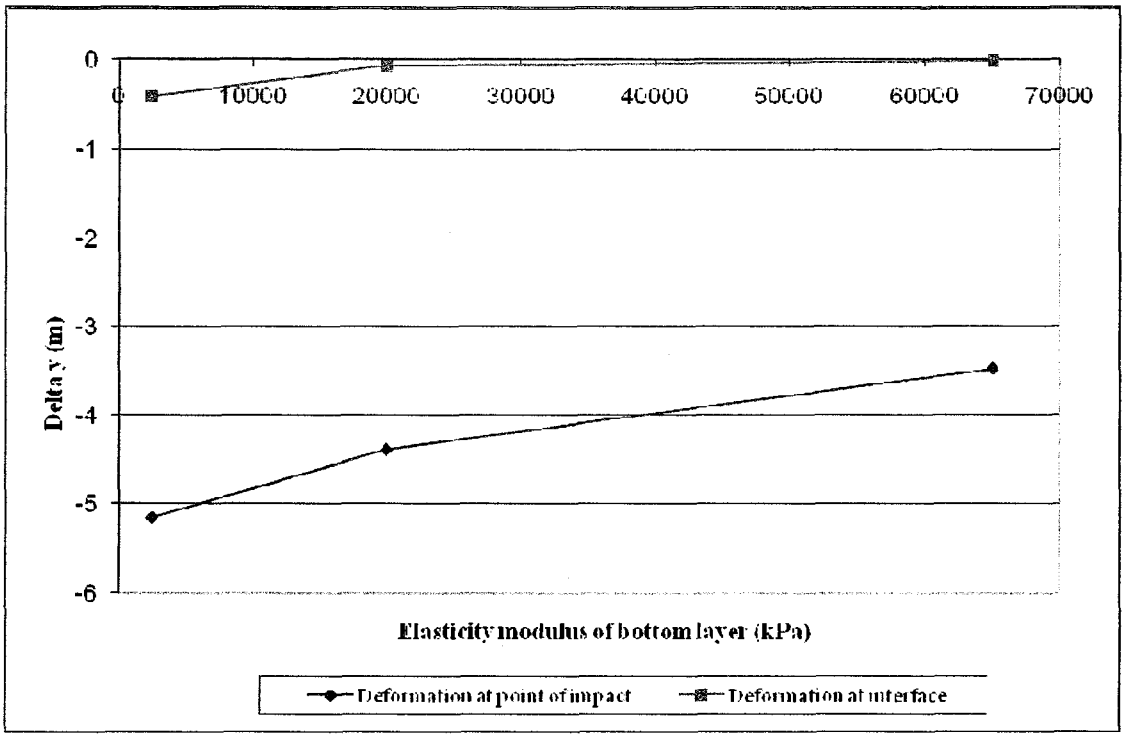

Figure 4.73: Δy of 2 m thick upper layer of sample 6 varying with E2

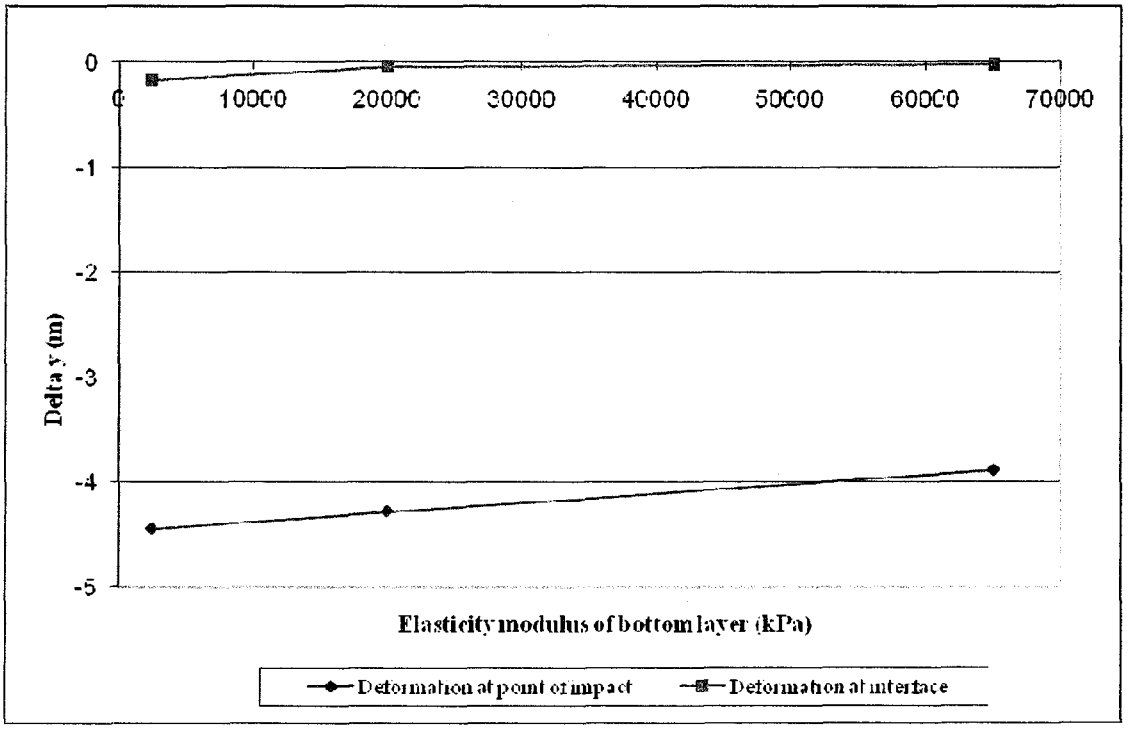

Figure 4.74: Δy of 3 m thick upper layer of sample 6 varying with E2

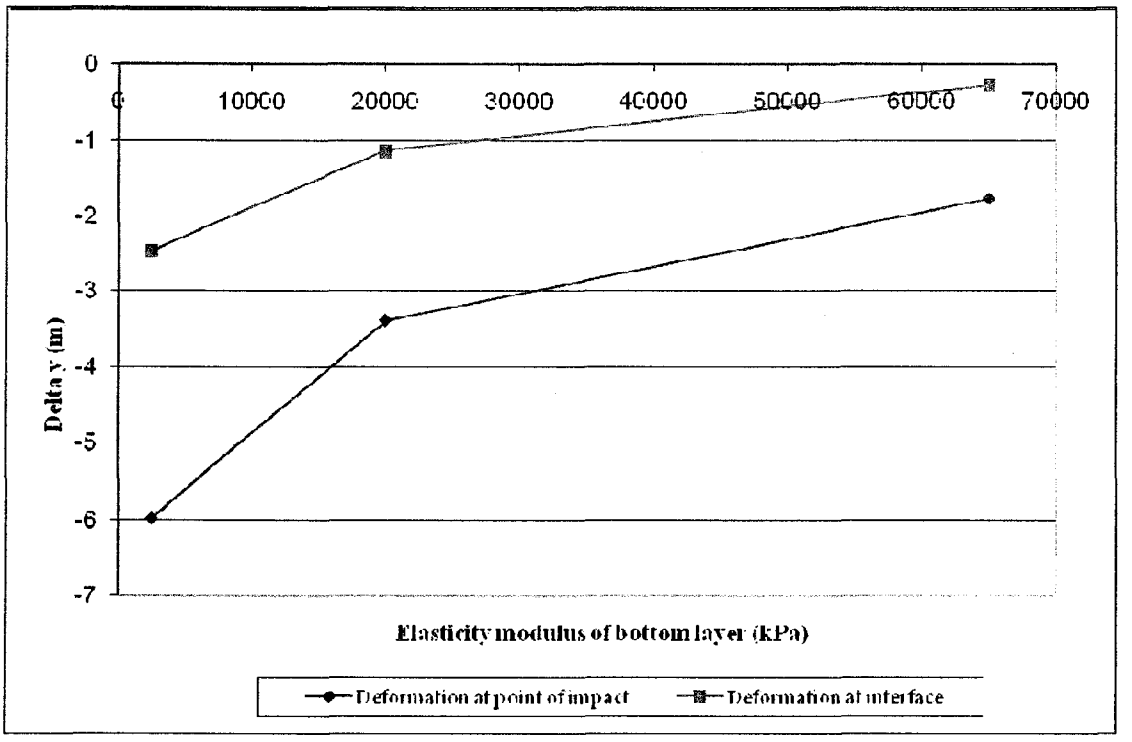

Figure 4.75: Δy of 1 m thick upper layer of sample 7 varying with E2

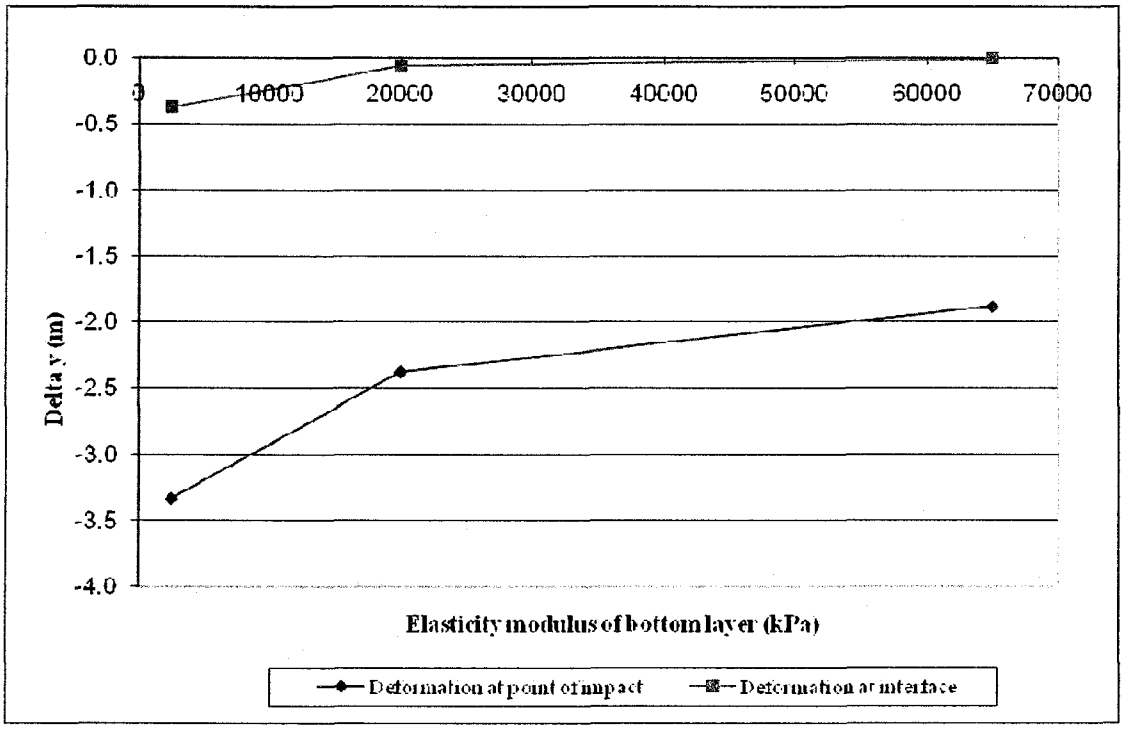

Figure 4.76: Δy of 2 m thick upper layer of sample 7 varying with E2

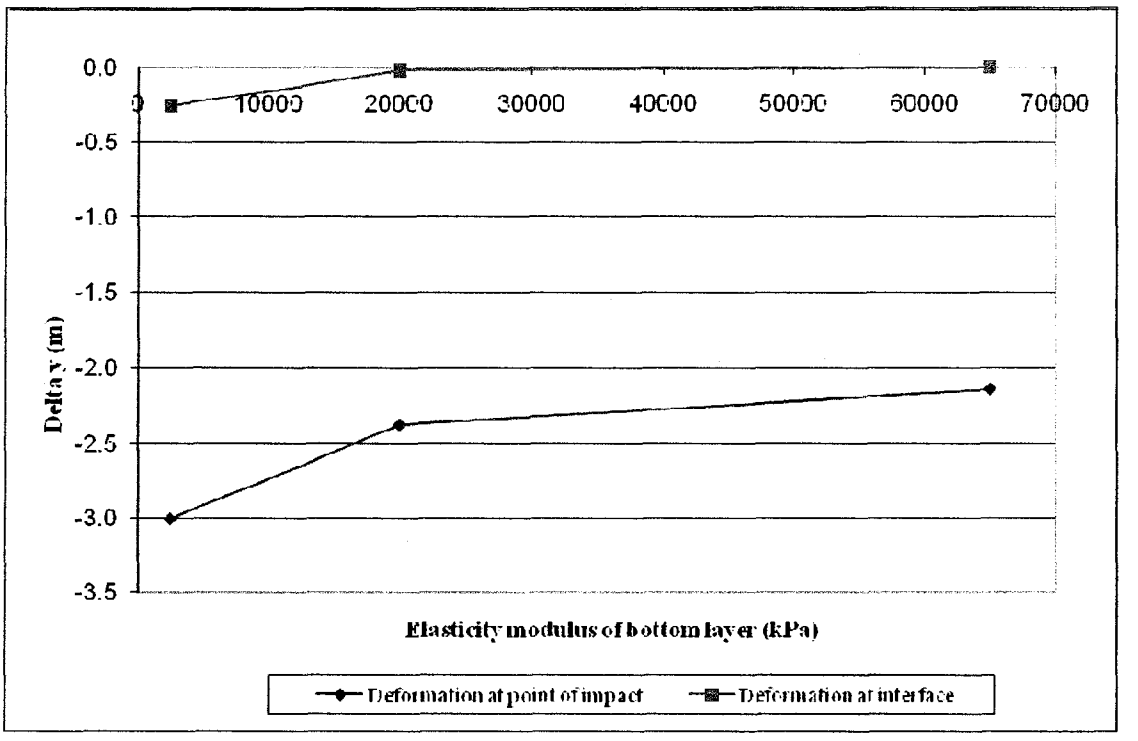

Figure 4.77: Δy of 3 m thick upper layer of sample 7 varying with E2

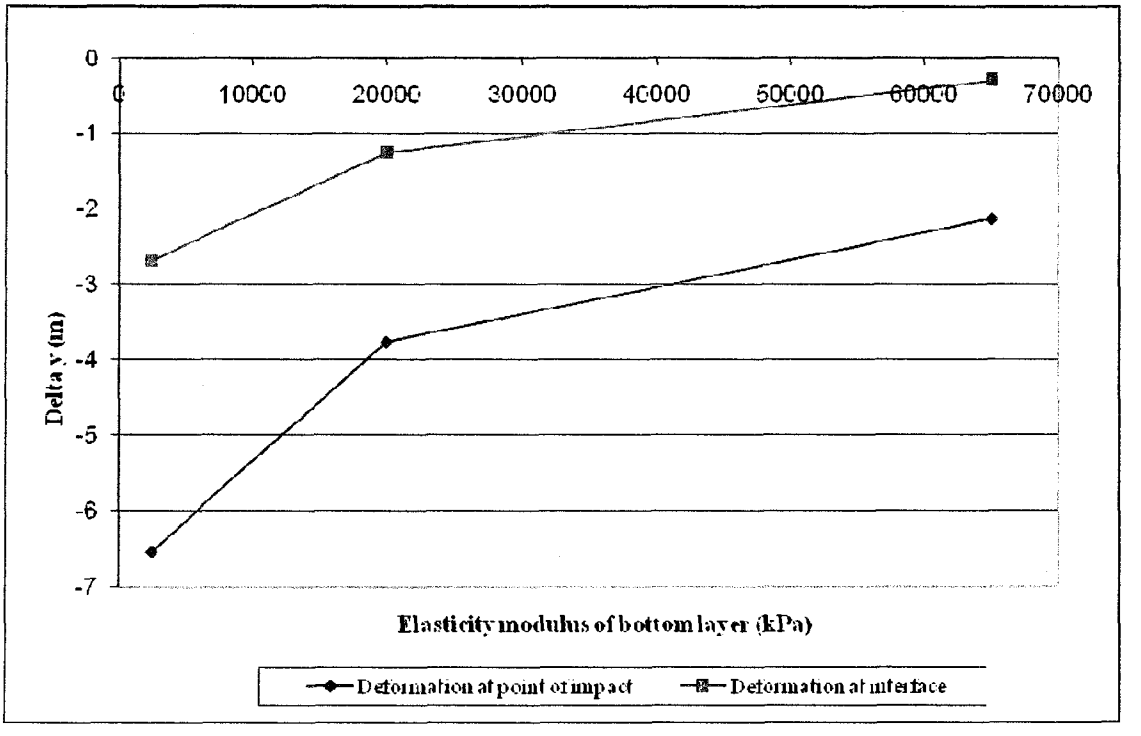

Figure 4.78: Δy of 1 m thick upper layer of sample 8 varying with E2

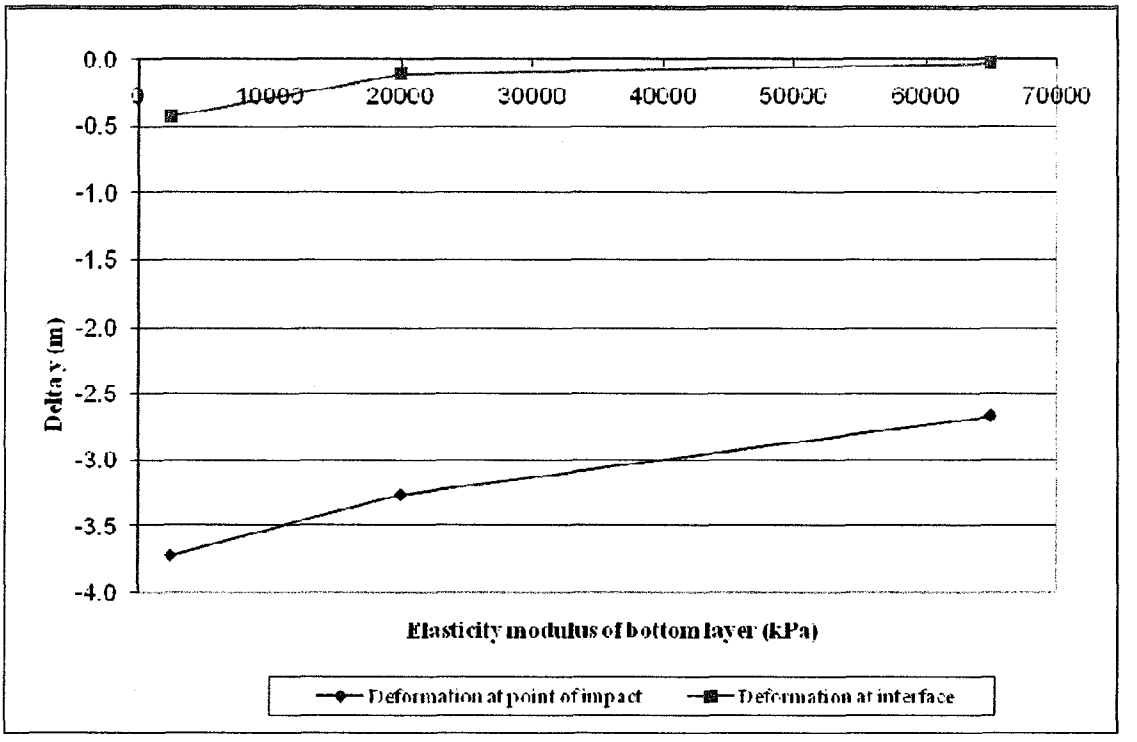

Figure 4.79: Δy of 2 m thick upper layer of sample 8 varying with E2

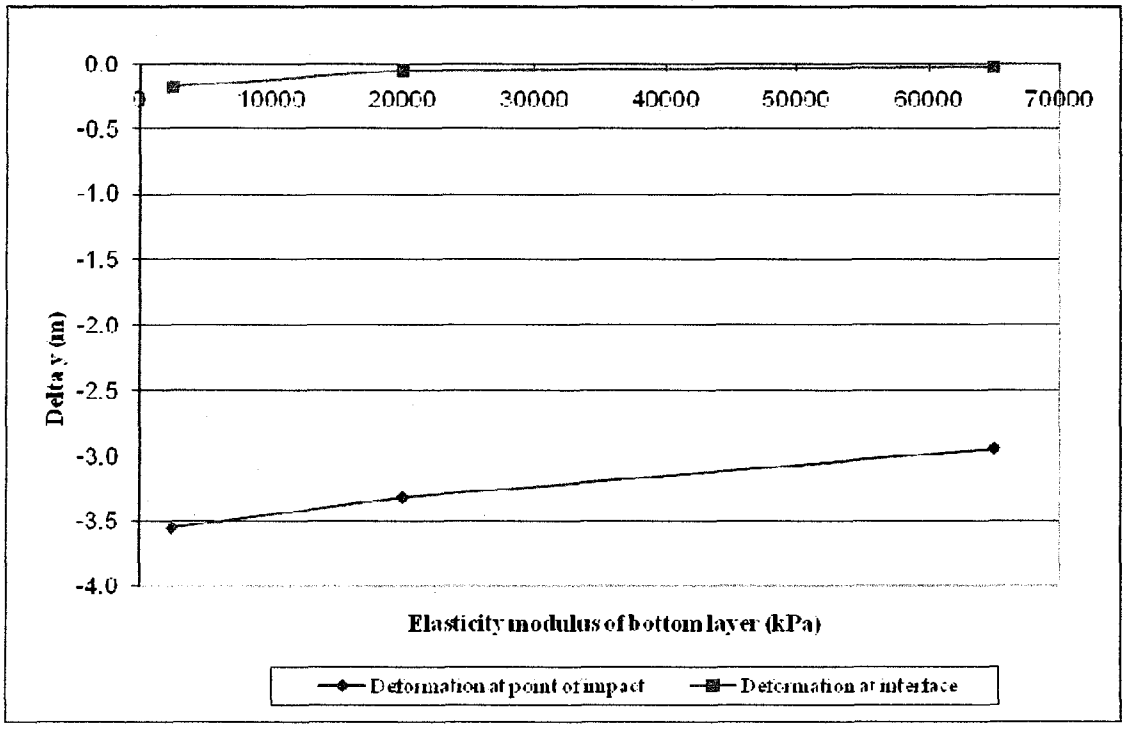

Figure 4.80: Δy of 3 m thick upper layer of sample 8 varying with E2

4.11 ANALYSIS OF TEST RESULTS - SUBGRADE LAYER OVERLYING DEEP DEPOSIT

There are two trends which can be observed from the figures plotted with the resulting data of the field case with upper layer thickness ranging from 1 to 3 m. First, from Figures 4.33 to 4.56, it is observed that as the upper layer thickness increases, the upper layer's deformation increases, therefore decreasing the upper layer's compaction. Second, it can be seen from figures 4.57 to 4.80 that the compaction of the upper layer increases with increasing modulus of elasticity of the lower layer.

As it is once again of interest to determine whether or not the underlying layer has had any effect with respect to the compaction of the upper layer, it is necessary to determine the actual deformation exhibited by the upper layer, which are summarized in Tables 4.16 to 4.18. That is, the vertical deformation of the upper layer without accounting for the movement of the lower layer. Therefore, the vertical deformation of the interface was subtracted from that of the point of impact for comparison purposes. The results for the laterally confined model and the field model are respectively presented in the following tables:

Table 4.11: Actual vertical deformation at point of impact for field model with upper layer thickness of 1 m

Sample number	Actual vertical deformation at point of impact (m)		
	E2 = 2500 kPa	E2 = 20 000 kPa	E2 = 65 000
1	-5.503861	-3.790492	-3.733880
2	-5.503861	-3.790492	-3.733880
3	-3.050696	-1.679222	-1.150180
4	-4.883216	-3.451328	-3.326743
5	-4.766541	-3.017204	-2.772233
6	-4.481292	-2.958694	-2.508122
7	-3.506628	-2.257970	-1.507818
8	-3.848908	-2.520786	-1.848730

Table 4.12: Actual vertical deformation at point of impact for field model with upper layer thickness of 2 m

Sample number	Actual vertical deformation at point of impact (m)		
	E2 = 2500 kPa	E2 = 20 000 kPa	E2 = 65 000
1	-5.863889	-5.693238	-5.202517
2	-5.863889	-5.693238	-5.202517
3	-2.422457	-2.038129	-1.721967
4	-5.054650	-5.119378	-4.302273
5	-4.847133	-4.337692	-3.839153
6	-4.739489	-4.314544	-3.462809
7	-2.959739	-2.317150	-1.874553
8	-3.296475	-3.159815	-2.631962

Table 4.13: Actual vertical deformation at point of impact for field model with upper layer thickness of 3 m

Sample number	Actual vertical deformation at point of impact (m)		
	E2 = 2500 kPa	E2 = 20 000 kPa	E2 = 65 000
1	-6.182381	-6.242561	-5.773279
2	-6.182381	-6.242561	-5.773279
3	-2.393489	-2.103720	-1.888607
4	-5.548728	-5.571876	-4.784906
5	-5.185683	-4.985096	-4.279820
6	-4.276787	-4.237786	-3.868323
7	-2.746452	-2.347230	-2.132015
8	-3.374101	-3.269968	-2.916979

In order to calculate meaningful percentage differences, it was necessary to obtain the vertical deformation at the point of impact of a homogenous layer (upper layer) 25 m in width and depth, the results of which are summarized here below.

Table 4.14: Vertical deformation for maximum unit weight using homogenous field model

Sample number	Δy (m)
1	-7.514790
2	-7.514790
3	-1.971714
4	-4.912799
5	-4.518337
6	-4.113139
7	-2.238087
8	-2.884109

It was necessary to obtain these deformations in order to be able to compare the field deformations to these values, rather than the Proctor model deformations, which were proven earlier to not be valid for a field case. As before, a positive percentage greater than zero indicates that applied energy was lost to the underlying layer, whereas a negative one indicates that some of the energy was reflected back into the upper layer, further compacting it. If there is no difference (0%), this means that the upper layer was compacted exactly as in the homogenous field model. Tables 4.20 to 4.22 present the results obtained.

Table 4.15: Percentage difference of actual vertical deformations for the field model with upper layer = 1 m

Sample number	% difference between Proctor and laterally confined model vertical deformation results		
	E2 = 2500 kPa	E2 = 20 000 kPa	E2 = 65 000
1	-26.8	-49.6	-50.3
2	-26.8	-49.6	-50.3
3	54.7	-14.8	-41.7
4	-0.6	-29.7	-32.3
5	5.5	-33.2	-38.6
6	9.0	-28.1	-39.0
7	56.7	0.9	-32.6
8	33.5	-12.6	-35.9

The percentage differences obtained in Table 4.20 indicate that as the modulus of elasticity of the lower layer increases, so does the compaction of the upper layer. It is even seen for samples 1, 2 and 4 that the upper layer is compacted beyond the Proctor deformation for all three values of the elasticity modulus of the lower layer.

Table 4.16: Percentage difference of actual vertical deformations for the field model with upper layer = 2 m

Sample number	% difference between Proctor and laterally confined model vertical deformation results		
	E2 = 2500 kPa	E2 = 20 000 kPa	E2 = 65 000
1	-22.0	-24.2	-30.8
2	-22.0	-24.2	-30.8
3	22.9	3.4	-12.7
4	2.9	4.2	-12.4
5	7.3	-4.0	-15.0
6	15.2	4.9	-15.8
7	32.2	3.5	-16.2
8	14.3	9.6	-8.7

Table 4.17: Percentage difference of actual vertical deformations for the field model with upper layer = 3 m

Sample number	% difference between Proctor and laterally confined model vertical deformation results		
	E2 = 2500 kPa	E2 = 20 000 kPa	E2 = 65 000
1	-17.7	-50.3	-23.2
2	-17.7	-50.3	-23.2
3	21.4	-41.7	-4.2
4	12.9	-32.3	-2.6
5	14.8	-38.6	-5.3
6	4.0	-39.0	-6.0
7	22.7	-32.6	-4.7
8	17.0	-35.9	1.1

The results from tables 4.20 to 4.22 are depicted graphically in figures 4.81 to 4.83, where the percentage difference is plotted against increasing elasticity modulus of the lower layer for an upper layer of the same thickness for each sample.

Figures 4.84 to 4.86 present the percentage difference plotted against increasing thickness of the upper layer of each sample for each modulus of elasticity of the lower layer.

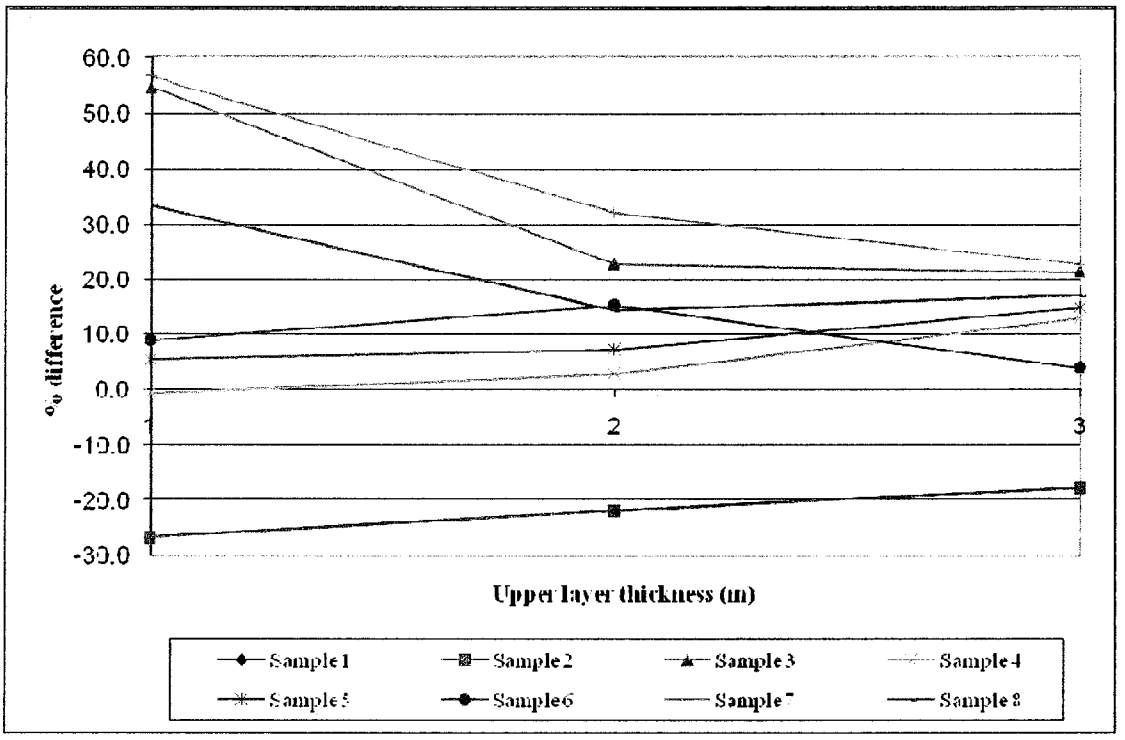

Figure 4.81: % difference vs upper layer thickness with E2 = 2500 kPa

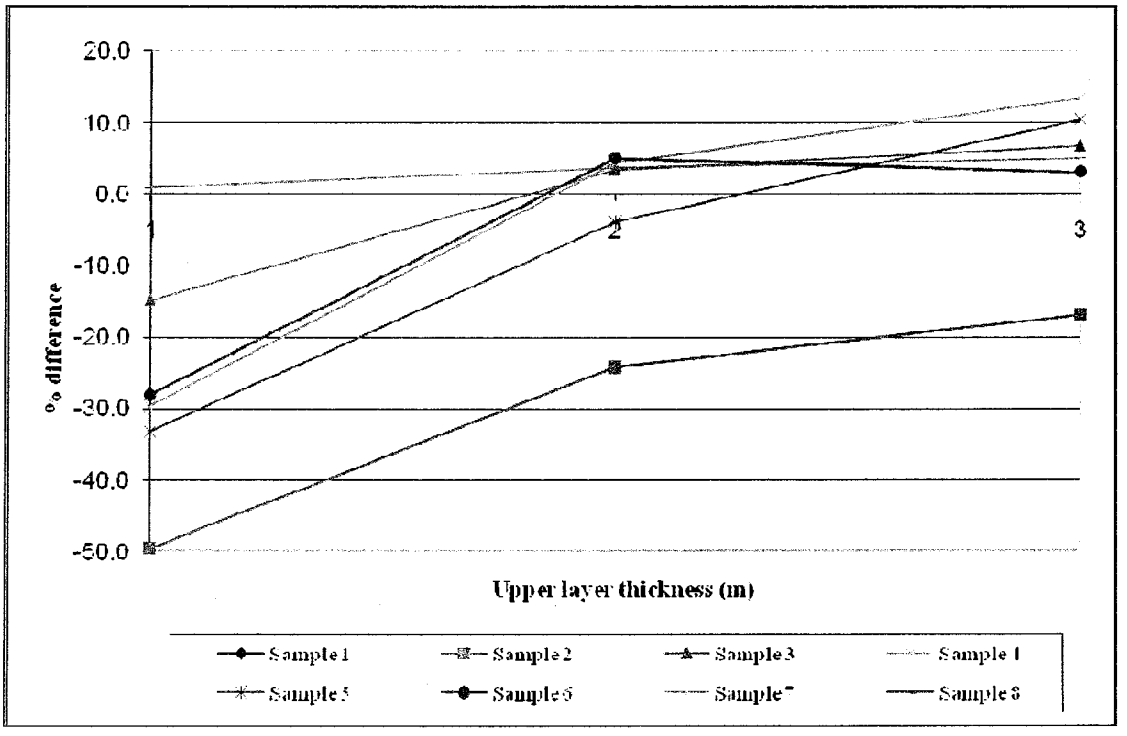

Figure 4.82: % difference vs upper layer thickness with E2 = 20000 kPa

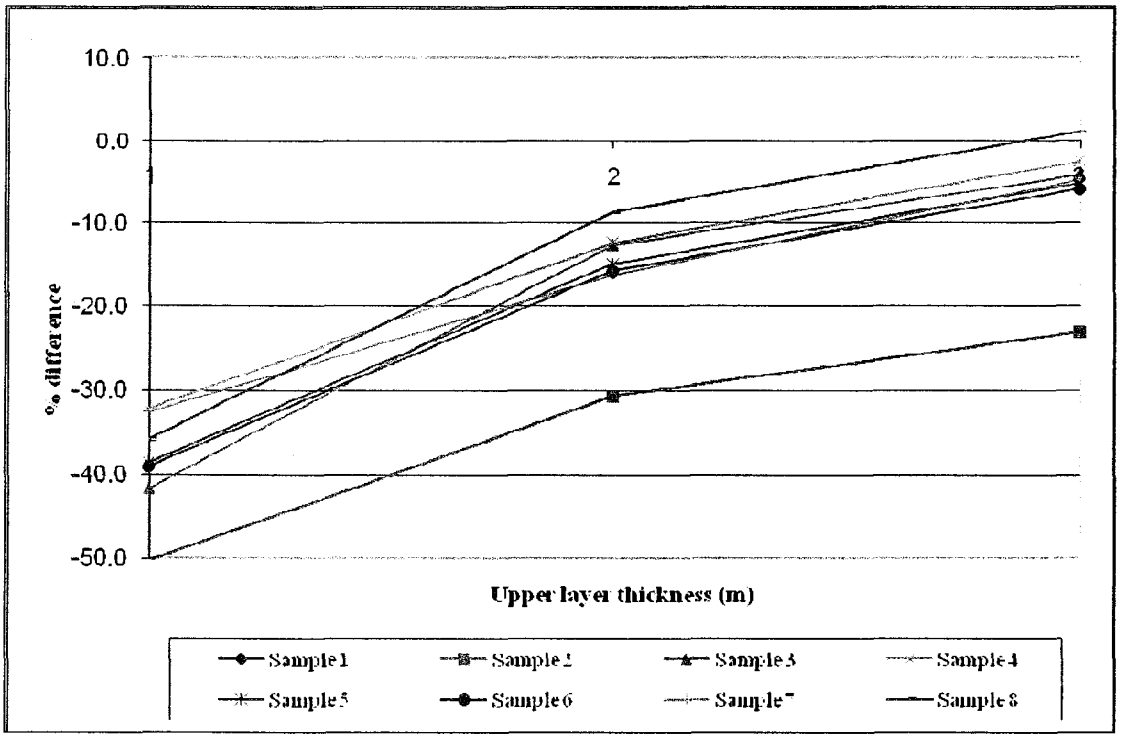

Figure 4.83: % difference versus upper layer thickness with E2 = 65000 kPa

From figure 4.81 it can be seen that samples 3, 7 and 8 increase in compaction as the layer thickness increases when the lower layer has a modulus of elasticity of 2 500 kPa, whereas the remainder of the samples decrease in compaction with increasing thickness. It should be noted that the samples 3, 7 and 8 each have high elasticity moduli (15 000, 10 666.7 and 9 500 kPa respectively) compared to the underlying layer and also they are the only samples having a Poisson's ratio of 0.3, which would account for the different response of these samples.

However, once the underlying layer's elasticity modulus exceeds that of the upper layer, as seen in figures 4.82 and 4.83 for E2 = 20 000 and 65 000 kPa respectively, only decreasing compaction with increasing layer thickness is observed.

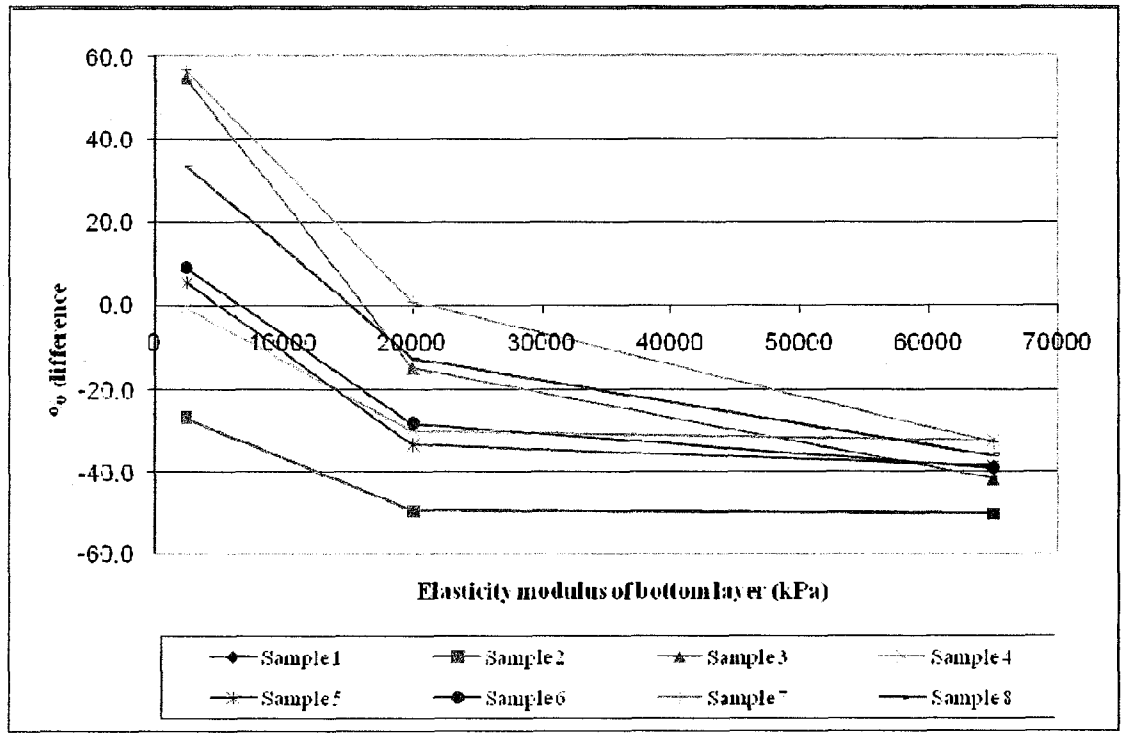

Figure 4.84: % difference vs E2 for 1 m thick upper layer

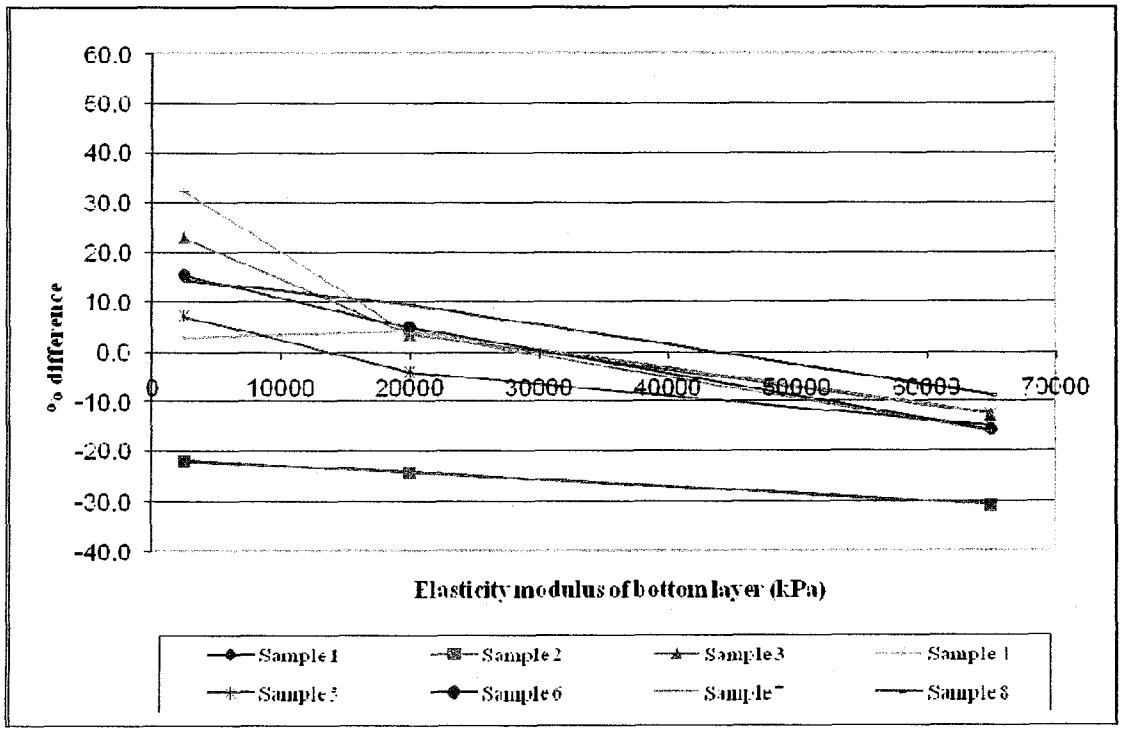

Figure 4.85: % difference vs E2 for 2 m thick upper layer

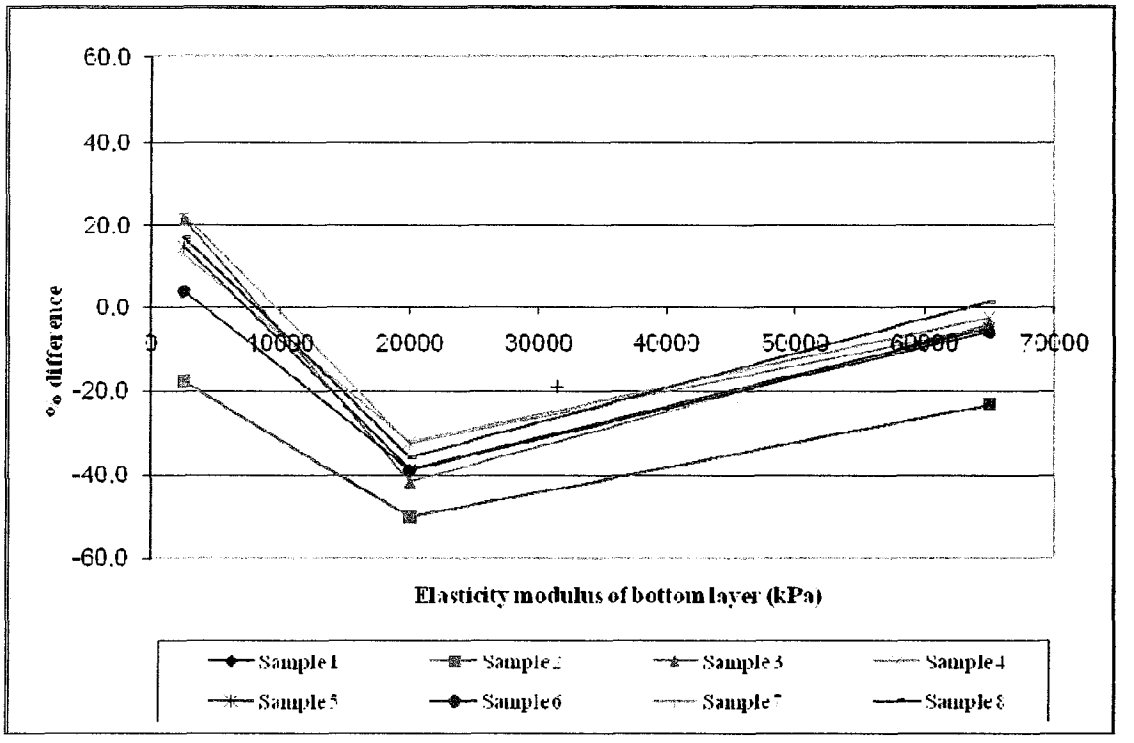

Figure 4.86: % difference vs E2 for 3 m thick upper layer

It is shown in figures 4.84 and 4.85 that compaction of the upper layer increases as the elasticity modulus of the lower layer increases for upper layer thicknesses of 1 and 2 m. This is not the case when the upper layer is 3 m thick, as seen in figure 4.86. Compaction of the upper layer increases initially from a value of E2 of 2 500 to 20 000 kPa and then decreases as the strength of the lower layer reaches 65 000 kPa.

Therefore, a trend of increasing compaction of the upper layer with increasing modulus of elasticity of the lower layer was observed for upper layer thickness ranging from 1 to 2 m. This did not hold true once the upper layer thickness reached 3 m with an elasticity modulus of the lower layer of 65 000 kPa.

4.12 DESIGN GUIDELINES

Figure 4.87 depicts the vertical deformation obtained for the Proctor model and for the homogenous soil field model for all eight tested samples.

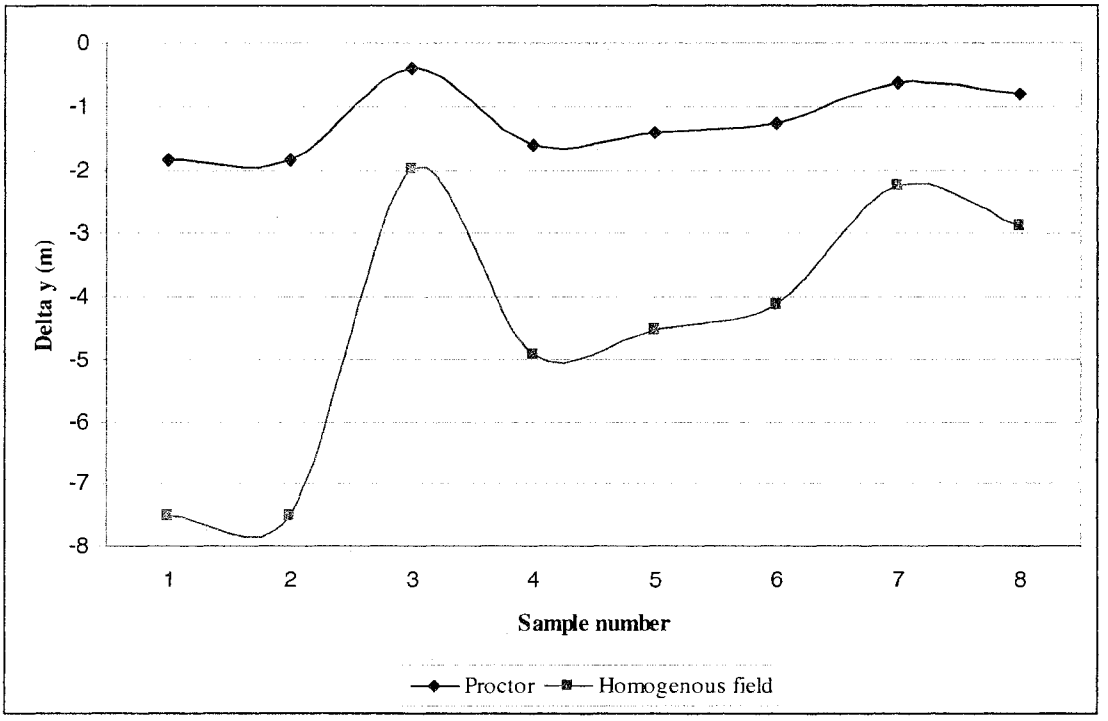

Figure 4.87: Δy of Proctor and homogenous field models

The differences in the observed vertical deformations of each sample from this figure are due to the incompatibility of the Proctor test's boundaries with those of the field. That is, a Proctor test sample is confined both laterally and horizontally, whereas a field sample is free to move in three dimensions.

Given that the results obtained via a Proctor test are unreliable to predict field compaction, the following design charts (figures 4.88 to 4.95) were created in order to predict the level of compaction for a given soil configuration. Given the initial stiffness (modulus of elasticity) of the underlying deep deposit and the thickness of the upper layer, provided that the upper layer is at the optimum moisture content, the maximum compaction for of the upper layer (represented by the vertical deformation) can be determined.

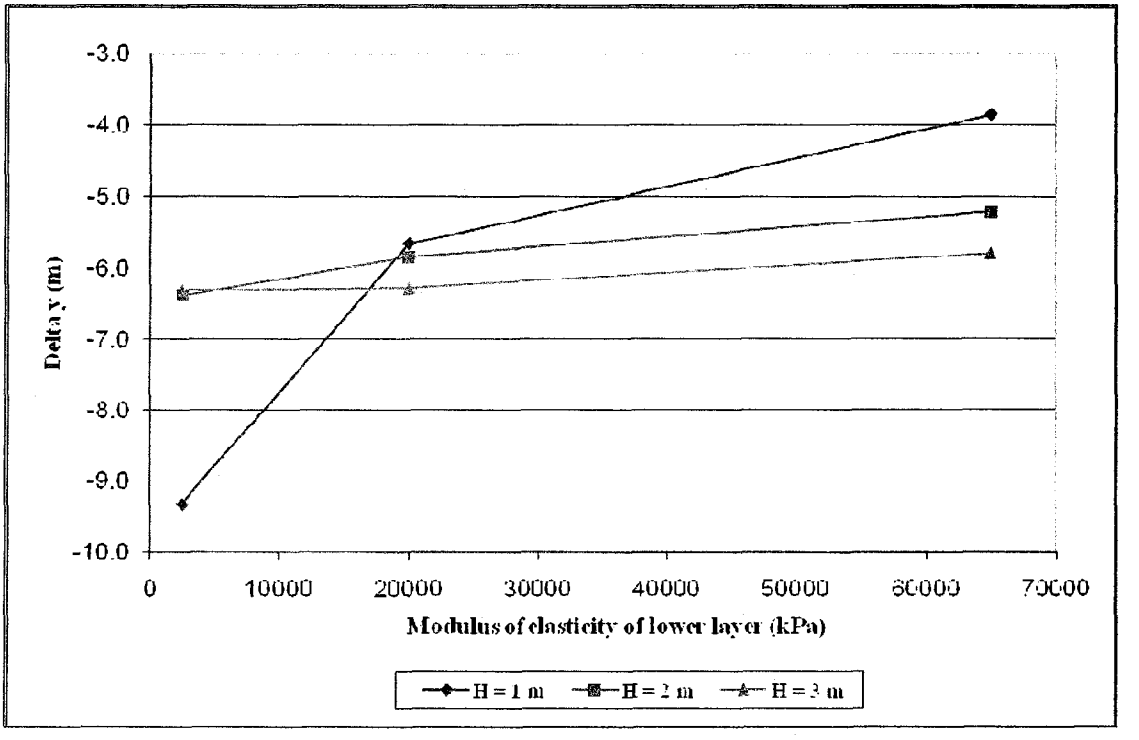

Figure 4.88: Design chart for γ_{dry}=16.2 kN/m^3

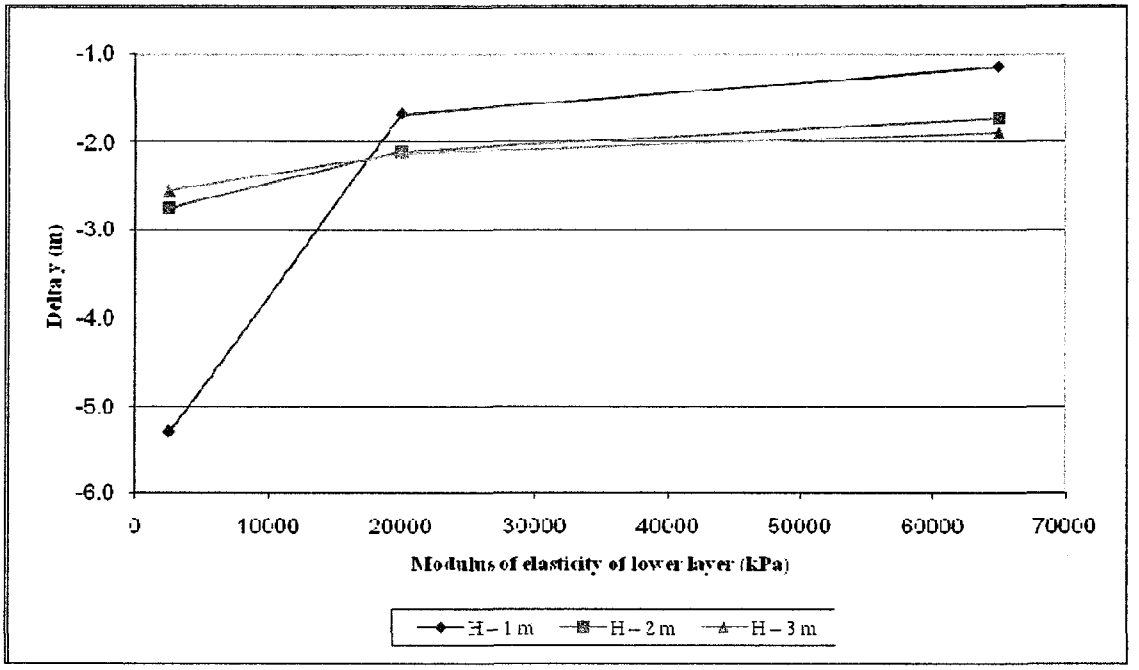

Figure 4.89: Design chart for γ_{dry}=16.4 kN/m^3

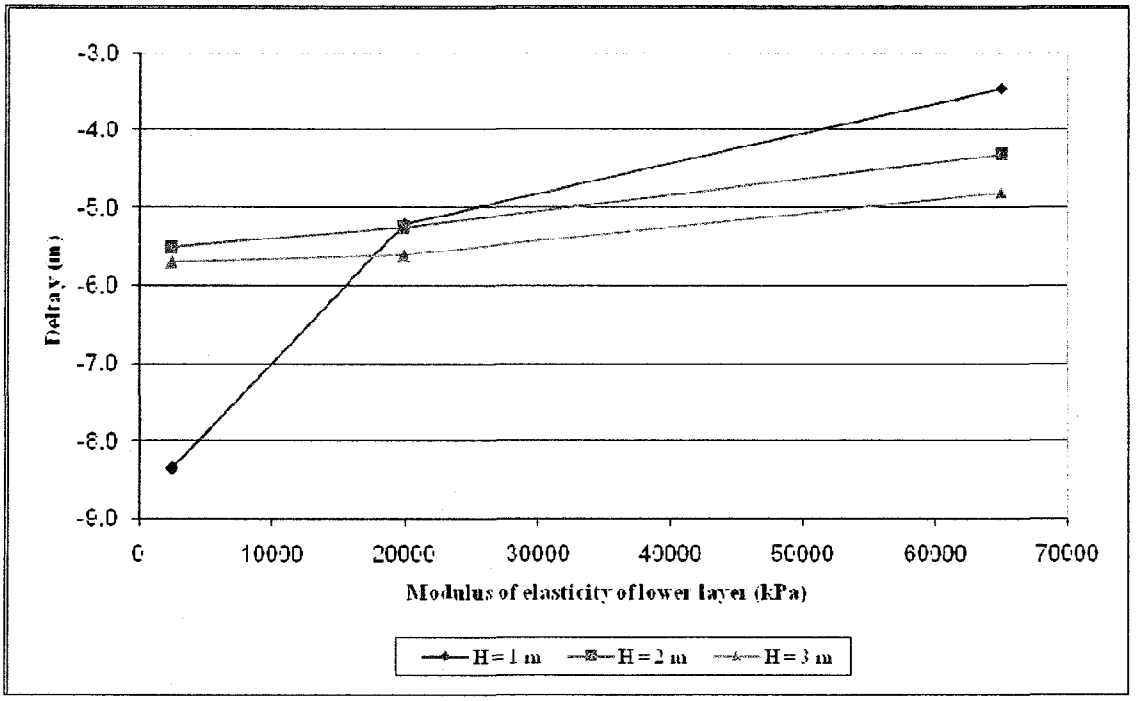

Figure 4.90: Design chart for γ_{dry}=16.5 kN/m^3

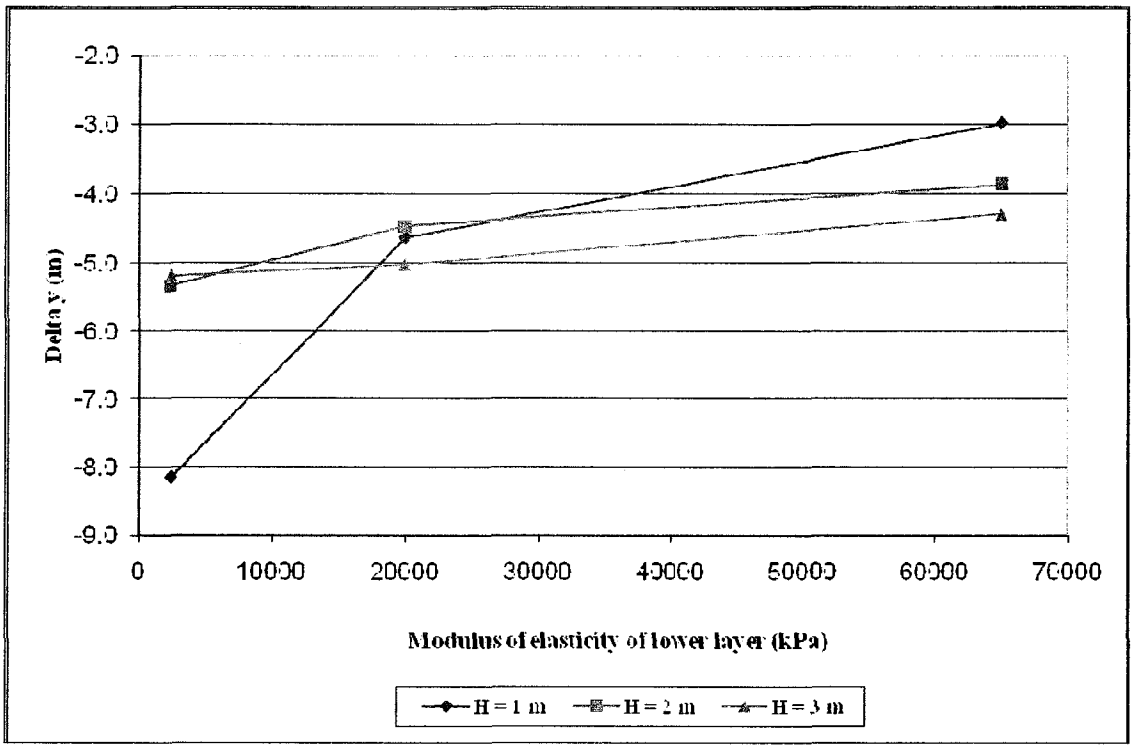

Figure 4.91: Design chart for γ_{dry}=16.8 kN/m^3

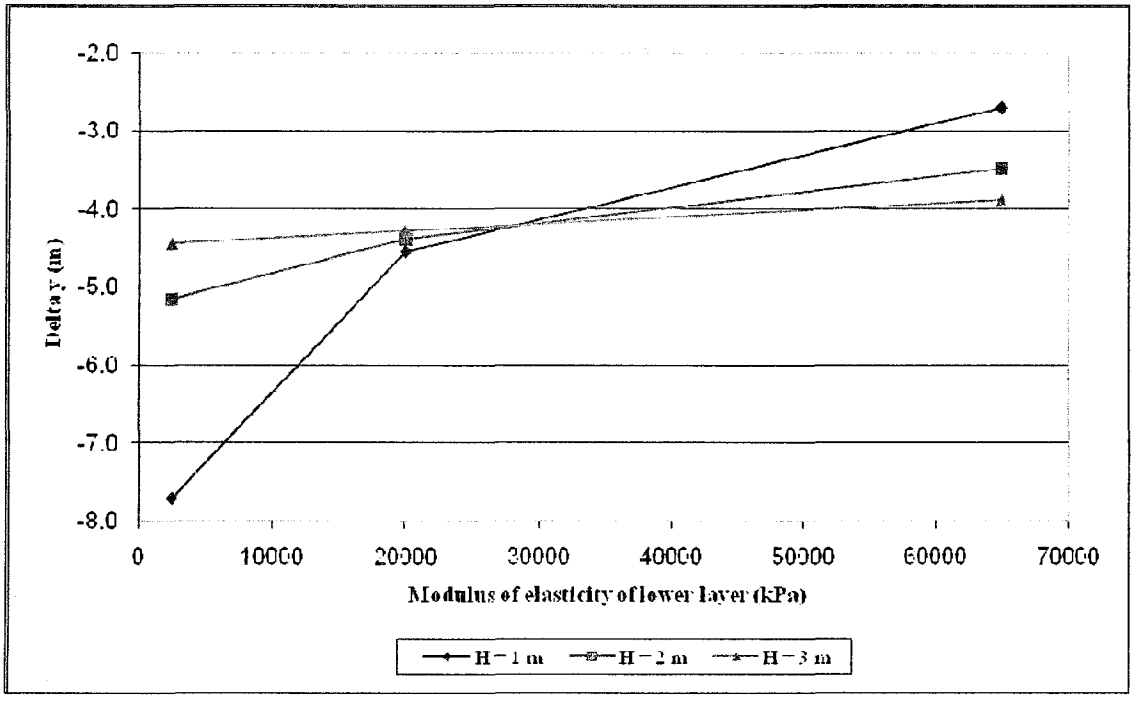

Figure 4.92: Design chart for γ_{dry}=17.1 kN/m^3

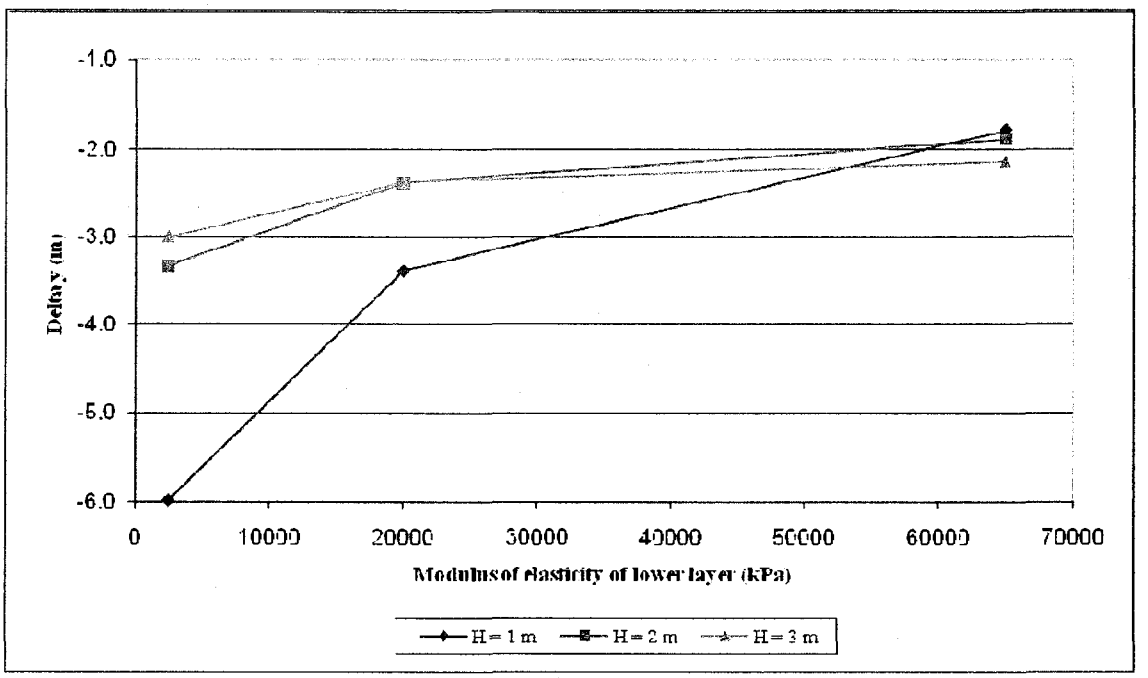

Figure 4.93: Design chart for γ_{dry}=17.3 kN/m^3

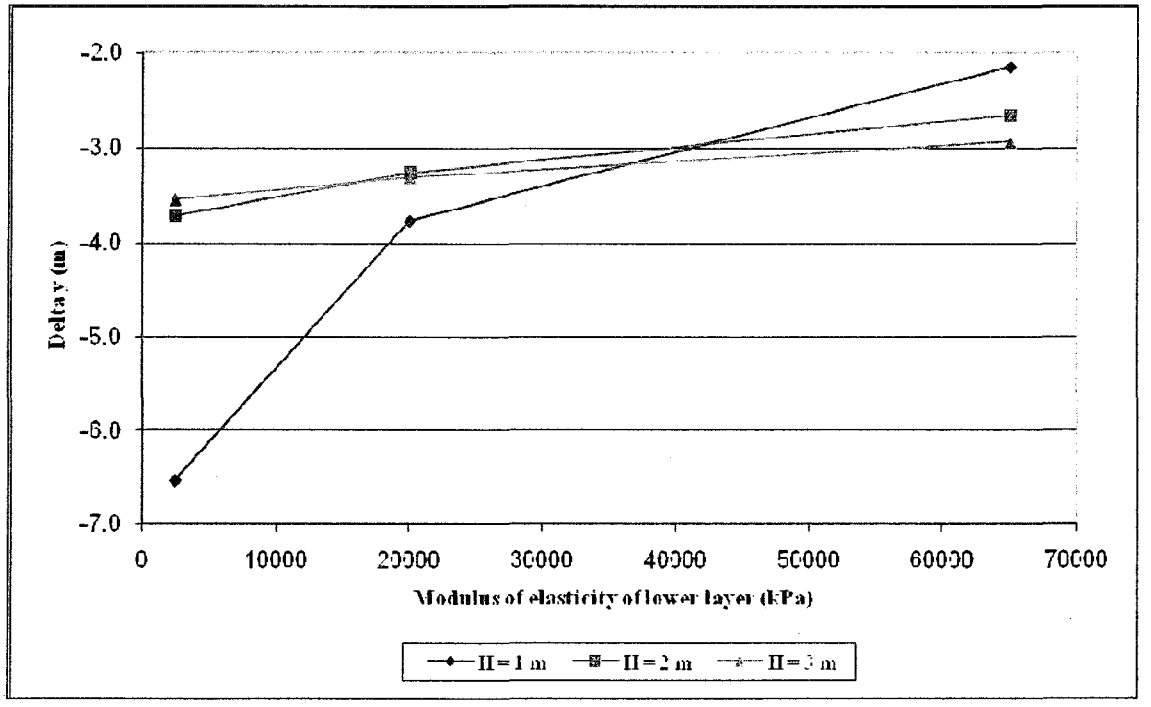

Figure 4.94: Design chart for γ_{dry}=17.7 kN/m^3

4.13 EXAMPLE USING THE DESIGN GUIDELINES

The following section will present a step by step example of how to use the design guidelines.

Design Example

Given:

- H = 1.5 m
- E2 = 35 000 kPa
- Dynamic load Q = 2 700 kN/m^2

Determine the field compaction.

The Proctor test results are as follows:

- Optimum moisture content = 14.3 %
- Maximum dry unit weight = 16.45 kN/m^3.

Looking at all the available design charts, it is found that the dry unit weight value falls between those of figures 4.89 and 4.90 (γ_{dry}=16.4 and 16.5 kN/m^3 respectively). In order to find the corresponding vertical deformation, some extrapolations will be necessary. The following steps outline the procedure to be followed in order to determine the expected vertical deformation in the field.

1. Using figure 4.89, 35 000 kPa is located on the horizontal axis and the corresponding vertical deformation values are taken at the lines for H = 1 and 2 m respectively (as shown in figure 4.95).

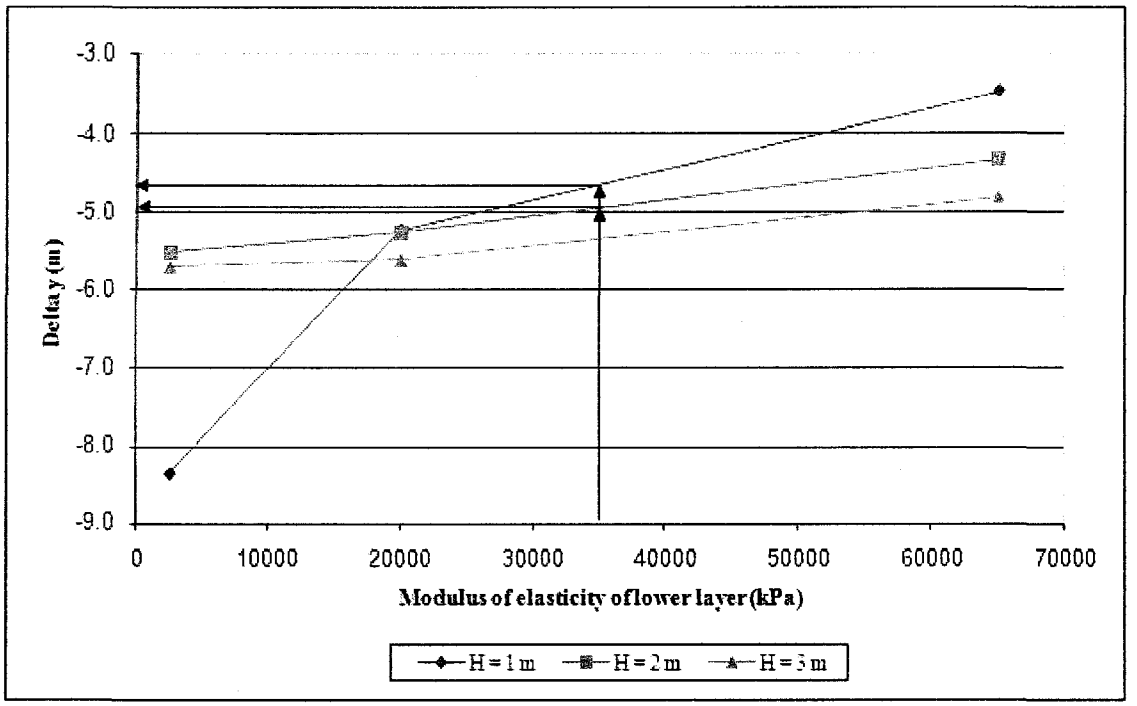

Figure 4.95: Delta y corresponding to E2 = 35 000 kPa

2. The resulting values are of -4.6 m and -4.95 m corresponding to a thickness of 1 and 2 m respectively.
3. In the same manner, the above is repeated using figure 4.90.
4. The resulting values are of -4.1 m and -4.3 m corresponding to a thickness of 1 and 2 m respectively.
5. In order to obtain the vertical deformations corresponding to γ_{dry}= 16.5 kN/m^3, the average of the values obtained from each figure is calculated for each thickness as follows:

   For H = 1 m:

$$\frac{-4.6+(-4.1)}{2} = -4.35m$$

For H = 2 m:

$$\frac{-4.95+(-4.3)}{2} = -4.625m$$

6. Extrapolating for a value of 1.5 m thickness the following results are obtained:

$$\left\{\frac{-4.625-(-4.35)}{(2-1)}\times(1.5-1)\right\}+(-4.15) = -4.2875m$$

Therefore, for a 1.5 m thick layer having a maximum dry unit weight of 16.45 kN/m^3 overlying a deep deposit with a stiffness of 35 000 kPa, a vertical field deformation of -4.29 m is expected. This value includes the settlement of the underlying layer as experienced by the subgrade layer.

CHAPTER 5

CONCLUSION AND RECOMMENDATIONS

5.1 GENERAL

Field compaction is often based on laboratory Proctor test results. Wide discrepancies are frequently observed between the laboratory results and the field results. The present investigation was directed at developing a numerical model capable of examining the field and laboratory boundary conditions which are responsible for the results obtained. The following can be concluded:

1. The Proctor test is not representative of field compaction conditions. The boundary conditions of the laboratory Proctor test are not compatible with those of field conditions. This is due to the sample in the Proctor test being confined both laterally and horizontally, whereas field samples are free to move in three dimensions.
2. Lateral boundaries have little effect on the produced level of compaction, whereas the bottom horizontal boundary has a major significant effect when replaced with an underlying layer. As energy waves reach the interface between the 2 layers, some energy is absorbed by the lower layer and some is reflected back into the upper layer. The highest degree of compaction is achieved when all of the energy is reflected back into the upper layer (upper boundary). Accordingly, the lowest level of compaction is achieved when all of the applied energy is absorbed by the lower layer (lower boundary).

3. The parameters governing the compaction of a thin subgrade layer at the modified Proctor energy level are the stiffness of the lower layer and the thickness and stiffness of the subgrade layer.
4. Compaction of the upper layer increases with increasing lower layer stiffness and decreases as its thickness increases.
5. The level of compaction obtained in the upper layer is a function of the energy lost to the lower layer. Therefore, the less energy lost to the lower layer, the higher the degree of compaction achieved.

Based on the results of the present investigation, the following are recommended: in order to avoid the negative effects of poor compaction in the field prior to the field compaction work:

1. A weak lower layer can be improved by means of injection.
2. Reinforcement can be added between the two layers by installing a geotextile or geomembrane at the interface of the two layers.
3. A portion of a weak lower layer can be excavated and replaced by a material with a higher stiffness and/or bearing capacity.

The above will sensibly improve the compaction of the upper layer.

5.2 RECOMMENDATIONS FOR FUTURE RESEARCH

Future research in this field should be directed at validating the numerical model results of the present investigation with a laboratory model and with data compiled in the field. Also, further research should be undertaken to develop a technique(s) allowing for an increase in the level of compaction in order to meet design requirements.

REFERENCES

Athanasopoulos, G. A., Pelekis, P. C. and Anagnostopoulos, G. A., 2000, *Effect of Soil Stiffness in the Attenuation of Rayleigh-wave motions from field measurements*, Soil Dynamics and Earthquake Engineering, Vol. 19, pages 277-288.

BNQ (Bureau de normalisation du Québec), 2005. BNQ 2501-255 : Soils - Determination of the Water-Density Relation - Modified Effort Compaction Test (2700 kN.m/m^3), pages 1-13.

Chow, Y. K., Yong, D.M., et al., 1994. *Dynamic Compaction of Loose Granular Soils: Effect of Print Spacing*, Journal of Geotechnical Engineering, Vol. 120, no. 7, pages 1115-1133.

Das, Braja M., 1993, Principles of Soil Dynamics, Southern Illinois University, Carbondale, pages 90-96.

Das, Braja M., 1995, Fundamentals of Geotechnical Engineering, Brooks Cole Thomson Learning, Pacific Grove, California, pages 51-74.

Hanna, A. M., 2003, *Laboratory Compaction of a Subgrade Layer Overlying a Deep Soil Deposit*, Ground Improvement, Vol. 7, no. 7, pages 1-8.

Hanna, A.M., and Saad, N. 2001. Effect of Compaction Duration on the Induced Stress Levels in a Laboratory prepared Sand Bed. ASTM, Geotechnical Engineering Journal, 24 (4).

MTQ (Ministère des Transports Du Québec), 1997. Recueil des méthodes d'essai, *LC 21-040*, Sainte-Foy, Québec, Les Publications du Québec, pages 1-8.

Nashed, R., Thevanayagam, and Martin, G. R., 2006, *Simulation of Dynamic Compaction Processes in Saturated Silty Soils*, ASCE GeoCongress 2006.

Pan, J. L., and Selby, A. R., 2002. *Simulation of dynamic compaction of loose granular soils*, Advances in Engineering Software, Vol. 33, pages 631-640.

"PLAXIS" v 8, 2006. "PLAXIS" Version 8 Reference Manual, Netherlands.

Poran, Chaim J. and Rodriguez, Jorge A., 1992, *Design of Dynamic Compaction*, Canadian Geotechnical Journal, Vol. 29, pages 796-802.

Rollins, Kyle M., Jorgensen, Stan J., and Ross, Todd E., 1998, *Optimum Moisture Content for Dynamic Compaction of Collapsible Soils*, Journal of Geotechnical and Geoenvironmental Engineering, Vol. 124, No. 8, pages 699-708.

Walsh, K.D., Houston, W. N., and Houston, S. L., 1997, *Field Implications of Current Compaction Specification Design Practices*, Journal of Construction Engineering and Management, Vol. 123, no. 4, December 1997, pages 363-370.

Yulek, Mustafa, Dynamic Compaction of a Thin Subgrade Layer Overlying Weak Deposit, Master of Applied Science Thesis, Concordia University, April 2006.

Zerwer, A., Cascante, G. and Hutchinson, J., 2002, *Parameter Estimation in Finite Element Simulations of Rayleigh Waves*, Journal of Geotechnical and Geoenvironmental Engineering, Vol. 128, No. 3, pages 250-261.